Patterns and Instabilities in Colloidal Nanoparticle Assemblies

Emmanuelle Pauliac-Vaujour

Thesis submitted to the University of Nottingham
for the degree of Doctor of Philosophy

May 2008

Abstract

Colloidal nanoparticles exhibit unusual individual and collective behaviour, often associated with interesting electrical, optical or electromagnetic properties. Thiol-passivated colloidal gold nanoparticles possess in addition a self-organising property, which, when the particles are deposited on a substrate, yields a plethora of fascinating patterns. The conditions of formation of these patterns are investigated, in order to understand the principles of - and gain control over - non-equilibrium self-organisation following drop evaporation.

The work presented in this thesis relies mostly on experimental observations, although the results are supported by numerical simulations carried out in the group and based on modified versions of the model developed by Rabani *et al.* in 2003 [1]. A novel deposition method is introduced, which provides controllable conditions for the occurrence of a wide variety of patterns, including close-packed monolayers of nanoparticles. Pattern and surface characterisation is achieved by combined microscopy techniques - atomic force microscopy (AFM) and real-time contrast-enhanced optical microscopy. The influence on pattern formation of the nanoparticle-solvent-substrate interactions is studied by altering the physical properties of all three components (substrate, solvent and nanoparticles).

The experimental set-up allows a meniscus-driven evaporation of the solvent of the nanoparticle solution and enables monitoring of drying front instabilities during the dewetting process. The effects of these instabilities on pattern formation are investigated and highlight a strong contribution of free excess ligands.

We have focused on two specific types of patterns which emerge in these experiments : fingering structures and nanoparticle rings. The former are reminiscent of patterns that form in a number of other systems, a process usually called "viscous fingering". A thorough investigation reveals that the mechanism of formation of such patterns involves the combination of specific experimental conditions and at least two different dewetting processes, with

different time and length scales. A "pseudo-3D" Monte Carlo model recreates such conditions and yields simulated results which are in good qualitative and quantitative agreement with experimental results. On the other hand, nanoparticle rings, although they are a recurrent type of pattern observed in nanoparticle assemblies [2, 3], form according to a mechanism which is not yet fully understood. We show however that wetting properties play a central role in ring formation and growth. As in the case of fingering structures, a narrow range of parameters has been determined, via an exhaustive experimental investigation, which favours the occurrence of nanoparticle rings.

For all the nanoparticle assemblies studied in this thesis (close-packed monolayers, fingering structures and nanoparticle rings), the deduction of pattern formation mechanisms from experimental observation (and simulations) relies on the very high degree of reproducibility that it is possible to attain using the combination of a meniscus-driven evaporation, a very fine tuning of experimental conditions and nanoparticle-solvent-substrate interactions, and a systematic cross-characterisation by complementary imaging techniques.

List of publications

E. Pauliac-Vaujour, A. Stannard, C. P. Martin, M. O. Blunt, I. Notingher, P. J. Moriarty, I. Vancea and U. Thiele, *"Fingering instabilities in dewetting nanofluids"*, *Phys. Rev. Lett.* **100**, 176102 (2008).

A. Stannard, C. P. Martin, E. Pauliac-Vaujour, P. Moriarty, U. Thiele, *"Dual-scale pattern formation in nanoparticle assemblies"*, *submitted to J. Phys. Chem. C* (2008).

E. Pauliac-Vaujour and P. Moriarty, *"Meniscus mediated organisation of colloidal nanoparticles"*, *J. Phys. Chem. C* **111**, *44*, 16255 (2007).

C. P. Martin, M. O. Blunt, E. Pauliac-Vaujour, I. Vancea, U. Thiele and P. Moriarty, *"Organising nanoparticles via directed solvent dewetting"*, *Phys. Rev. Lett.* **99**, 116103 (2007).

J. A. Hayton, E. Pauliac-Vaujour, P. J. Moriarty, *"Anisotropic Assembly of Colloidal Nanoparticles : Exploiting Substrate Crystallinity"*, *NANO* **2**, 361 (2007).

M. O. Blunt, C. P. Martin, M. Ahola-Tuomi, E. Pauliac-Vaujour, P. Sharp, P. Nativo, M. Brust and P. Moriarty, *"Coarced coarsening of nanoparticle assemblies"*, *Nature Nanotech.* **2**, 167-170 (2007).

C. P. Martin, M. O. Blunt, E. Pauliac-Vaujour, A. Fahmi, A. D'Aleo, L. De Cola, F. Vögtle and P. Moriarty, *"Self-organised nanoparticle assemblies : a panoply of patterns"*, in *"Systems self-assembly : Multidisciplinary snapshots"* (Studies in Multidisciplinarity, Volume 5). Editors: N. Krasnogor, S. Gustafson, D. A. Pelta and J. L. Verdegay (Elsevier 2007).

M. O. Blunt, M. Suvakov, F. Pulizzi, C. P. Martin, E. Pauliac-Vaujour, A.

Stannard, A. Rushforth, B. Tadic and P. Moriarty, *"Charge transport in cellular nanoparticle networks : meandering through nanoscale mazes"*, *Nano Lett.* **7**, 855-860 (2007).

Acknowledgements

What makes doing a 3-year PhD course and writing up a thesis enjoyable is not the fact that you are fascinated by the subject, or convinced that your research will change the world. Although these obviously help. But what really makes the most of being a research student is the help and support that you receive from other people, may they care about your research subject, the results of your latest experiment, or simply about you doing the job that you like.

I really enjoyed this experience, and I owe a large part of it going so smoothly to my supervisor, Philip Moriarty. Thank you Phil for having me as a student, for being always so passionate when your students face moments of doubts and frustration, for being so extravagantly clumsy and hard to follow but also being the first to laugh about it, and for helping me to stick so perfectly to my improbable timetable.

I want to address many thanks to the people involved in the PATTERNS network: to Uwe Thiele, for always hunting the most far-fetched errors in the problems that we submitted to him, to Mathias Brust and Paola Nativo, who spent a lot of energy filling the gaps in my basic knowledge of Chemistry, to Dave Corcoran and Harm Rotermund, whose conversations never failed to entertain me during our yearly workshops, and to Ulli Steiner, Bosa Tadic and all the other people - students and permanent staff - of the network.

Among the Nottingham people, I would like to thank James Sharp and Ioan Notingher for their helpful views and comments during the course of my PhD. I also thank Matt Blunt, maestro of the lab, and Chris Martin, for the best laughs at work and in conferences (no contest). Finally, I thank all the present and past members of the nanoscience group, who coped with their "Frenchie" for 3 years, with a special thanks to Ivanka, whose company I missed a lot in my final year. Thanks also to Jason, Elliott and Jau-Yi from B120, and to Dave for the company in the clean room. To you all, "so long, and thanks for all the fish"...

Enfin, merci à ma famille et à mes amis. Si vous ne pouvez comprendre que quelques lignes de cette thèse, autant que ce soient celles-ci. Merci papa et ma-

man pour votre soutien, toujours discret, toujours présent. Merci Julie, Coralie et Romain, les trois autres quarts de mon premier centenaire. Merci mille fois Yoanna, pour les pétages de plombs devant les ravioles de l'Amphitryon. Ce furent les meilleurs moments. Merci Sébastien pour ta patience et pour tout ce que tu sais. Enfin, j'ai une pensée émue pour ma mamie, que j'adore tendrement, et pour mon papy, dont la curiosité et l'inventivité en auraient fait le meilleur chercheur du monde.

C'est à toi, mon Géo Trouvetout de Papy, que je dédie cette thèse.

"Y aller ou pas... La décision d'entrer dans un sujet engage une partie qui n'est jamais gagnée d'avance."

Pierre-Gilles De Gennes.

Contents

Chapter 1

Introduction: What motivated this research ?

"Surely we can, at even a brief glance, tell a crystal from a living creature, an insect from a rock ?"

Philip Ball.

This chapter is intended as a general and illustrated introduction to the "science of pattern formation", from its origins to its implications in today's research. The understanding of this field lies in the ability to connect things and events on a very broad scale and in many different disciplines. From a mere snowflake to the Grand Canyon, from the hide of a giraffe to froth bubbles, scientists of all times have been faced with the fantastic complexity of nature and have worked to unravel the physics associated with this ubiquitous phenomenon, from the macroscopic to the atomic scale.

1.1 The intrigue of pattern formation in Nature

Not everyone may be aware of it, but spontaneous pattern formation takes place all around us, on all scales and at all times. It is present in the tree growing in the park, the cracking earth on a hot summer day, or the water dewetting from our skin when we get out of the bath. The scientific field in which these phenomena are studied is concerned with the emergence of "a natural or chance arrangement of shapes or markings having a decorative or striking effect", according to the definition that the Oxford English Dictionary gives of a *pattern*. And if there is one thing that nature can sometimes be, it is certainly "striking" (see Fig. 1.1).

As Philip Ball observed in his excellent book *The Self-Made Tapestry, Pattern formation in Nature* [6], however, "nature's artistry may be spontaneous, but it is not arbitrary". The ability of nature to purposefully form objects and shapes of such outstanding beauty and complexity with apparent reproducibility, without necessitating external appeal, has captivated scientists, novelists and inventors from the fifteenth century to nowadays. Let us for instance cite Leonardo Da Vinci, renowned for exploiting in his art - and designing most of his inventions according to - the so-called *golden ratio* which is a recurrent, and yet unexplained, aspect ratio observed in nature. Figure 1.2 illustrates some of these famous pieces of his work : the supposedly ideally proportioned Vitruvian man, the so-called "helicopter" wing, and some of his other flying wings, all inspired by his observations of natural phenomena (see also [7] for an exhaustive translation of Da Vinci's notebooks). It is this faculty of obser-

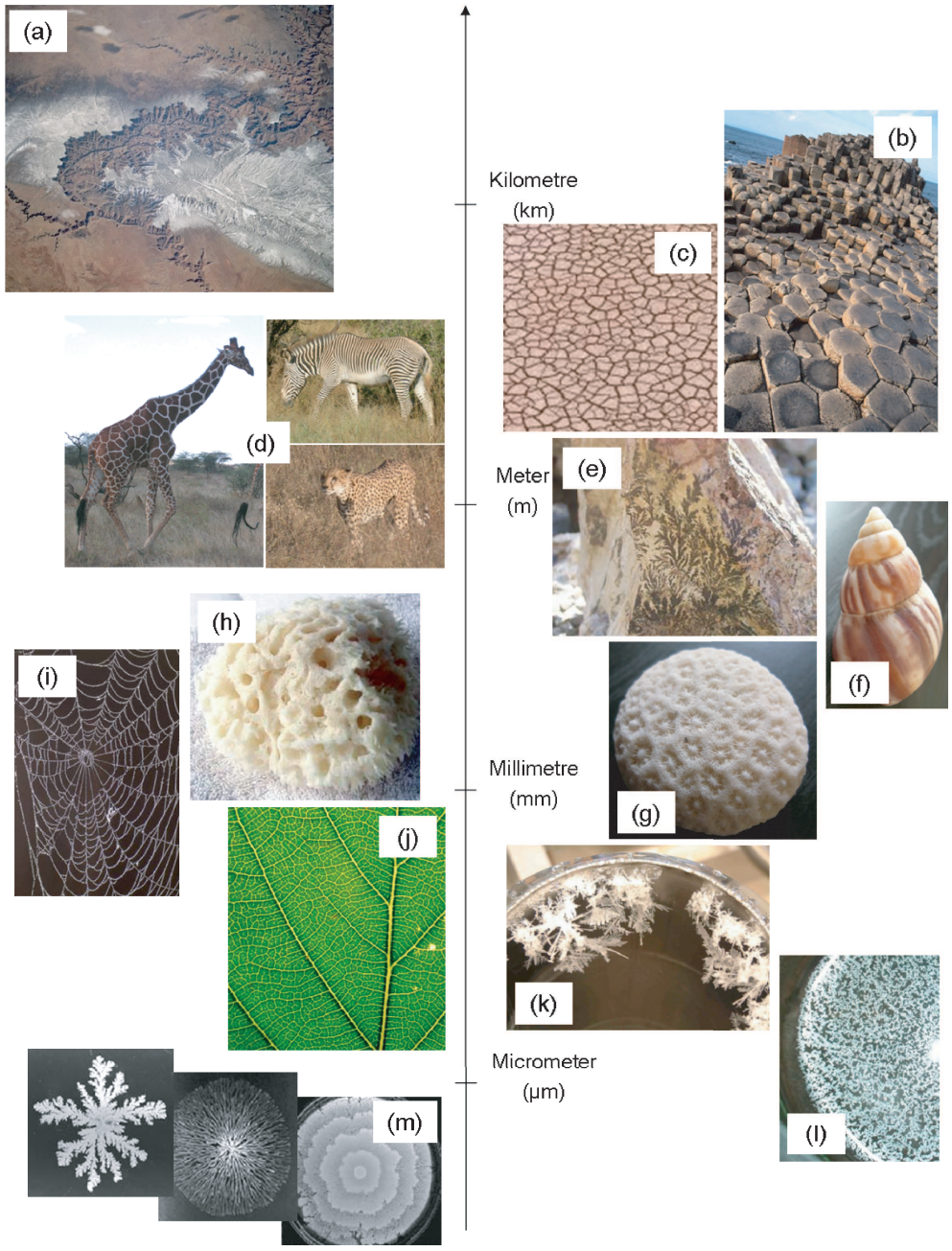

Figure 1.1: *Examples of patterns in nature : (a) the Grand Canyon, Arizona, USA, (b) the Giant's Causeway in Antrim, Northern Ireland, (c) cracked earth, (d) reticulated giraffe, zebra of Grévy and cheetah, Kenya, (e) branched mineral fossils in a rock, (f) shell, Kenya (g) marine fossil, Kenya, (h) natural sponge, (i) spider web, (j) tree leaf, (k) ice crystals, (l) particles of silver ink on the surface of water, (m) bacteria colonies. (a), (b), (e), (h), (i) from [4]; (c), (d), (f), (g), (j), (k), (l) by author and (m) from [5].*

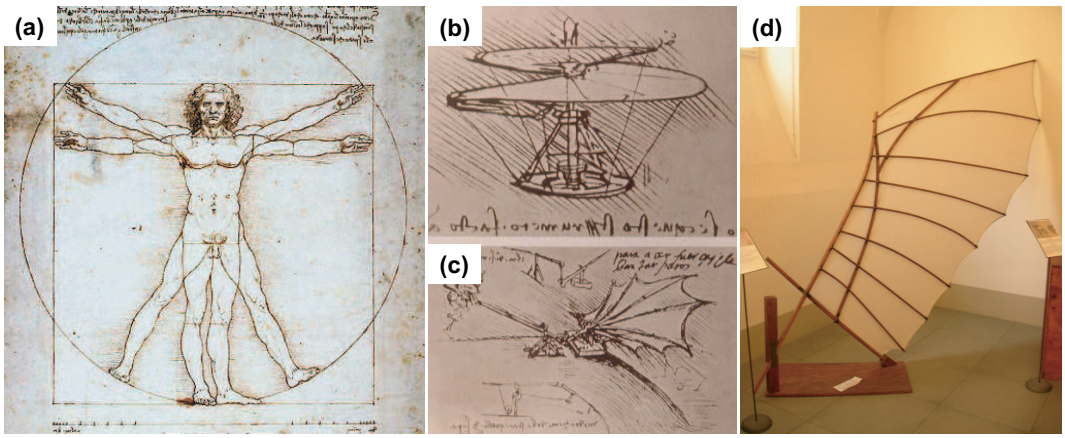

Figure 1.2: *(a) The Vituvian Man, (b) the "helicopter" and (c)-(d) flying wings designed by Leonardo Da Vinci based on his observation of nature. (a-c) from [4], (d) by author.*

vation and interpretation, promoted by many past researchers, that has led to the emergence of the "science of pattern formation", if such a field can be said to exist, and that I would like to introduce as the origin of the work I have been carrying out for three years.

A subject of intense curiosity for scientists

The excitement that has grown around the formation of patterns and the science associated with it can never be as well understood as when it is illustrated by a few everyday examples. As in the case of Leonardo Da Vinci mentioned earlier, the mere observation of nature has led to very many discoveries and inventions, regarded today as the essence of some of the principles of modern science. Some such major contributions are outlined below.

Henri Bénard (1874-1939), France : The cracks in a dry patch of mud, the hide of a giraffe or hot oil in a pan have one thing in common : a cellular structure. Despite their striking similarity, the principles that lead

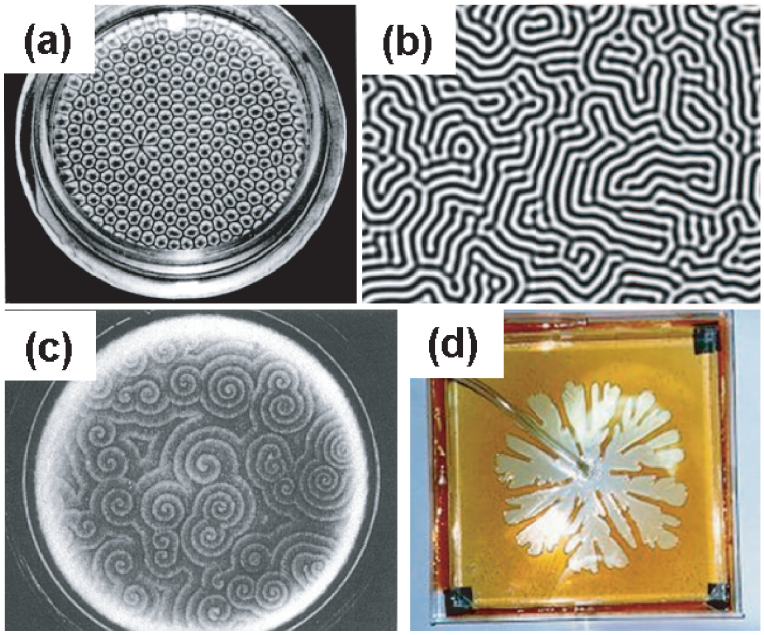

Figure 1.3: *Some famous scientific observations of the twentieth century, from which originate some of the most fundamental principles of the physics of pattern formation today : (a) Bénard's convection cells, (b) an example of Turing patterns, (c) spirals forming during a BZ chemical reaction, (d) formation of viscous fingering in a Hele-Shaw cell.*

to these patterns are very different and well-understood today. For instance, the latter (oil in a pan arranging into regular hexagonal cells) results from a convection movement, which was first observed and identified as such by Henri Bénard in 1900 [8]. He discovered that a liquid trapped between two media of different temperature will, for a critical value of the temperature gradient, adopt a macroscopically ordered configuration, with a characteristic length scale : it forms convection cells, induced by the periodic rotational flow of the fluid within the layer (Fig. 1.3(a)). This observation is fundamental to appreciate and discern the effects of convective movements in liquids, and other important hydrodynamic principles were deduced from it (one of them, the Marangoni effect, is described later in Section 2.2.4).

Alan Turing (1912-1954), England : I evoked the hide of a giraffe earlier but I could as well have cited the regularly spaced stripes on a sea-shell or the colourful and sometimes extravagant patterns on a butterfly's wings. The mechanism that leads to the formation of these patterns is believed to derive (although this remains mostly an open question) from Turing's study on morphogenesis, published in 1952 [9], and his discovery of what is now famously known as "Turing patterns" (Fig. 1.3(b)). He imagined a chemical reaction which would spontaneously promote symmetry breaking of an initially isotropic system, and generate spatially stable patterns (the concept of symmetry breaking is considered as a source of pattern formation and will be discussed again in Section 2.1.1). The very important principle arising from his work is that differences in the diffusion rates of an auto-catalyst and an inhibitor can create areas where either one or the other of the species dominates, causing a spatial segregation of the species. It also prompts the existence of long-range (inhibition) and short-range (activation) interactions, appellations that were subsequently attributed to these phenomena in 1972 by Meinhardt and Geier [6]. Nowadays, many pattern-forming systems have been designated as *activator-inhibitor systems* following Turing's research.

Boris Belousov (1893-1970) and Anatol Zhabotinsky, Russia : At the same time as Turing was discovering activator-inhibitor systems, Belousov and Zhabotinsky were pursuing an experiment from which would originate a long and passionate debate amongst physicists [10–13]. Their steadily oscillating chemical reactions, also called "BZ reactions" (Fig. 1.3(c)), were initially believed to contradict the second law of thermodynamics, for they were regarded as systems that could basically create order from a disordered

(or isotropic) state. In fact, the Belousov-Zhabotinsky experiment represented the dawn of *reaction-diffusion systems*, into which the production of one of the chemical species periodically counteracts the production of the second species, and vice versa, causing the solution to adopt an "indefinitely" oscillating behaviour (note that new reactants need to be provided continuously to keep the reaction going) [10]. Turing pattern forming solutions belong to the category of reaction-diffusion systems, and so do many other systems today.

Henry Selby Hele-Shaw (1854-1941), England : If we are to consider other scientists who provided great insights in science mostly by observation (and there are very many of them), let us cite Henry Hele-Shaw, for example, who was an engineer, passionate about naval mechanics and concerned with the physics of fluids and flows. He invented a device in 1898 [14] that is still now an insightful tool for many researchers in many fields, and which is rightfully called the "Hele-Shaw cell" (Fig. 1.3(d)). It allows the study of fluid flow at the interface between two fluids of different viscosities, a matter of huge interest today in the oil extraction industry, for example. The less viscous fluid tends to spread through the most viscous fluid in the shape of fingers, that grow, develop and sometimes split to form repeated fingering protrusions (see Chapter 5 for a more detailed explanation). The principle that governs the formation of these fingered patterns was explained much later in 1958 by Saffman and Taylor [15] and is thus called the "Saffman-Taylor instability". Needless to say that once again, this instability is a key principle that enables an understanding and explanation of the behaviour of numerous systems involving fluid flows and finger formation.

There are many examples of how the observation of pattern formation has

led to some of the most important conclusions and principles of today's physics, from geological studies in the sixteenth century [16] to the study of bacterial colony growth in the past decade [17]. The objective here is not to write a natural science review but to establish that there exists a clear correlation between spontaneous natural phenomena and well-established physics principles, between the macroscopic and the microscopic scales, and that *critical observation* is a powerful tool to guide us toward possible unifying principles of pattern formation.

Classifying patterns

The first stage in studying pattern formation is observation. The next step consists of classifying the various patterns and establishing degrees of similarity, before ultimately being able to understand and exploit the physical principles that underlie their formation (see also Section 1.2).

Some patterns exhibit a property called "self-similarity", which means that they are similar on all scales (and not necessarily *identical*). These patterns are said to be *fractal* (see Fig. 1.4). Fractals are mathematical objects and the *fractal dimension* is the mathematical measure that was developed in the 1970s to classify those patterns. In his book *The Fractal Geometry of Nature* [18], Mandelbrot explicitly highlights the self-similar character of naturally occurring patterns such as coastlines, trees or rivers. His classification of fractal-like patterns has become a standard tool for describing some of the patterns in nature. However, although of great importance to the field of pattern formation study, this tool remains rather artificial and cannot generally be applied to all patterns in nature. In our case, it will be of interest for the study of one

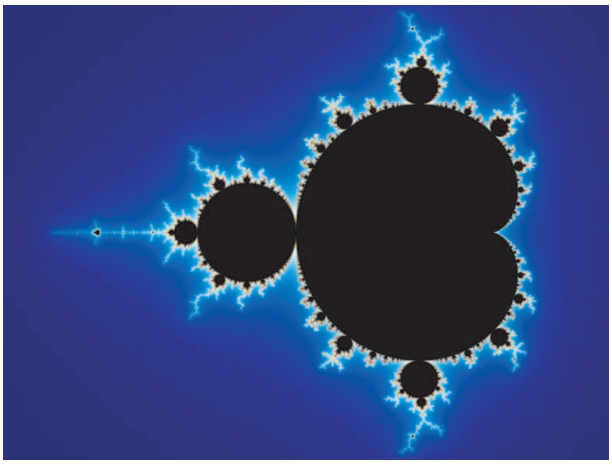

Figure 1.4: *The Mandelbrot set is a fractal discoveved by Benoît Mandelbrot in 1977.*

particular type of pattern (see Chapter 5).

Following the example of the fractal dimension, there exist many different tools to associate a degree of quantification to other patterns, such as, for instance, the Voronoi tessellation for cellular networks [19–21]. However, there also sometimes exists a "natural" classification of patterns, whose significance remains partly mysterious to scientists : the golden ratio that was used by Da Vinci to design his ideal Vitruvian man, is a good example of this natural necessity to classify patterns and quantify their degree of resemblance or dis-resemblance. However, it is also a good illustration that quantifying one's observations does not necessarily address the larger issue of the mechanisms that drive pattern formation. Indeed, why the spiral shape of a shell, or the spacing between its stripes, should depend on the golden ratio still cannot be explained nowadays. It remains a mere observation. The goals of scientists who study pattern formation are thus (i) to fill the gaps left by previous observers and deduce the yet-not-understood mechanisms of pattern formation, and (ii)

to turn towards new fields of interest, new systems and new scales for which the study of pattern formation is mostly at the stage of observation nowadays (thanks to the recent development of new characterisation tools).

Establishing the principles of pattern formation

To summarise and conclude this introductory section on pattern formation in nature, there exist different visions of this phenomenon and different ways of studying it. A natural approach consists of combining an accurate experimental observation with a powerful tool of characterisation and quantification in order to deduce laws, principles and mechanisms at the origin of pattern formation.

The final shape of a pattern can, more often than not, teach us something about the *cause* that created it. *Guiding forces* can be identified - instability, diffusion, activation, inhibition are some concepts, related to this issue, that we have already encountered - that generate patterns of striking resemblance in systems that initially seemed to have nothing in common. The idea that there may exist a few grand unifying principles that govern the formation of patterns on all scales and in all systems is one of the main motivations of this work. Although this assumption can be considered as perhaps premature for the time being, it has served as a guide to many scientists of the past century, and many elementary and today broadly-accepted physics principles have been derived from their work.

In that sense, the study of pattern formation is not generally intended as a predictive science. However, to some extent, it is now possible to predict the formation of given types of pattern in some very well-known systems,

under finely controlled conditions. *Controlling* the formation of patterns seems the natural next stage in this domain of research. This aspect of pattern formation is the second main motivation of this work, since it opens the way to a multitude of applications, particularly at very small scales, which are the centre of interest of numerous researchers and industries today.

1.2 Patterns and Nanoscience

The subject of this thesis fits into the broader scheme of 'the study of materials and their properties at the nanometer-scale', also called "nanoscience". We are particularly interested in the ability of these nano-materials to create specific patterns. Now, some questions that we might ask ourselves are : despite the understandable - and noble - motivation of explaining the formation of all patterns on all scales and in all systems (an ambitious agenda, to say the least), how can we relate the principles deduced a century ago to today's research at the molecular level ? And what prospect is this work going to give us in terms of applications with regard to so called "nanotechnology" (i.e. the applications of nanoscience research) ?

What is at stake

Nanoscience has become, in the past few decades, one of the most fashionable areas of scientific research. Immense interest (and investment) is brought into nanotechnology ; groups of scientists worldwide, and in all disciplines, have started to investigate the fascinating properties of nanometre-sized objects and phenomena. However, if one asks for a definition of nanotechnology,

then there are probably as many answers as there are people involved in the field ! Nanotechnology is concerned with objects at the nanoscale, where their properties become radically different from those of the macroscopic form of the same objects. Even further along these lines, the individual and collective properties of nano-objects, as they are called, differ, and nanotechnology aims at exploiting these various properties. Gaining control over these new nanoscale effects implies the development of a bewildering number of new applications, be they, for example, in biology, chemistry or surface science. In the case of materials science, the early stage of research into the nanotechnology area is of major importance, since it is from this field essentially that are supposedly expected to emerge so-called *designer materials* or *intelligent materials*, especially designed at the nanometre scale to achieve specific tasks. In reality, although nanotechnologies are now slowly and gradually spreading out of fundamental research laboratories to reach the world of industrial mass production, most of the concepts and principles underlying the physical properties of objects at the nanometer scale are still to be understood, let alone controlled.

The systems that we will study here exhibit very interesting individual and collective properties, one of the most poorly-understood of all - though promising for applications - being their ability to create long-range ordered, i.e. non-random, arrangements : this is called self-assembly or self-organisation (the difference between these terms will be discussed below). In a similar way as Hele-Shaw or Belousov and Zhabotinsky, we are now faced with a system which shows a remarkable behaviour and two issues are to be considered : (i) deducing pertinent principles that will enable us to understand the physics

associated with this phenomenon, while (ii) keeping in mind the possible larger scale applications of these systems. To highlight the necessity of carrying out such extensive research, let us consider a few examples of recent successful nanotechnological developments which combine these two requirements and give a better understanding of the challenges of nanoscience and the study of pattern formation.

Getting control

In 1986, Gerd Binnig and Heinrich Rohrer received the Nobel Prize for their invention of the scanning tunnelling microscope (STM), only four years after they first presented their work to the international scientific community [22, 23]. This incredibly fast appreciation and reward of their work shows the impact of nanotechnology-related discoveries. By offering a brand new tool for investigating the nanoscale (Fig. 1.5(a)), Binnig and Rohrer opened the doors to innumerable new paths of research. Indeed, not only was it now possible to *see* the "nanoworld" (including the formation of patterns at this scale, which is the object of my own research), but people also saw the STM as a tool to interfere with the natural organisation of things at the nanoscale and gain a little bit more control over the behaviour of atoms and molecules. The first and best illustration of this is the manipulation of atoms on a surface as achieved only a few years later by Eigler and Schweizer, in 1990 [24] (see Fig. 1.5(b)). They demonstrated the manipulation of individual xenon atoms with an STM tip with a degree of control never achieved before, and although spelling the logo "IBM" on a surface may not find a direct industrial application, it marked the beginning of the new era of nanotechnology and control over nanoscale

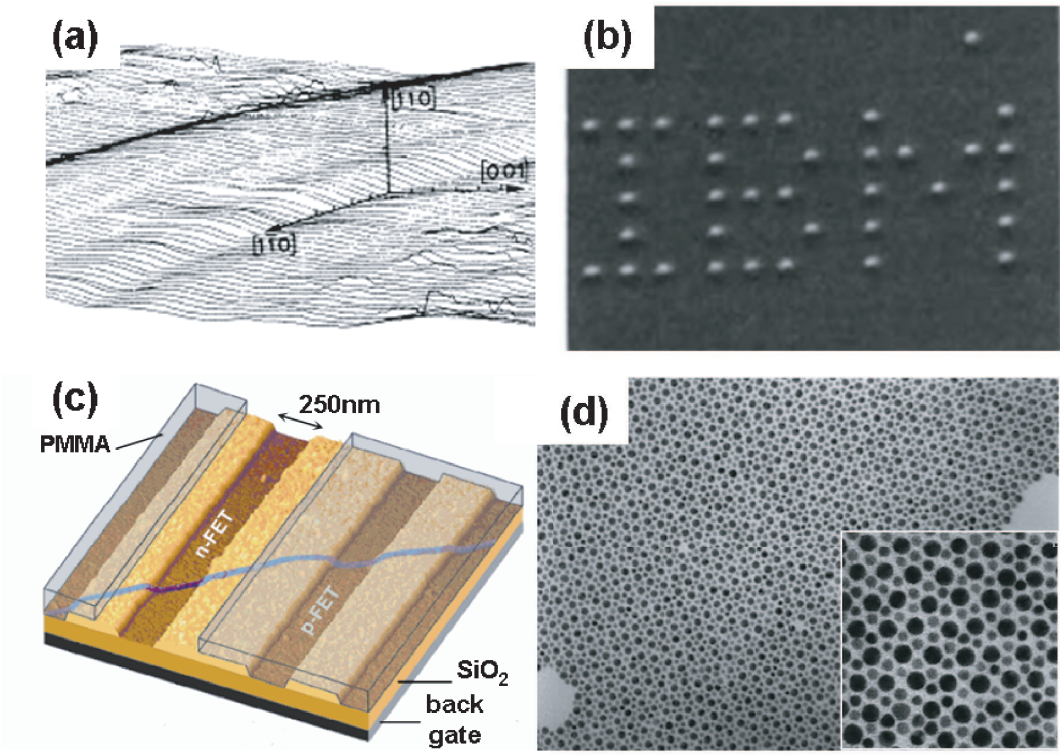

Figure 1.5: *(a) Scanning tunnelling micrograph of an Au(110) surface, Binnig and co-workers [23]; (b) IBM logo formed by xenon atoms on a nickel (110) surface using STM, Eigler and Schweizer [24]; (c) AFM image of two carbon nanotube field-effect transistor (CNTFET) in series, Derycke* et al. *[25]; (d) transmission electron micrographs of a bimodal array of Au nanoparticles of two different sizes (size ratio 0.58, the insert in a close-up view), Kiely* et al. *[26].*

objects.

Nanostructured objects have ever since become the fashion in many domains of science, ranging from physics to biomedical science, accompanied by the emergence of the concept of "grey-goo", featuring futuristic nano-robots injected into the human body and, in a Hollywood-style scenario, slipping dramatically out of control (!), or the *nano-factory*, an independent unit able to produce nano-objects at the industrial scale. Without going this far into the world of fantasy, let us say that the biggest achievement in fabricating nano-

objects that actually have a dedicated task goes about as far as producing a single molecule transistor, which is in itself a revolutionary achievement, although this concept might not sell so many science-fiction novels. The fabrication of nano-devices found its first real applications in 2001, when several groups reported almost simultaneously that they had successfully interconnected several of these elementary objects to form functional networks. The eagerness was such that wiring up molecular devices was voted the "breakthrough of the year" by *Science* magazine [27]. Thanks to the intensive work of a few groups (Lieber's in Harvard, Heath's in Los Angeles, Dekker's in the Netherlands and, needless to say, some IBM labs), nanowires and nanotube-based junctions and transistors (see Fig. 1.5(c)), first reported in 1999 by Dekker [28], could now be assembled into intermolecularly connected logic circuits. *Science* published no less than 6 reports on the subject in 2001 alone [29–34] . Soon after followed single-molecule tunnel junctions [35] and transistors [36, 37]. In 2002, polymer nanocrystal LEDs made their appearance [38] and in 2003, wiring up single-molecule devices attained yet another degree of complexity with the use of self-assembled templates [39]. These achievements are of major importance for the miniaturisation of integrated circuits and the imminent short-coming of Moore's law concerning the progress of the capacity of integration [27] (we will come back to this later).

Review articles such as Moriarty's on the state of research on nanostructured materials, dated from 2001 [40], and Weiss and co-workers', dated 2004, on patterning materials at the nanoscale [41] give a good appreciation of the investment (both financial and human) that was brought into the field of nanotechnology since the 1990s. Within less than 20 years (a strikingly in-

significant amount of time compared to the several centuries of Section 1.1), nanoscience has invaded the domains of materials science, electronics, optics, electro-magnetism, biomedical science, etc. The field that we are concerned with here is the study of nanometre-sized chunks of material (a few nm in size), in the shape of colloidal nanoparticles, and both their individual and collective properties. This is also a subject that has been the centre of much attention over the past decade or so (see Section 2.3) and has seen several major turning points within the past 10 years. In 1996, Andres *et al.* first exploited the self-organising behaviour of colloidal nanoparticles to form long-range ordered arrays of metallic nanoclusters separated by an insulating polymeric barrier [42], which had some time before been described as an ideal theoretical system for the study of Coulomb blockade and single electron conduction [43] (see section 2.3). Many experimental studies were derived from this initial work to exploit the unusual collective conduction properties of arrays of metallic nanoparticles [44–48]. Control over this self-organising behaviour attained yet another turning point only two years later, in 1998, when Kiely *et al.* first reported the self-assembly of a bimodal array of nanoparticles [26], i.e. an array where particles of two different natures or sizes self-organised to form a long-range ordered matrix (see Fig. 1.5(d)).

These few examples give a better idea of the influence that nanoscience has had over the past few decades in scientific research, even more so when combined to a field as interdisciplinary and incompletely understood as pattern formation. While keeping this in mind, I shall now proceed to a more direct description of my work, starting with a few definitions.

The definition of terms

The terminology associated with pattern formation at the nanometre scale can be confusing, for many terms tend to be used interchangeably. Before moving on to describing the work that I carried out, it seems essential to define as clearly as possible what the terms of predilection will be here.

Nanoparticles : Nanoparticles are small (<100nm typically) clusters of matter containing a few to a few thousand atoms. For this reason, they are sometimes called "nanoclusters" or "nanocrystals". They exhibit unique properties due to their nanometer size and their very high surface-to-volume ratio, which confers to them a very high reactivity, as opposed to the bulk configuration of the same material. Nanoparticles are known as "quantum dots" when they are grown on a surface under very well-controlled conditions. Quantum dots offer promising opportunities for use as electronic or optical devices, for instance. Nanoparticles can also be suspended in solution, in which case they are called "colloidal nanoparticles". Colloidal nanoparticles of many materials are commonly synthesized which exhibit intriguing electronic, optical and/or magnetic properties. Gold nanoparticles, in particular, are the object of my study and have a vast field of applications (see Daniel and Astruc for a comprehensive review of gold nanoparticles [49]). Colloidal gold nanoparticles (now broadly referred to as "nanofluids") are stabilised in solution either by charge or by a passivation process, which involves attaching ligands to the cluster that will prevent it from aggregating with neighbouring particles in solution. A detail of synthesis processes involving both techniques will be given at the beginning of Chapter 3. Passivated gold nanoparticles are a particularly interesting systems because they are metallic, hence conductive,

whereas the ligands that are used for passivation form an insulating layer around the clusters. Putting several of these clusters close together allows the creation of a nanometre-scale system of capacitively-coupled metallic dots, which is expected to exhibit a specific single-electron conduction behaviour [43–48].

"Top-down" and "bottom-up" : Ideally, atoms, molecules and nanoparticles can be considered as building blocks for larger-scale, tailor-made, devices with novel physical properties. This approach to microfabrication is called "bottom-up" and contrasts with the usual "top down" fabrication that presently governs industrial microfabrication. The "top down" approach consists of reducing the scale of existing components in order to increase the overall capacity of integration. According to the famous Moore's law, this capacity should double every other year. However, top-down fabrication is now reaching its limits, with transistor gates down to 10nm in size, which start to exhibit poorly-known and badly-controlled quantum effects due to an increasing confinement. In this sense, bottom-up fabrication could be the answer to the restrictions imposed by these dimensions, because it aims at controlling these effects, and at the same time solves the issue associated with Moore's law exponential growth.

Self-organisation and self-assembly : Last, but not least, the specific property of colloidal nanoparticles that will be of interest here is their ability to create ordered arrangements once out of solution (e.g. deposited on a surface and dried). This behaviour is called *self-organisation*, because it requires an external source of energy for the phenomenon to occur (e.g. here the evaporation of the solvent); hence it takes place *out of thermodynamic equilibrium.*

An illustration of this process was the convection cells from Fig. 1.3(a), which form as a result of the temperature gradient through the liquid film.

Self-assembly, on the other hand, is a property of systems that can assemble into a non-random configuration *while at equilibrium* (or in a metastable state). Examples of self-assembly are numerous, with one commonly cited, the DNA molecule : the bases on each strand of the DNA molecule have the ability to recognize the bases on another strand. Merely by the effect of Brownian motion, bases on complementary stand-alone DNA strands can self-assemble to form the double helix DNA molecule. The configuration that emerges from this process is the energetically most favourable one. This self-assembly takes place at equilibrium and does not require any external impulse apart from the natural motion of its constituents. The information required to create a self-assembled pattern is said to lie within its individual constituents.

In this report, colloidal gold nanoparticles deposited from solution will be said to self-organise, rather than self-assemble. However, in some of the references cited along this thesis, depending on context, self-organisation and self-assembly are sometimes used interchangeably, adding to the confusion. We will maintain the self-assembly / self-organisation nomenclature whenever the distinction can be clearly made between an out-of-equilibrium pattern formation process (self-organisation) and an assembly occurring at equilibrium (self-assembly).

1.3 Thesis outline

This thesis is intended as a contribution to the study and understanding of the pattern formation process (by self-organisation) in systems of colloidal gold nanoparticles. It is concerned with (i) the nature of the patterns themselves, (ii) gaining control over the experimental conditions that lead to their occurrence, and (iii) the larger scale implications of the physical principles that can be deduced from these observations. The current chapter presents the motivations and starting point of this study and its place in the course of nanoscience. Later chapters will give further details of the context in which this research is based, including a background presentation of colloidal nanoparticle science and the description of experimental techniques involved in this work. For the purpose of this thesis, I focused on the deposition aspects, on wetting and dewetting issues, and on pattern formation itself. Possible applications of nanoparticle manipulation are not explicitly described here but have been exploited in previous studies by our group [47, 50] ; these applications were constantly used as a guide to my work and remain the - more or less - long term objective of this research.

Chapter Two : A background description of the main physical principles involved in pattern formation both at the macroscopic and microscopic levels is given. Growth mechanisms and molecular interactions are discussed, as well as the phenomenon called "dewetting" that is a cause of pattern formation in thin liquid films. A summary of previous studies on the subject of colloidal nanoparticle self-organisation is also presented.

Chapter Three : My research was mostly based on experimental observa-

tion and this chapter depicts the various techniques that could be exploited to analyse the effects of tunable experimental parameters on pattern formation.

Chapter Four : A new deposition technique, adapted from previous work on polystyrene spheres [51], was developed very early into this project and offered a new tool to study the effects of slow evaporation on pattern formation and selection, as opposed to most of the previous work that was carried out for very fast evaporations (see background Section 2.3.2). This technique also reveals some fascinating phenomena such as the correlation between drying front instabilities and pattern formation.

Chapter Five : Tuning experimental parameters within a very narrow range of values can produce striking variations in nanoparticle arrangements. The main part of my research was carried out on self-organised patterns exhibiting a branching behaviour, which is reminiscent of many systems in nature (Section 1.1). Simulations, theories and experimental results are presented (not necessarily in this order) and discussed, that lead to a better understanding of the principles involved in the formation of such patterns. The question of the assembly process during dewetting and evaporation is also addressed, illustrated by the first real-time observation of nanoparticle deposition and self-organisation on a surface.

Chapter Six : Varying one element of the nanoparticle-solvent-substrate system can have a dramatic effect on pattern formation and can help to identify the various interactions at play in this poorly-understood process. This chapter aims at investigating the correlation between nanoparticle-solvent-substrate mutual interactions and pattern formation.

The final chapter summarises the conclusions that were drawn from the

analysis of the experimental results presented, and highlights the contribution of this work in the scheme of colloidal nanoparticle science and pattern formation study, while suggesting possible orientations for future work.

Chapter 2

Pattern Formation: Principles and Driving Forces

"I shouldn't be surprised if some of you prefer the 'just so' explanation, which at least has something to say about how the stripes and spots got there."

Philip Ball.

The work presented in this thesis focuses on the self-organisation of colloidal gold nanoparticles when deposited on a solid substrate. This apparently simple system gives rise to a remarkable variety of complex patterns. The previous chapter described some of the striking similarities that exist among naturally occurring patterns on all scales. This chapter reviews some of the elementary physics associated with pattern-forming systems, and considers the forces, both at the macroscopic and microscopic levels, at play in the *selection* of specific types of patterns. The role of dewetting as a rich source of pattern formation in thin liquid films is highlighted. Finally, a comprehensive background review for our specific research is presented.

2.1 Pattern selection and intermolecular forces

As discussed in Chapter 1, although pattern formation is ubiquitous in nature, so far there does not exist an associated "universal theory". Anyone hoping to understand the complexity of pattern formation will have to content themselves with a set of general principles, through which some experimentally observed complex structures can be explained. In order to look at the "big picture", one has to concentrate on finding one's way towards unifying the principles of non-equilibrium pattern formation. This section is provided as a basis for future reflection upon mechanisms involved in these processes, and describes a number of elementary forces and interactions contributing to the formation of patterns in general.

2.1.1 Competing forces and emergence of a preferred growth mode

Spontaneous pattern formation is generally the result of a competition between two or more driving forces. The more balanced the competition is, the more complex and visually stunning the pattern will be. At least four general "families" of competing forces can be identified. First, we have seen that Turing patterns and oscillatory BZ chemical solutions were classified as reaction-diffusion systems (section 1.1 and Fig. 2.1(a)), which behave according to the subtle balance between short-range activation and long-range inhibition. Second, the Saffman-Taylor instability mentioned earlier results from a competition between branch growth and surface tension, which leads to the formation of a variety of branching patterns (so called "viscous fingering", Fig. 2.1(b)). A

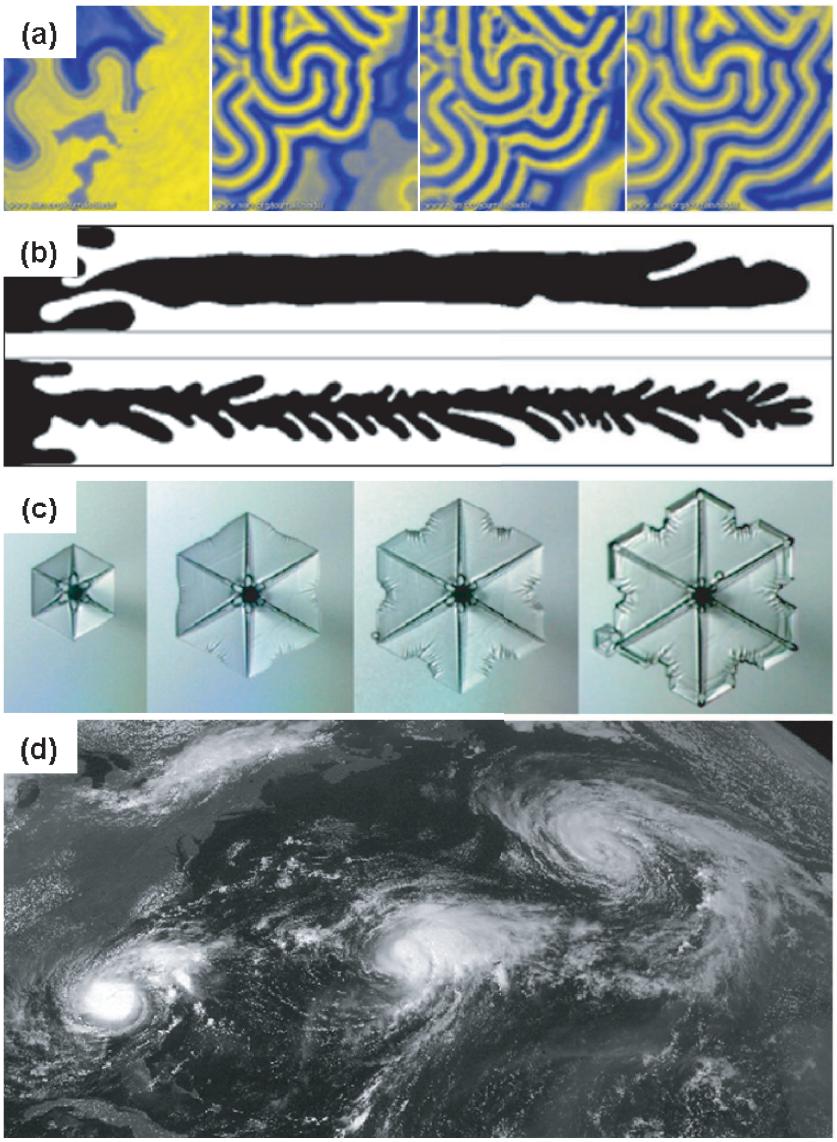

Figure 2.1: *Patterns forming under the influence of competing forces, (a) oscillations and labyrinthine pattern formation in a chemical BZ reaction, from [52], (b) viscous fingers growing in two different preferred growth modes (with different characteristic length scales), from [53], (c) growth of a dendritic snow crystal from a facetted state, from [54] (d) illustration of vortexes : hurricanes Ophelia, Nate and Maria forming above the Atlantic Ocean and approaching the Gulf of Mexico in 2005 (from [55]).*

related - yet not due to the same growth mechanism - type of structure is the dendrite, which is for example the shape adopted by the branches of a snow flake or more generally arising from the solidification of a material from a melt (Fig. 2.1(c)). Dendrites are the consequence of an anisotropic growth. Their resulting morphology will be a compromise between the usually predominant anisotropic event that created them and the presence of noise, which can become overwhelming and lead to extremely complex dendritic structures. Finally, vortex-like disturbances are created due to the competition between a wavy instability and the viscosity of the system (Fig. 2.1(d)).

It was also briefly mentioned that one aspect of pattern formation was the breaking of symmetry. This concept is not trivial and may be explained as follows. When a pattern-forming system (initially random and isotropic) is driven away from its equilibrium state, it tends to do so by breaking as little symmetry as possible at a time. This explains why lines (e.g. wrinkling in polymer films, symmetry broken along one direction) and hexagons (e.g. honeycomb-like convection cells, symmetry broken along two directions) are very commonly observed patterns. As a result, a close-to-equilibrium system will often appear highly symmetrical, which incidentally also makes it rather striking to the eye, whereas a far-from-equilibrium system may present little or no symmetry.

There exists a difference between the order that characterizes an equilibrium system, like a crystal for example, and the ordered non-equilibrium states arising from spontaneous pattern formation. In the former systems, the periodicity of the system is determined by the dimension and geometry of its elementary components (that is to say, for a crystal, the atoms that form it).

The latter systems, on the other hand, are maintained out of equilibrium by a continuous flow of energy. Patterns formed under these conditions are called "dissipative structures". As opposed to the previously described equilibrium systems, they exhibit a spatial scale which is not related to the size of their constituents, but really is the result of intrinsic interactions within the system (and therefore is steady in the face of perturbations). This will play an important role in *pattern selection*.

Pattern formation usually occurs once a critical point in the system has been reached. The pattern then develops with one preferred wave vector, meaning it exhibits one specific spatial length scale (we will come back to this in Section 2.2). The important - and still mostly unsolved - question that remains relates to how to predict the shape of the pattern that emerges. A large number of perturbations with various wavelengths are able to grow and develop within each system, but can we tell which particular wavelength will be selected ?

Indeed, in the case of complex patterns forming at equilibrium, one can easily predict the most favourable configuration of the system (that of lowest free energy), as long as one knows the contributing factors to the free energy. However, for complex patterns forming away from equilibrium, free energy is not the determining criterion, nor is it the minimum entropy production, as initially believed by Prigogine in the 1950s, then ruled out by Landauer in 1975. It is the latter who first implied that these systems were "multistable" in essence, and that to identify the most favourable state, one had to take into account not only the locally stable states of the system, but also its particular environment and *history*.

Although this then makes any generalization of pattern formation principles a problematic issue, one can all the same rely on some general observations in order to, if not predict pattern selection, at least understand it. The principal considerations are as follows : (i) pattern formation occurs by breaking as little symmetry as possible (as was explained earlier), and (ii) the pattern is associated with a characteristic wavelength, which can provide us with information about the history of the system and some of its intrinsic specificities.

Finally, *growing* patterns will be of particular interest in this study. In this case, pattern selection arises not only from the principles outlined above, but is bound to involve also dynamic considerations. This is for example the case in branching patterns, for which there is a subtle balance between the growth speed and the tendency of the tip to split. Two schools of thought exist in this domain, one proposing that the pattern selected is simply the one that grows fastest and outruns the others, the other opting for the mode that maximizes

Figure 2.2: *The diffusion-limited aggregation model [56].*

the generation of entropy. The study of such growth mechanism will be dealt with in Chapter 5. In addition, one should pay particular attention to noise as a pattern-selecting influence. Indeed, it is noise that, for example, will make a difference between a Hele-Shaw like pattern (see Chapter 5) with "fat" branches, and a diffusion-limited aggregation (DLA) pattern [56, 57] with a much more skeletal aspect (Fig. 2.2).

2.1.2 Van der Waals forces, interaction potential and Hamaker constant

Let us now consider pattern formation at the scale of atoms and molecules. We will see how the global behaviour of a pattern-forming system is actually dictated by the combination of interactions present at the microscopic level. Intermolecular interactions are often split into many categories, such as ionic bonds, van der Waals forces or hydrogen bonding to name a few, themselves splitting into subcategories of weak, strong, long-distance or short-distance interactions. To clarify at once the problem of the classification of forces, in the field of colloid physics which we are dealing with here, one will mainly refer to long-ranged intermolecular forces by using the denomination "van der Waals forces" and will occasionally refer to short-range interactions, such as molecular packing or orbital overlap, for example.

Van der Waals forces

Three types of forces contribute to the global van der Waals interaction : the induction force, the orientation force, and the dispersion force. The first two

occur only in the presence of permanent dipoles. Since we are here studying the case of particles without a static dipole moment, these interactions are not of particular relevance to our system and I shall not discuss them any further for now. However, the third type of force is always present and as a result will often represent the predominant contribution to the van der Waals interaction for our system. Dispersion forces are long-range forces (effective from a fraction of a nm up to 10nm of more), that can be either attractive or repulsive. The dispersion forces can be understood as follows : at any moment, the instantaneous positions of all the electrons around the atom create an instantaneous dipole moment. This dipole will induce polarization of nearby bodies and the resulting interaction is an instantaneous attractive force between pairs of bodies. It is interesting to note that, in the absence of dominating intermolecular interactions (e.g. Coulombic or H-bonding forces), there is always an effective attraction between molecules or particles that are alike (because the energy of the associated state is lower than the one of the dispersed state), whereas unlike molecules can either attract or repel each other depending on the relative properties of the species involved. This constitutes the basis of the physics of wetting and dewetting and liquid-liquid demixing, for example.

London forces, Lennard-Jones potential and Hamaker constant

Van der Waals forces comprise three components, namely the Keesom forces or orientation effect between polar bodies, the Debye forces or induction effect between a polar body and an induced dipole, and the London forces or dispersion effect between instantaneous dipoles [58, 59]. All these contributions have an R^{-6} dependence on the separation R between the bodies, meaning

the potential associated with attractive van der Waals forces can generally be written :

$$W(R)_{vdw} = -\frac{1}{R^6}\left[C_{ind} + C_{orient} + C_{disp}\right] = -\frac{C}{R^6} \tag{2.1}$$

where C_{ind}, C_{orient} and C_{disp} are constant terms associated with the induction, orientation and dispersion effects respectively. For coherence with what was said in previous paragraphs, in what follows van der Waals forces will be considered solely in terms of the dispersion component.

Various potentials have been put forward to model the interaction of atoms and molecules, the most famous of which is probably the Lennard-Jones potential :

$$W(R)_{LJ} = 4\varepsilon\left[\left(\frac{\sigma}{R}\right)^{12} - \left(\frac{\sigma}{R}\right)^{6}\right] \tag{2.2}$$

where the R^{-6} term represents the attractive dispersion forces as explained above, and the R^{-12} term describes the repulsive short range interactions. ε is the depth of interaction and σ the hard sphere diameter of the interacting bodies. The shape of this potential is given in Fig. 2.3.

A significant contribution to the understanding of the forces acting between macroscopic bodies in terms of van der Waals interactions was that of Hamaker [60]. His early work relied upon the assumption of an *additive* atomic van der Waals interaction, that is to say that for a potential of the form $W(R) = -C/R^6$, the global interaction between two bodies is given by the sum of the contributions of each body. Hamaker proposed to calculate interactions between macroscopic objects by mere integration over their geometric shape

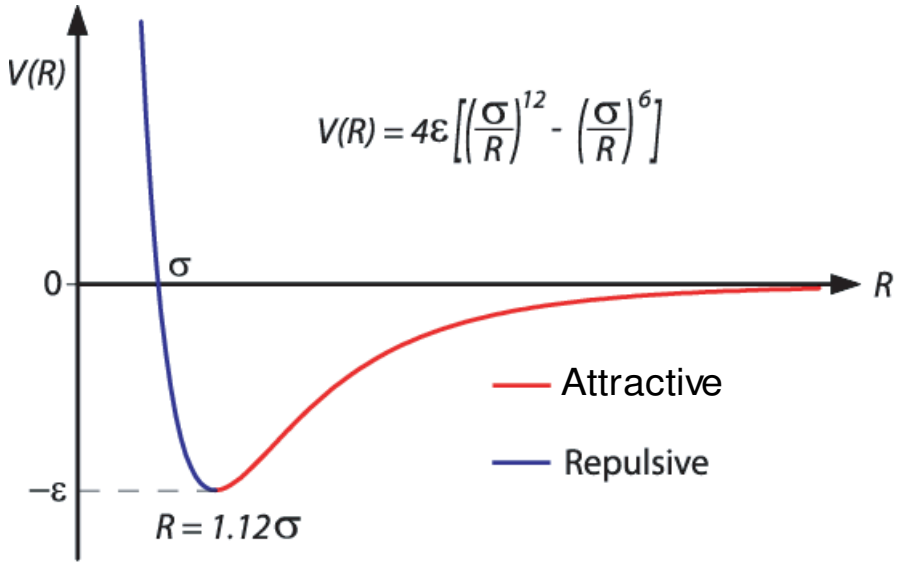

Figure 2.3: *The Lennard-Jones potential. From [47].*

(see, for example, Chapter 11 of reference [61] for a list of expressions of van der Waals interaction free energies between bodies of various geometries). Each interaction law hereby calculated depends on a constant A, called the Hamaker constant, and defined by :

$$A = \Pi C \rho_1 \rho_2 \tag{2.3}$$

where Π is a factor that depends on the geometry of the object, ρ_1 and ρ_2 are the atomic densities in the two bodies and C arises from the van der Waals potential given above and represents the "polarisability" of the interacting media. Following Hamaker's pioneering work, Lifshitz then developed a theory which considered the bodies as continuous media and derived the interaction from their bulk properties rather than their atomic structures. We shall not go through the complex theory developed by Lifshitz [62]. In short, the main difference with Hamaker's calculations of interaction energies for given geome-

tries lies in the way the Hamaker constant is calculated. For an interaction between two media 1 and 2 across a third medium 3, the Hamaker constant can this time be calculated using the equation :

$$A_{123} = \frac{3}{4}k_B T \left(\frac{\varepsilon_1 - \varepsilon_2}{\varepsilon_1 + \varepsilon_2}\right) + \frac{3h}{4\pi}\int \left(\frac{\varepsilon_1(i\nu) - \varepsilon_3(i\nu)}{\varepsilon_1(i\nu) + \varepsilon_3(i\nu)}\right)\left(\frac{\varepsilon_2(i\nu) - \varepsilon_3(i\nu)}{\varepsilon_2(i\nu) + \varepsilon_3(i\nu)}\right) d\nu \tag{2.4}$$

where ε_1, ε_2 and ε_3 are the static dielectric constants (above named "bulk properties") for the three media, and $\varepsilon(i\nu)$ are the imaginary parts of the dielectric constants.

Measuring intermolecular forces

Interactions at the molecular level can be interpreted from a range of experimental measurements and data. For example, thermodynamic data on gases, liquids or solids give access to information on the short-range attractive potentials between molecules. An application of this is the use of adsorption isotherms to monitor the interaction of molecules with surfaces (used in some deposition techniques). For mixtures of liquids, one can also gain information on solute-solvent interactions (which are of particular interest here). Physical data on liquids and solids give an insight into the size and shape of molecules and their repercussions in the overall structure of condensed phases.

In addition to this rather common but incomplete description of intermolecular interactions through basic experimental data, some dedicated experiments allow direct access to the nature and range of the force laws and potential functions, which the previous data do not provide. Among those,

particle detachment and peeling experiments (to measure an adhesion force) are broadly well-known, as are contact angle measurements (adhesion energies related to liquids on liquids or liquids on solids, also called surface tension) and scattering experiments (dynamic data, interparticle separations or motions in liquids) to name a few.

Finally, one can gain access to a direct measurement of these forces, and I shall illustrate this by referring to the technique which has been central to this study of nanoparticles adsorbed on surfaces, that is to say atomic force microscopy (AFM). This technique will be discussed at lengths in the following chapter and all along this report. The forces measured using AFM are in the 10^{-9}-10^{-12}N range, necessitating the use of a whole new highly sensitive technology to be able to detect such small force variations and allow displacements of the order of a fraction of nm. Thus, it becomes possible to gain direct observation of the long-range forces between an atomically-sized tip and a surface and the short-range forces between the species on the surface (see Section 3.3).

2.2 Dewetting of thin films

This section aims to describe some of the dynamics that govern the *drying* of liquids and mixtures of liquids. Pattern formation can originate from the *dewetting* of thin films - a comprehensive review on wetting/dewetting, fluid interfaces and capillary forces can be found in [63]. The driving force that leads to the rupture of the film is the free energy at the surface. Depending on the balance of surface and interface energies, thin films on solid substrates can

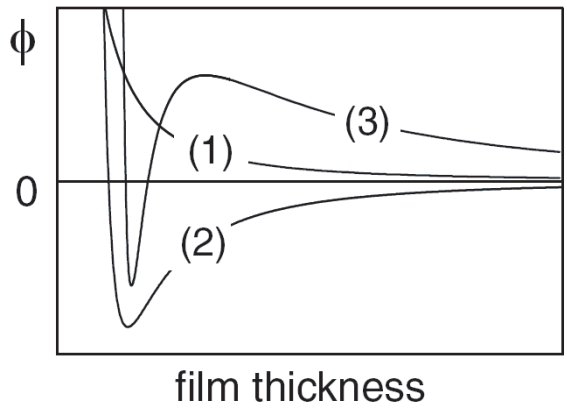

Figure 2.4: *Shape of the interface potential $\phi(h)$ as a function of film thickness for (1) stable, (2) unstable and (3) metastable films. From [64].*

be unstable and dewetting is the process that will bring them towards their equilibrium state, that is to say, a set of droplets. In the following, I outline the key processes associated with dewetting thin films.

The interface potential $\phi(h)$ is the free energy per unit area of two surfaces separated by a distance h. In the case of a thin film on a solid substrate, the surfaces are respectively the solid-liquid and the liquid-air interfaces. h is the thickness of the film. The stability of the film is determined by the shape of its interface potential, as shown in Fig. 2.4. The film can either be in a stable, unstable or metastable state.

In curve *(1)* of Fig. 2.4, the variation of the interface potential with the film thickness is monotonic, i.e. does not show a local minimum. In this case, the thinning of the film has an energetic cost, which means that dewetting is not energetically favourable. The film is *stable*.

Curves *(2)* and *(3)*, on the other hand, exhibit a local minimum for a finite value of h. They represent respectively the cases of an *unstable* and a *metastable* film. The unstable film - curve *(2)* - seeks to reduce its energy by

reducing its thickness, leading to spontaneous dewetting. Such a film is very unstable in face of small fluctuations of its thickness. A metastable film - curve *(3)* - behaves like an unstable film for small values of h, but becomes stable above a critical thickness, corresponding to the local maximum of curve *(3)*. This maximum represents an energy barrier that the system needs to overcome in order to become unstable.

As a result, Fig. 2.4 suggests that dewetting occurs according to two different mechanisms, one of them involving an energy barrier ("nucleation"), not the other ("spinodal"). For metastable films, the thickness needs to be sufficiently reduced for the film to become unstable : this barrier is overcome when a large enough perturbation occurs, e.g. the nucleation of a hole in the layer of liquid. Both spinodal and nucleation-induced dewetting processes are described in some detail below. Note that several dewetting processes can coexist in a single system.

2.2.1 Heterogeneous nucleation

The first studies of thin film dewetting were carried out with solutions of high molecular weight polymers. As a result, the thickness of the film did not attain values of less than 10nm. Dewetting of these films induced only one type of pattern, via the nucleation of holes of uniform diameter, randomly distributed over the surface. Jacobs *et al.* [65] demonstrated that the presence of defects, such as dust or trapped bubbles of air, could lead to what they called "heterogeneous nucleation" (Fig. 2.5(a)).

As observed by Jacobs *et al.*, thick metastable and unstable films can undergo dewetting in the presence of heterogeneously distributed defects (dust,

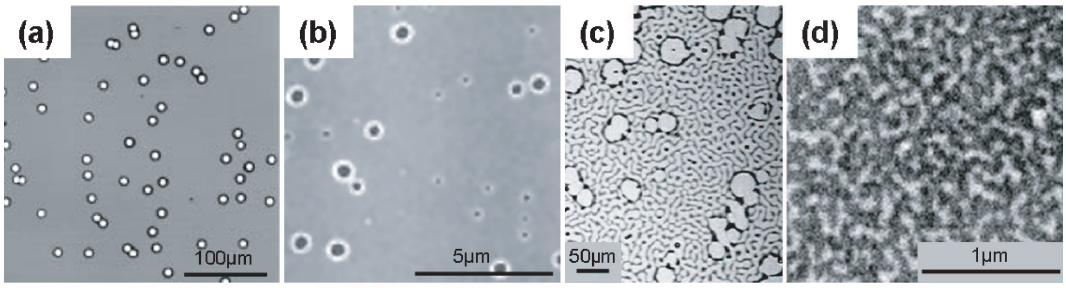

Figure 2.5: *(a) Heterogeneous nucleation in a thick (47nm) polystyrene (PS) film following annealing [65]; (b) Thermal nucleation in a 4.1nm PS film [64]; (c) Combination of defect-induced nucleated holes and spinodal dewetting [66]; (d) Bicontinous surface pattern following annealing of a 4.5nm PS film and first identified by Xie et al. as spinodal dewetting [67].*

defects on the substrate's surface, etc.). Several holes nucleate within a short time period, leading to features that have no correlation in space but exhibit very similar sizes. This is characteristic of *heterogeneous nucleation*.

2.2.2 Thermal nucleation

Another type of nucleation can occur in metastable films for thicknesses close to the local maximum of the interface potential curve. At this point, the activation energy necessary to overcome the barrier is small. As a result thermal fluctuations can be sufficient to alter the stability of the film and induce the nucleation of a hole. In this case, nucleation occurs randomly both in space and time, and the resulting features show no correlation in location or size. This is characteristic of *thermal nucleation* and illustrated in Fig. 2.5(b).

2.2.3 Spinodal dewetting

The term "spinodal dewetting" is derived from "spinodal decomposition", which describes a phase separation phenomenon (or "demixing") in mixtures

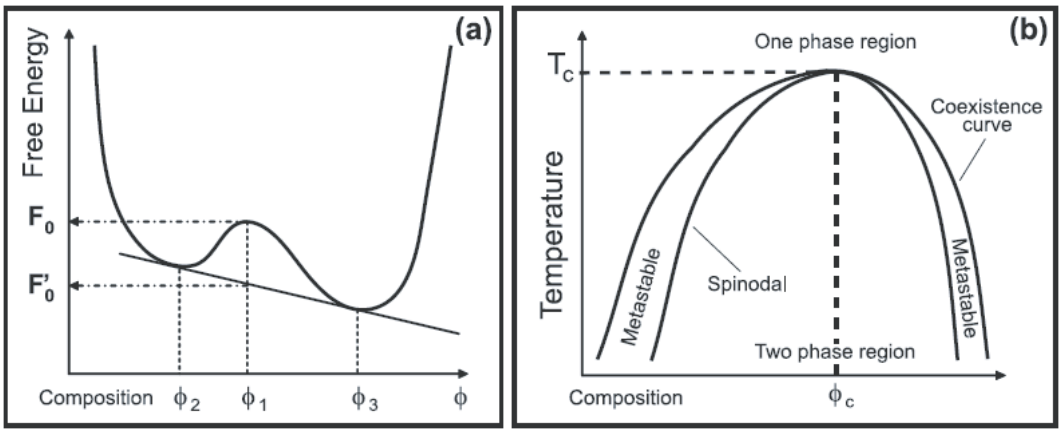

Figure 2.6: *(a) Shape of the free energy curve as a function of the composition of a mixture of two polymers in the case where demixing occurs via spinodal decomposition. (b) Phase diagram of the mixture showing the coexistence and the spinodal curves, which separate respectively the stable from the metastable phase and the metastable from the unstable phase. Spontaneous phase separation - "decomposition" - occurs below the spinodal line, where the mixture is unstable with respect to small fluctuations. From [50].*

of two materials (e.g. polymers). Let us consider the free energy of such a system as a function of its composition. If the free energy shows a local maximum, such as shown in Fig. 2.6(a), at that point the system is unstable, i.e. very sensitive in the face of small fluctuations in density or composition. The system can reach a more energetically favourable state by "decomposing" into two phases. This phenomenon is called *spinodal decomposition*.

A "phase diagram" can thus be established for the mixture of polymers, as shown in Fig. 2.6(b). One can define the "coexistence curve", separating a stable state (one single phase) from a metastable state, and the "spinodal curve", separating an unstable state (two phases) from a metastable state. The intermediary, or metastable, state is stable unless it overcomes a given activation energy via a perturbation. For a critical value of both composition and temperature, the two curves defined above intersect and the mixture

undergoes *phase separation*.

The particularity of spinodal decomposition is that it occurs with a *preferred length scale*. The fluctuations that develop within an unstable film span a large spectrum of wavelengths, but they do not all grow at the same rate. Short wavelengths are associated with a high energetic cost due to the large surface area that they create. As a result, they are promptly smoothed out. Long wavelengths, on the other hand, are favoured by the smaller amount of new surface area that they require, but the transport of matter that is necessary in order to "nourish" the growing perturbation must occur over very long distances, which slows down the growth process considerably. Consequently, the balance of these limitations leads to a local maximum growth rate, and thus to a preferred length scale, that associated with the selected wavelength [68].

The presence of a characteristic length scale is key in both the spinodal decomposition process and *spinodal dewetting*. The terminology for the latter is directly derived from the former and the "phase separation" analogy is sometimes preserved as well, although it is not universally adopted. Spinodal dewetting takes place in a binary fluid whose free energy curve is non-monotonous. In conditions where the film is unstable (refer to the introduction of this section and Fig. 2.4), a perturbation with a given wavelength develops faster than the others. Under the effect of this perturbation, the film ruptures homogeneously in both space and time, leading to features that are strongly correlated both in size and shape. From a uniform film, the system is changed into a set of isolated droplets.

Until extremely thin films ($\leq$10nm) were first studied, there was very limited evidence of spinodal dewetting. It was observed combined with nucleated

growth by Herminghaus *et al.* [66] in 1998 (Fig. 2.5(c)). Xie *et al.* [67] then presented an extensive study of a spinodal system, where early stage dewetting exhibited a bicontinuous surface pattern that they identified as being spinodal (Fig. 2.5(d)). They assumed that there was a crossover thickness for which both processes combined before switching to one or the other.

The rupture of the film takes place when the amplitude of the undulation becomes comparable to the thickness of the film, which in the case of spinodal dewetting happens extremely rapidly because of the exponential growth of the fluctuations in the early stage of the process. As a result, spinodal dewetting is a much faster process than heterogeneous nucleation.

2.2.4 Marangoni effect

The formation of patterns and / or the rupture of dewetting liquid films can also be the result of what is called a Marangoni effect [3, 69]. Instabilities in liquid films create surface tension gradients, from which pattern formation is originated, as was first observed by Bénard in 1900 [8]. Bénard showed evidence of convective flow formation in liquid films exhibiting hexagonal patterns, which was described much later theoretically by Block and Pearson as surface tension induced convection [70, 71]. Bénard-Marangoni instabilities, as they are named, generally lead to the formation of hexagonal patterns and hole nucleation in fluid films of volatile solvent deposited onto a solid substrate: this is referred to as the Marangoni effect. There is a difference of temperature between the surface of the substrate and the free surface of the liquid. This difference gives rise to a gradient of temperature through the liquid which does not conduct heat perfectly. As a result, a very small disturbance will create

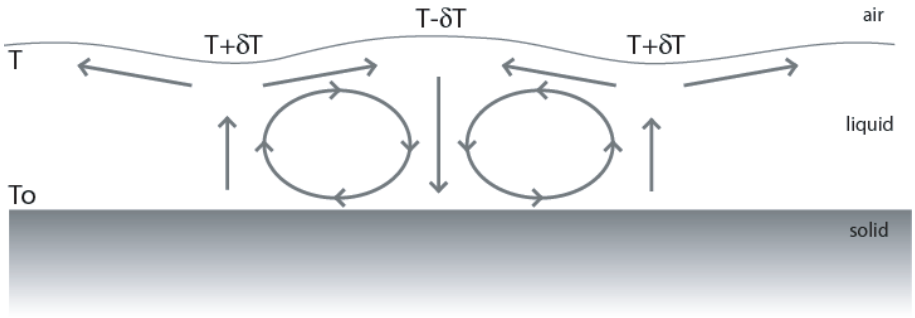

Figure 2.7: *Schematic of the Marangoni effect.*

an instability in the shape of "hot" and "cool" regions throughout the liquid film. The interfacial tension γ is dependent on temperature (and, as discussed below, solute concentration) and will increase wherever the temperature decreases, meaning the local temperature gradients will create regions of low and high interfacial tension. The minimum of surface energy $E = \gamma S$ is then obtained by decreasing the areas of the cold regions (S) where γ is high. This creates a movement of the fluid at the surface from hot to cold places. Since the liquid cannot accumulate locally at the surface, it will move downwards and some liquid will flow upwards to compensate this displacement of matter. As a result, hot places are fed by hot liquid from below, which enhances the initial instability and ends up creating convective flows through the film, as shown in figure 2.7.

Hexagonal patterns constitute a stationary state of this convection movement. The Marangoni number is a quantitative parameter which characterises the state of the system undergoing such a perturbation. It is dimensionless and given by equation 2.5 [3]:

$$M_a = \frac{B\Delta T h}{\rho \nu \kappa} \tag{2.5}$$

where B represents the variation of interfacial tension with temperature ($-d\gamma/dT$), h is the thickness of the film, ρ is the liquid density, ν its dynamic viscosity and κ its thermal diffusivity. The fluctuation is therefore enhanced by a variation of temperature, an increase of the thickness and/or a variation of interfacial tension. On the contrary, it can be inhibited by increasing the thermal diffusivity and viscosity of the fluid. From this equation, it is possible to establish a critical Marangoni number M_c below which instabilities do not occur. Far from M_c, the Marangoni number is given by $M_a = 8\alpha^2$ where α is the periodicity of the convective movement [3]. A definition of the characteristic wavelength of the instability is then :

$$\lambda = \frac{2\pi h}{\alpha} \tag{2.6}$$

For very thin films (where the gravitational effect can be neglected) or for very low interface tensions, long wavelength Marangoni instabilities take place. Such films have a thickness of the order of the amplitude of the "convection waves". For these films, it is possible that the Marangoni effect could produce film rupture by the creation of nucleation holes. To conclude the subject of Marangoni instabilities, it is important to note that the presence of nanoparticles in the liquid disturbs this process. Indeed, it induces a gradient of concentration during the evaporation process, whose effect is similar to that of the temperature gradient described above. As a result, the gradient of surface tension, from which originates the Marangoni effect, will be strongly

influenced by the concentration and size of the nanoparticles [72].

2.3 Colloidal nanoparticle science : background studies and challenges

Sections 2.1 and 2.2 introduced some of the physics, namely that of mutual body interactions and dewetting, that we will need to refer to in order to explain pattern formation in colloidal nanoparticle assemblies. Our analysis must also rely on previous work on similar systems. This section presents a background study of advances in the domain of colloidal nanoparticle science in the past decade or so, with an emphasis on metallic clusters, which will be of interest here.

2.3.1 Long-range ordered arrays of colloidal metallic nanoparticles

Studies of solutions of colloidal nanoparticles, often called "nanofluids", predominantly concentrate on three types of materials : metals, semiconductors and transition metals. Semiconductor nanoparticles, in addition to their obvious specific electronic properties, present much interest for optics-based applications, for instance. Transition metal nanoparticles are often exploited for their nanoscale magnetic properties. For the purpose of this thesis, I shall exclusively discuss the use of metallic colloidal nanoparticles, and in particular of gold nanoparticles, the studies of which represent a very large majority of the work carried out in this domain.

Superlattices of metal clusters

There exist two types of colloidal nanoparticles : charge-stabilised clusters, usually synthesised in aqueous phase (see Section 3.1), and ligand-passivated, or "functionalised", particles. The latter can be the result of two synthesis processes : they originate either from a gas-phase synthesis and a subsequent solution-phase encapsulation, or can be entirely synthesised in liquid phase (see Section 3.1). The result is a suspension of facetted metal clusters of anything up to several thousands of atoms, passivated with a layer of adsorbed organic molecules that keep them apart in solution.

Arrays of gold nanoclusters separated by gaps or organic ligands (i.e. capacitively coupled metallic dots) constitute a standard model for the study of electronic transport properties [43]. Coercing gold nanoparticles to assemble into well-ordered close-packed matrices has therefore been one of the ambitions of nanofluid specialists for the past 12 years, since Andres *et al.*'s observations in 1996 [42].

Andres *et al.* obtained close-packed arrays of 3.7nm thiol-passivated gold nanoparticles with long-range order, as shown in Fig. 2.8. They noticed that charge-stabilized nanoparticles did not easily form close-packed arrangements due to the fact that they repelled each other too much. They used gas-phase synthesised particles, afterwards passivated with alkyl-thiol ligands and spin-casted onto graphite, MoS_2 or SiO_2 substrates. The passivating molecules are found to interpenetrate, since the average spacing between particles was found to be 5nm (instead of the expected 6.1nm).

Andres *et al.*'s paper marked the beginning of the success of thiol-passivated gold nanoparticles associated with their apparently easily-controlled ability to

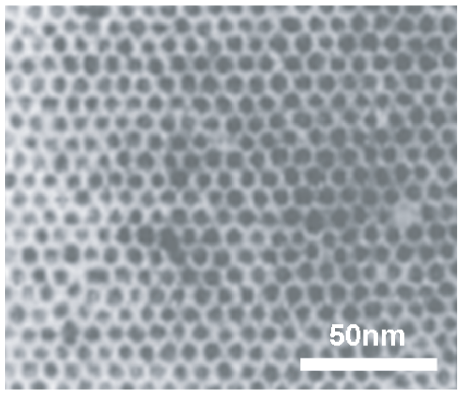

Figure 2.8: *TEM micrograph of a superlattice formed by spin-casting 3.7nm thiol-passivated (initially from gas-phase synthesis) gold nanoparticles on an MoS_2 surface [42].*

self-organise into well-ordered close-packed monolayers. The fact that many groups are still trying to master this self-organising process today shows (i) that Andres *et al.*'s experiment was a major achievement and (ii) that the potential of these systems to be used on an industrial scale to constitute tomorrow's single-particle electronic devices still needs to be fully investigated and controlled.

Binary assemblies of particles: alloy superlattices

The results discussed in the previous section opened the way to all sorts of manipulations on nanofluids. Another major achievement was the work by Kiely *et al.* between 1998 and 2000 [26, 73], which led to the fully-controlled creation of the first nanoparticle alloys. Kiely *et al.* used mixtures of decanethiol-passivated gold particles (synthesised in liquid phase) of different, well-defined sizes, to form well-ordered 2D bimodal arrays which they considered as nanoparticle "alloys". The maximum area of the layers formed was about $1\mu m^2$ and presented a perfect regularity of the nanoparticle arrangement (called

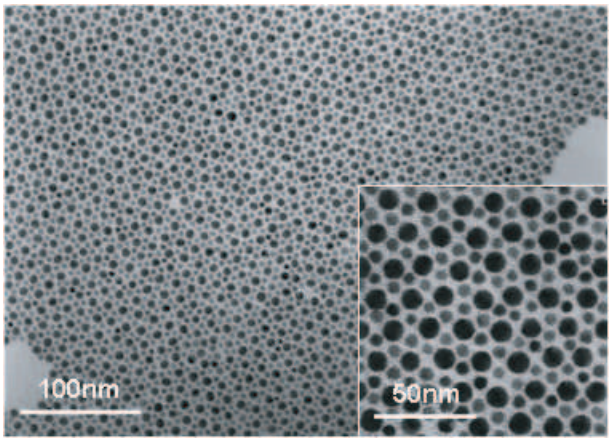

Figure 2.9: *TEM micrograph of a binary superlattice formed by thiol-stabilised Au nanoparticles of two different sizes (with a size ration of 0.58 (close-up view in inset) [26].*

"AB_2 stochiometry", see [26]) (Fig. 2.9). They found that this configuration only occurred for a narrow range of values of the ratio of the particle radiuses. For different values of this ratio, either random alloys (for nanoparticle sizes that are very similar) or size-segregated regions form. All three configurations exhibit a dense packing of the particles and a high degree of order over areas up to a square micron. The term "phase separation" was employed to describe the segregation by size of the particles, and it was suggested that this very peculiar self-organisation derived from an entropy-driven mechanism.

The degree of control that Kiely *et al.* demonstrated on the formation of these close-packed bimodal arrays was one never achieved thus far. Two years later, using the same technique, they managed, to a certain extent (150nm×150nm), to create "real" alloys of nanoparticles, i.e. controlled assemblies of nanoparticles of two different materials, namely gold and silver [73]. Both these fascinating results have contributed to developing interest in self-organised bimodal structures.

Close-packed layers of gold particles

We shall not, however, be looking at these bimodal structures here. We will concentrate on close-packed monolayers of a single type of particle, namely thiol-passivated gold nanocrystals. In 2001, Lin *et al.* [74] managed to create well-ordered arrays of such particles over an area of several square microns by drop deposition and evaporation, and by adding an excess of thiol molecules to their solution (Fig. 2.10). Thus, they improved the results obtained by Andres *et al.* five years earlier [42], but also proposed for the first time a possible mechanism of formation of these monolayers. Their assumption is that the superlattices form in solution, at the solvent-air interface, during evaporation [74, 75]. They suggested that the slowing down of the evaporation associated with the presence of low-volatility excess thiol gave enough time for the particles to self-organise before being deposited on the surface as the contact line of the drop finally depins and retreats towards the centre of the sample. The solidity of the close-packed monolayers is believed to prevent them from being damaged during the final stage of evaporation.

However, they revised their proposition a few years later, via a paper by Bigioni *et al.* [76]. In 2006, they were able to directly observe by optical microscopy the formation of close-packed monolayers at the solvent-air interface. At this stage, they were able to produce millimetre scale defect-free monolayers of gold nanoparticles, which constituted a major improvement. However, they expressed a different opinion concerning the role of excess thiol in solution and evaporation duration. Indeed, they stated that too long an evaporation process would impede the formation of close-packed layers. A necessary condition turned out to be that particles should be rapidly segregated at the solvent-

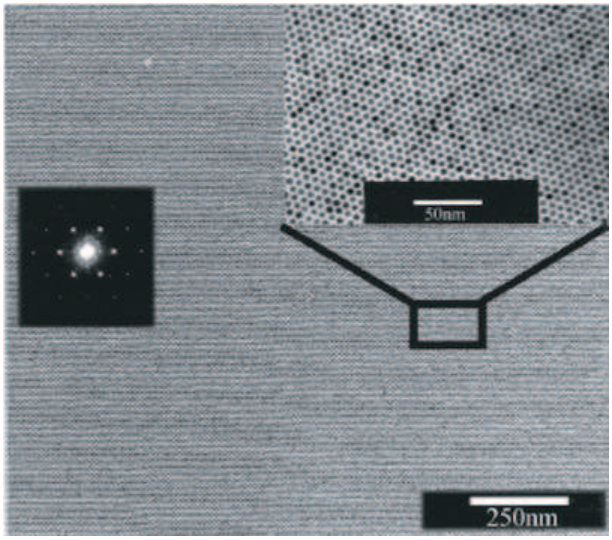

Figure 2.10: *TEM microcgraph of a long-range-order superlattice formed by dodecanethiol-passivated 5.5nm Au nanoparticles. The left inset shows the FFT diffraction pattern of the image, the right inset is a close-up view [74].*

air interface, which only happened in a fast enough evaporation. The role of excess thiol, thus, was redefined and it was suggested that free thiol molecules intervened in the particle-interface interaction. In the presence of excess thiol, particles are allowed to move towards the interface faster, thiol molecules playing the role of "nucleation sites" for flat islands of particles to form and grow, finally coalescing into one very large close-packed monolayer [76].

Lin and Bigioni and their co-workers offered a simple and reliable technique to produce large-scale close-packed monolayers of gold nanoparticles, which was a significant breakthrough. An example of a very direct application of their technique is described below, which exploits the conduction properties of nanometre-scale thiol-coated gold particles. However, we shall see in the next chapters of this thesis that reproducing Lin and Bigioni's experiments is not trivial and that the mechanism they proposed, although it may be correct for their own specific experiment, deserves to be reappraised in some of the cases

with which we will be concerned.

Applications: electrical transport though arrays of metallic nanoparticles

If we were to discuss all the possible applications related to the electronic properties of gold nanoparticle arrays, there would doubtlessly be enough material to write a complete new chapter. However, it seems necessary to describe these properties to some extent here, since they will not be discussed at length in what follows (it was explained earlier that this work focused more on the mechanisms of pattern formation than on its possible direct applications).

To be concise, Middleton and Wingreen developed a model in 1993 [43] which described electronic transport through an array of capacitively coupled metallic dots. They found that these arrays should exhibit a Coulomb blockade behaviour, which means that successive thresholds in voltage must be overcome for current to flow through the successive dots within the array, due to the presence of the tunnel barrier between the dots. Not only do arrays of thiol-passivated gold nanoparticles correspond to Middleton and Wingreen's system, but they also exhibit single electron charging due to the dimensions of the particles (the charging energy of an individual nanoparticle is inversely proportional to its capacitance, i.e. to its radius, see [43, 47, 48]). All the details of these mechanisms can be found in various reports and articles, including [43], [44], [47], [48], [77], [78], [79]. In a 2D array of such dots, charge transport progresses as a front that is displaced as a function of the applied voltage. This is illustrated in figure 2.11. Once the conduction front reaches the opposite electrode in one point, a channel of conduction opens. More and

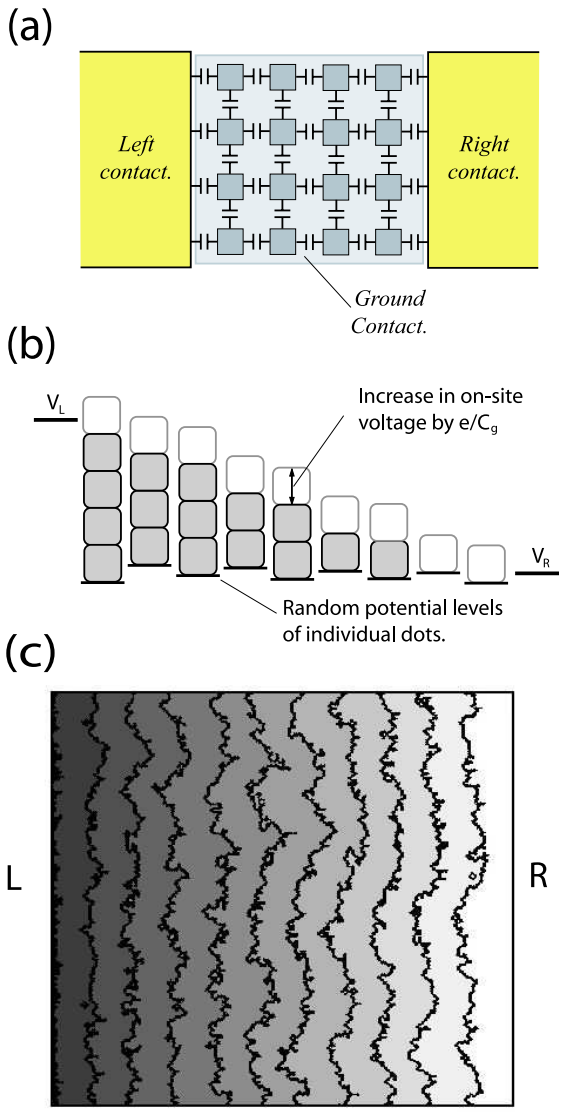

Figure 2.11: *(a) Schematic of an array of capacitively coupled metallic dots, between left and right contacts (V_L and V_R) and an underlying ground contact (V_g). (b) Charge flow through an array of metallic dots : for a value of the bias less than the threshold voltage for the 1D array, electrons will be transferred on the first dot as allowed by the value of the applied bias and will then move progressively through the array according to the potentials of the adjacent dots, until the bias becomes insufficient (here to transfer an electron from the 7th to the 8th dot). (c) Advancing front of charge through a 2D array of metallic dots for different voltages below the threshold of the array. Adapted from [43].*

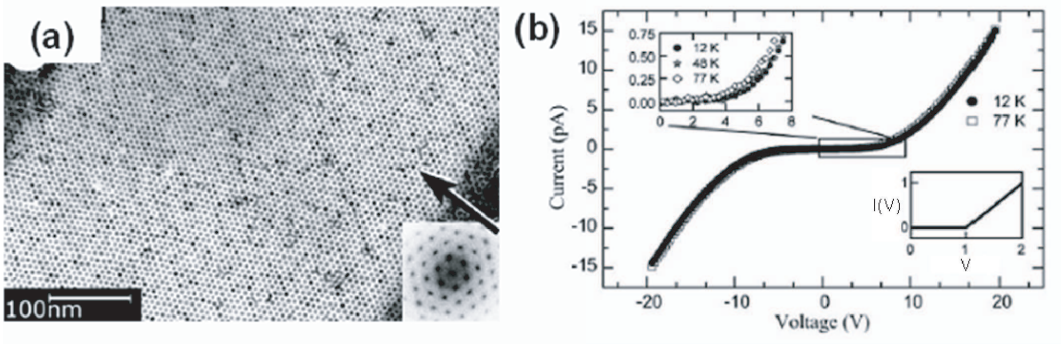

Figure 2.12: *(a) Highly ordered superlattice of 2-3nm gold nanoparticles (and 2DFT) (b) shows the I(V) characteristics they obtained for a 330nm×2μm array. The upper inset magnifies the region near the voltage threshold of the array and the lower inset is a schematic of the ideal I(V) curve for a single nanocrystal. From [44].*

more channels open as the voltage is increased further, until all the thresholds in the array are overcome [43, 79].

In 1996, Andres *et al.* already had observed the expected Coulomb blockade effect for Au monolayers. Later, following Lin *et al.*'s success at forming larger-scale monolayers, Parthasarthy *et al.* [44] studied the effect of structural disorder on electrical transport (Fig. 2.12) and, a little later, the effects of temperature [45], soon complemented by Blunt *et al.* [48], so that nowadays, we have a better understanding of the mechanism of transport through gold nanoparticle arrays. However, conduction channels such as those described by Middleton and Wingreen [43], or Reichhardt and Olson Reichhardt 10 years later [79], have not yet been directly observed experimentally.

2.3.2 Pattern formation and selection

The previous section dealt with long-range ordered arrays of nanoparticles, for the now obvious application opportunities that they might represent. In this

section, we focus on the process of pattern formation in nanoparticle assemblies, and on the route that it provides to effectively control the connectivity or geometric order within nanoparticle lattices.

Rings of nanoparticles

A common feature that appeared very early on in studies of nanoparticle assemblies is the nanoparticle ring. In 1998, Ohara *et al.* [2] reported the formation of such patterns in assemblies of 3nm particles deposited from hexane, as shown in figure 2.13(a). They discussed the effects of solvent dynamics, evaporation rates and nanoparticle concentration on the formation and growth of nanoparticle rings. They correlated the occurrence of these sub-micron size rings with *hole nucleation* in the ultra-thin liquid film and the effect of *disjoining pressures* at the substrate interface. As the hole grows, particles are collected at the rim and cause contact line pinning as their local concentration increases, forming the observed rings (illustrated in Fig. 2.13(b)).

However, shortly after that, Maillard *et al.* [3,69] reported the formation of micrometre size rings and hexagons in assemblies of charge-stabilised particles (Fig. 2.13(c)), which they associated with a convective flow, namely a *Bénard-Marangoni instability*, as described earlier in section 2.2.4 (Fig. 2.13(d)). They stressed a number of important points. First, according to them, rings are not due to a dewetting process and nucleation (this issue was re-examined by Rabani *et al.* [1] and Moriarty *et al.* [21] later, see below), rather they originate from this convective instability (whose effect decreases as the evaporation is slowed down, in which case the distribution of particles on the surface becomes random). This instability emerges from a gradient in temperature and con-

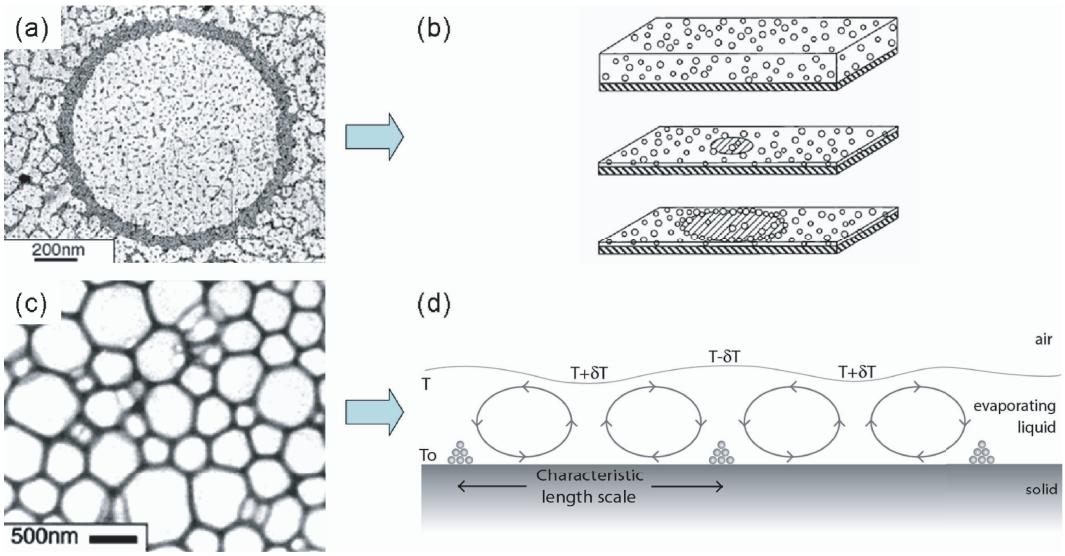

Figure 2.13: *(a) A nanoparticle ring, from [69], and (b) the process of hole nucleation and dewetting from which nanoparticle rings are believed to originate, from [2]. (c) A honeycomb of hexagonal nanoparticle cells, from [3], and (d) the Marangoni convection effect that created them, adapted from [72].*

centration that are created by the evaporation process itself. Second, rings become more hexagon-shaped as the size distribution of the particles is narrowed. However, the *occurrence* of rings depends neither on average nanoparticle size and size distribution, nor on the nanocrystal shape. Third, the long-range convective effect accounts for the formation of long-range ordered nanoparticle honeycomb arrays (see Fig. 2.13(c)), which cannot be understood solely in terms of local (short-distance) interactions and effects.

The contributions of both dewetting processes and convection flows to pattern formation was clarified by Stowell and Korgel [72], who analysed the mechanisms at play when the observed patterns evolved from isolated rings to honeycomb structures. They highlighted the effect of concentration on the microscopic morphology of the assembly, from rings at high concentrations, to polygonal and then ordered hexagonal networks, to arrays with no structural

order at low concentrations. They contradicted Ohara *et al.* on the fact that polydispersity and size influenced the creation of rings. However, they acknowledged the role of disjoining pressure and contact line pinning in the ring formation. For lower concentrations, this depinning does not occur and pattern formation is thus dictated by other contributions, such as a convective flow. They confirm that hexagons originate from a Marangoni instability, in which case particles re-arrange in the most energetically favourable configuration. The fact that this configuration sometimes adopts the shape of hexagons confirm the presence of long-range forces such as those associated with Marangoni convection flows. In addition, rings and honeycombs are sometimes seen coexisting in the same area, which suggests that *the evaporation proceeds in two stages, one involving dewetting and disjoining pressure, the other one resulting from convective effects.*

It is thus interesting to see how two different ideas can evolve in parallel to finally lead to a rather complete interpretation of ring formation in nanoparticle assemblies. The experimental investigation of the conditions that lead to given nanoparticle arrangements provides a solid basis for critical analysis and draws up a spectrum of configurations where several mechanisms may be present at different times or coexist. It will constitute the procedure generally adopted along the course of this work.

Spinodal phase separation and cellular networks of nanoparticles

The ability of colloidal passivated nanoparticles to form a variety of patterns was really first explored only recently, by Ge and Brus, in 2000 [80]. They attributed this property to the strength of the interparticle interaction, which

is very weak in solution but becomes strong enough to induce aggregation as the particles are exposed to air following deposition and evaporation. As a result, they form various arrangements, from small isolated islands uniformly distributed on the surface for a fast evaporation, to ribbons formed of coalesced islands as the evaporation rate is reduced. These configurations correspond to a spinodal dewetting process [67, 80] (see Section 2.2.3). As the coverage of the surface by the particles is increased over 30%, a new range of patterns is observed : bicontinuous patterns and foam like arrangements (Fig. 2.14), up to layers with round voids and cracked layers. Ge and Brus drew some important conclusions. They mentioned that the characteristic length scale of the patterns grows as the evaporation process lengthens, which is of key importance for gaining control over the formation of patterns of given dimensions. They also note that assembly occurs at the substrate interface, not in solution. Note that this statement differs from that of Lin and Bigioni [74, 76], but also describes a different experiment, which may involve a different mechanism altogether. Obviously, both assumptions lead to completely different interpretations of the mechanisms at play and it is thus a major issue that remains to be solved. We will undoubtedly be faced with this discussion again in the course of this thesis (Chapters 4 and 5). Finally, a straight-forward but essential conclusion is that the patterns are dependent on the solvent used, considering that the transition between interparticle interactions through the solvent and interparticle interactions through air is going to play a role in the process of pattern formation. This description of the evaporation process for the first time introduces the idea of a quenched system, that is a system trapped in a non-equilibrium configuration.

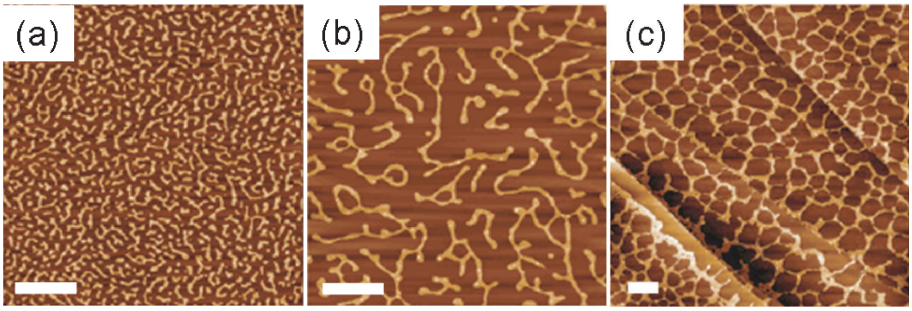

Figure 2.14: *AFM images of nanoparticle arrangements following deposition from chloroform-based solutions, with a coverage above 20% : (a), (b) spinodal-decomposition-like patterns forming a regular bicontinuous layer, (c) foam-like configuration, or cellular network. Scale bar represents 1µm. From [80].*

Ge and Brus's conclusions were, and still are, essential to the comprehension of the role of dewetting processes in pattern formation in assemblies of colloidal nanoparticles. However, subsequent works and points of view have since then complemented and refined their explanation and we are now in a position to elucidate the mechanisms of pattern formation in many more situations and systems. A few examples include the analysis of cellular network formation by Moriarty *et al.* in 2002 [21] and the development of a 2D model by Rabani and co-workers [1] (later modified by Martin *et al.* [81]) to account for most of the patterns observed when colloidal particles are deposited by spin-casting onto a solid substrate. Interestingly, Moriarty *et al.* state that despite what previous works had established [3, 72] (see above), cellular networks could not be due solely to a Marangoni effect. The presence of networks of smaller characteristic length scale within the branches separating the main network cells (Fig. 2.15(a-b)) suggests that a spinodal-like dewetting effect could coexist with the larger scale convection-induced evaporation process. They also set up a quantification method that establishes the degree of ordering of the nanoparticle arrangements (for instance, although the network is not

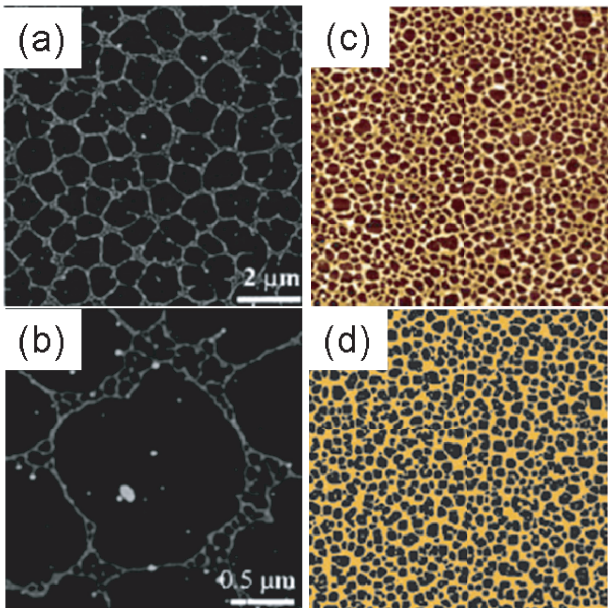

Figure 2.15: *(a) AFM image of a 2nm-Au-nanoparticle "foam" or cellular network on native silicon oxide; (b) close-up view, which shows the formation of cellular networks on a different length scale within the branches separating adjascent network cells. The scale is given on the images, from [21]. (c) Network formed by thiol-passivated nanoclusters deposited from organostannoxane (AFM scan 8µm×8µm); (d) equivalent simulated image using the 2D Monte Carlo algorithm (image 3µm×3µm). From [81].*

ordered in the long range, there exists a preferred intercellular separation and statistically, cells are almost perfectly hexagonal on average) and incidentally, confirms that several mechanisms may be at play in the formation of these complex networks.

Based on these conclusions, a model emerged, initially developed by Rabani *et al.* [1] but adopted and adapted by others since then [81, 82], that matches experimental results and accounts for solvent fluctuations. It takes into account both homogenous and heterogeneous evaporation processes and relies on Ge and Brus's assumption that assembly takes place at the substrate interface. This model will be described in more detail in Chapter 5. In its original

version, this 2D model can account for and even predict, to a certain extent, pattern formation in far-from-equilibrium assemblies of gold nanoparticles.

Controlling nanoparticle organisation

To finish this chapter on the mechanisms of pattern formation, it is important to stress the possible applications that can be derived from this type of study. Self-organised systems which exhibit electronic properties such as that of passivated gold nanoparticles represent a huge potential in the domain of microfabrication and microelectronics, since they do not require costly and time-consuming lithographic steps to arrange themselves into ordered structures. Transferred to single particle transistor technologies, for example, these systems have the potential to be revolutionary. There is therefore a lot at stake when it comes to controlling particle organisation. However, this task is much more complicated than it seems at first.

One can control the organisation of particles by controlling the deposition technique. This, we will see, has motivated a large part of the research presented here. It was mastered to an impressive degree of control by at least two groups in the last couple of years. By using a Langmuir-Blodgett deposition process, Huang *et al.* [83] managed to create regularly spaced 1D lines of single particle thickness, with various materials and different particle sizes up to the micrometer scale. The position of the lines is determined by the slip-stick motion of the contact line. Arrays of lines and grids were obtained, that served as a template for the growth of silicon nanopoles (Fig. 2.16). Simultaneously, Xu and co-workers [84,85] obtained gradient concentric rings of particles (the ring height and annular thickness decrease as the diameter of the ring decreases)

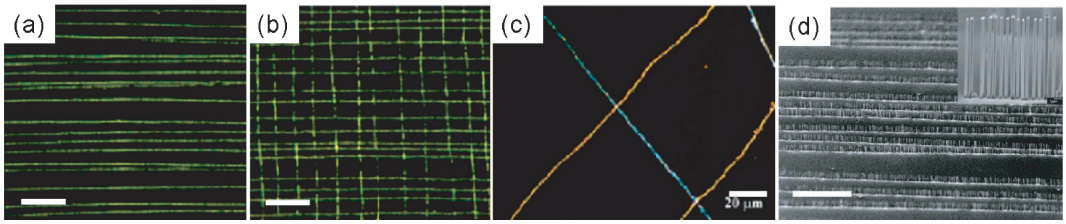

Figure 2.16: *(a) 1D line of gold nanoparticles after one dipping, (b) grid of 1D lines of gold nanoparticles after the second dipping, perpendicular to the first one, (c) grid of two lines of gold and silver particles obtained after two successive crossed dippings. (d) SEM image of an array of silicon nanopoles grown on top of 1D lines formed by gold nanoparticles (the insert shows a close-up view). Scale bars represent (a)-(b) 200µm, (c) 20µm and (d) 100µm. From [83].*

following controlled evaporation of the solvent in a sphere-on-flat geometry. There again, by achieving a fine control on the conditions of deposition, they could vary the ring thickness, height and separation with great accuracy. This ring geometry has been exploited in the work presented here, but in a different (i.e. meniscus) configuration (see Chapter 4).

Gaining perfect control over pattern formation is challenging. First of all, we need to be able to classify patterns as a function of experimental parameters, so that we can reproduce them faithfully. In the case where electrical transport is studied as a function of topology, as in the work of Blunt *et al.* [47, 48] for instance, it is necessary to control the long-range correlation in the array that is being studied. It is useful to be able to identify the experimental conditions that created these patterns in order to obtain a sufficient number of similar test samples, to offer a good statistics on experimental measurements. In their work, Blunt *et al.* classified the structural disorder as "correlated" and "uncorrelated". In this thesis, we propose a study that fully requires the same sort of classification and for which reproducibility is a major issue (see Chapter 5).

Finally, there are other ways of controlling self-organisation, and that is by influencing the environment of the nanoparticle solution : the solvent can be changed in order to modify the dynamics of evaporation and/or one can locally alter the substrate's wetting properties by alternating regions of different nature, as described for example by Martin *et al.* [86]. In configurations like this, it is the control exerted locally over the dewetting process that is reflected on the nanoparticle assemblies. In cases where these microscopic artifacts can be produced on a large scale, this technique represents a very efficient way of controlling nanoparticle organisation on a surface.

These techniques illustrate the potential of self-organising nanoparticles as tailored materials for specific applications. They were exploited and developed in the course of this research both for the purpose of obtaining model systems whose behaviour is dictated by principles that we can clearly identify, and for the possible future applications that they may underpin.

Chapter 3

Review of Experimental Techniques

"Au plan des principes : il y a plus d'originalité dans la fermeture éclair que dans bien des montages présents dans nos labos."

Pierre-Gilles De Gennes.

The previous chapters aimed at introducing both the importance of the concept of spontaneous pattern formation and some of the basic physical principles associated with this phenomenon, with an emphasis on systems of colloidal nanoparticles, or nanofluids. This chapter will present some of the technical aspects of nanoparticle synthesis and deposition, and will also cover a number of experimental conditions that are accessible in order to monitor and tune pattern formation in these systems.

3.1 Synthesis of gold nanoparticles

The system studied throughout the work described in this thesis is a solution of gold nanoparticles suspended in an organic solvent. The particles are clusters of gold atoms to which alkylthiol molecules have been attached (in a ratio 1:300 to 1:1000 typically) by adsorption in liquid phase, hence forming a passivating layer which isolates the particle from its neighbours. Thus, a colloidal solution of polydisperse gold nanoparticles is obtained (the relative size distribution depends on the kinetic of the chemical reaction and is typically around 15% in our case). The particles can be hydrophobic and suspended in toluene, or they can be made hydrophilic by simply modifying the termination of the alkyl chain of the passivating molecules, in which case they will be suspended in water or in another polar solvent. The majority of the work reported here has been carried out using hydrophobic particles. Hydrophilic particles were also synthesized and preliminary tests established that they exhibited properties reminiscent of those of hydrophobic particles (namely, self-organisational abilities, see later). Nanoparticles are synthesised according to well known procedures, as described below. They are then deposited onto a substrate, usually native oxide terminated silicon. During evaporation, the self-organisation of the particles into well-defined patterns occurs (whether assembly occurs in solution or on the surface will be part of the discussion in the next chapter). Depending on experimental conditions, a broad range of patterns can be observed [21, 80]. A series of measurements was carried out on these samples and on the assemblies of gold particles at their surfaces. Throughout the course of this work, nanoparticle morphologies were systematically investigated using

atomic force microscopy.

3.1.1 Two-phase synthesis of thiol-passivated gold nanocrystals: hydrophobic colloidal particles

The thiol-stabilised colloidal gold nanoclusters used here are synthesised according to the procedure developed by Brust *et al.* [87] in 1994. It is a two-phase synthesis procedure where the polar phase is constituted of "inverse micelles" of surfactant molecules in a non-polar solvent. An aqueous solution of gold salt is added, in which the $AuCl_4^-$ ions, charged, will seek the polar environment at the centre of the micelles to reach their lowest possible energy configuration. Gold ions are then reduced (with a solution of $NaBH_4$) in the presence of thiol molecules, thus allowing the passivation of the gold nanocrystals, which become stable in solution. The remaining steps of the procedure aim at cleaning and purifying the solution by removing all the residues of the chemical reactions still present in solution. This is achieved by precipitation of the nanoparticles in ethanol, after evaporation of the "polluted" toluene down to a very small amount. All residual products are soluble in ethanol whereas the gold particles are not and will therefore precipitate in large aggregates (the amount of residual toluene being too small to keep them in suspension). A filtering step is afterwards sufficient to extract the precipitate, which is then redissolved in toluene or other organic solvents such as alkanes (hexane, decane...), other benzene derivatives (benzene, mesitylene...) or halogenated solvents (dichloromethane, chloroform...). The cleaning steps can be repeated several times to ensure the solution is free of reaction by-products.

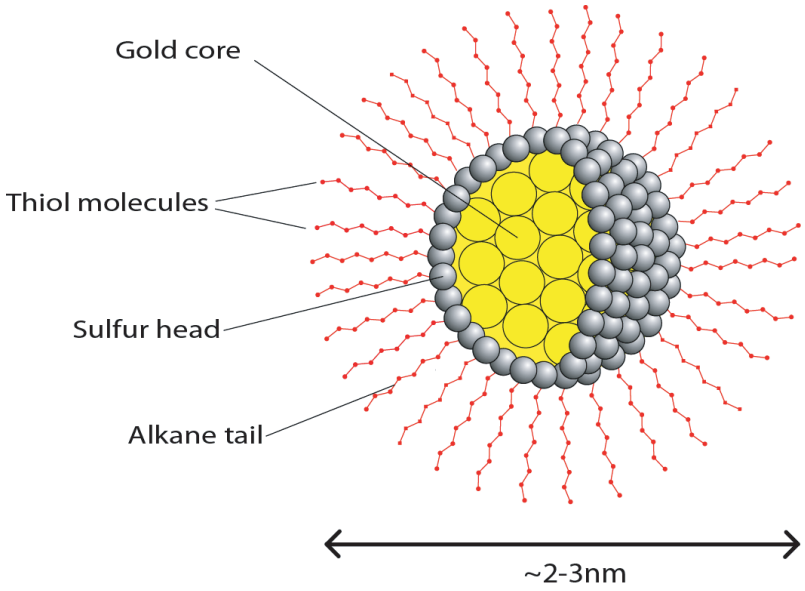

Figure 3.1: *Schematic of a thiol-passivated gold nanoparticle.*

The particles obtained are usually 2 to 3 nm in size (Fig. 3.1), although this can be easily tuned by a careful adjustment of the stoichiometric ratios of the reactants. Particles can be dried out of solvent and redissolved at will. The alkyl chains of alkylthiol molecules can be of various lengths : for the purpose of this work, alkyl chains from 5 up to 14 carbons were used. The passivating layer can consist of either alkylthiol molecules or other sulphur-terminated functionalised molecules, hence enabling a variation of the physical properties of the particles. This is the case for hydrophilic particles, as will be briefly described in the following section.

3.1.2 Alcoholic-phase synthesis of charge-stabilised gold nanocrystals: hydrophilic colloidal particles

Hydrophilic particles were prepared following 3 types of synthesis protocols. The simplest and quickest synthesis is known as the sodium citrate reduction method, or Turkevich method [88], which yields gold colloids fairly uniform in size, with a typical diameter of 14±1nm. A similar synthesis process in which reduction occurs via sodium borohydride rather than sodium citrate is used to produce 5±0.5nm gold colloids. From these preparations, hydrophilic gold nanoparticles can be obtained by simply adding the passivating ligands to the charge-stabilised gold colloids in water. Then the particles are cleaned and purified by centrifugation. The size distribution of the particles can also be varied in these processes. The ligand that is added consists of an alkanethiol molecule whose termination has been modified into a $-(O-CH_2-CH_2-)_4-OH$ or $-(O-CH_2-CH_2-)_4-COOH$ group for example [89, 90].

The third synthesis process is a single-phase preparation in alcohol solution [91] that yields 2−4nm hydrophilic particles by addition of a similar ligand. It is also possible to prepare those particles with the same 2-phase method as described in the previous section. The particles are transferred from the toluene phase to the aqueous phase in the last step of the synthesis when the hydrophilic ligands are introduced and progressively form the passivating layer around the gold clusters [90]. In all cases, particles are dissolved preferentially in water at the end of the process, but can be dried and redissolved at will in various polar solvents. All hydrophilic particles were synthesised in collaboration with Brust *et al.* in the Chemistry Department of

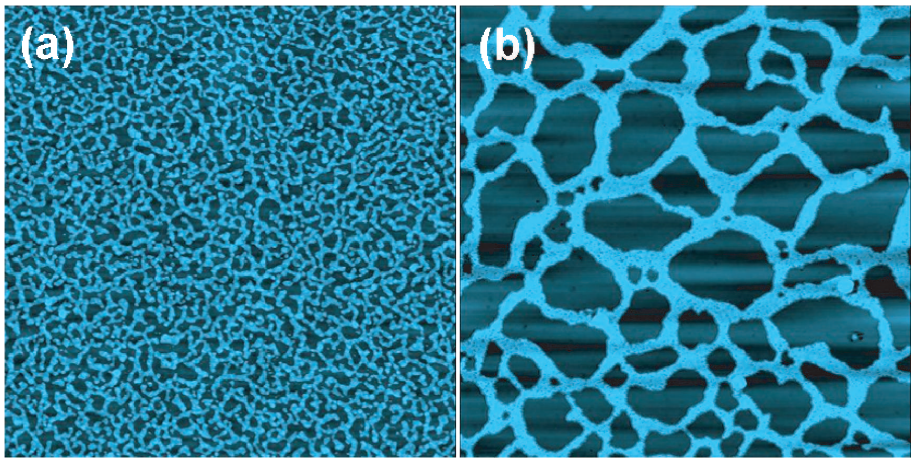

Figure 3.2: *AFM pictures of (a) 2-4nm hydrophilic gold nanoparticles spin-coated from a water-based solution and (b) 14nm hydrophilic gold nanoparticles deposited with the meniscus technique onto a native-oxide terminated silicon substrate (hydrophilic). Scan sizes are (a) $2\times2\mu m^2$ and (b) $5\times5\mu m^2$.*

the University of Liverpool.

A quick observation by AFM shows that hydrophilic particles exhibit a self-organising behaviour when deposited on silicon oxide. Figure 3.2 was obtained after deposition by spin-casting (see next section), and is very reminiscent of Ge and Brus's and Moriarty *et al.*'s results shown in Section 2.3, Fig. 2.14 and Fig. 2.15.

It is thus possible to vary the degree of hydrophobicity / hydrophilicity of gold nanoparticles, while preserving their self-organising behaviour. This opens the door to a whole new range of experimental parameters and experiments exploiting the wetting properties of both substrate and particles. Further work could at first involve particles of identical wetting properties, but various sizes, leading to possible patterning by size segregation or formation of bimodal well-ordered structures such as those observed by Kiely and co-workers [26]. Then, mixtures of particles of different wetting properties but

identical size could be studied and hopefully would form a different type of segregated regions. Combining these effects with those of a substrate where different regions exhibit different wetting properties [86] could considerably broaden the field of investigation of self-organisation in gold nanofluids and possibly enable us to achieve a never attained degree of control on pattern formation in such assemblies. However, this represents a considerable amount of experimental research and, as said earlier, is out of the scope of this thesis. Furthermore, preliminary experiments show that it is very difficult to control accurately the composition of nanoparticle mixtures. Indeed, finding a solvent that will keep both types of particles (hydrophobic and hydrophilic) in suspension is already an obstacle to these experiments. Controlling the degree of hydrophobicity / -philicity of particles and their solubility in various organic / aqueous solvents is essential to allow uniform spreading on the surface and avoid liquid demixing during deposition.

Another approach consists of mixing two different types of particles in two different (miscible) solvents, which would by-pass the problem of finding a unique solvent. However, this system becomes extremely complex and the mechanisms at play in pattern formation very intricate. All these parameters offer a glimpse of the fantastic degree of complexity that will need to be overcome and mastered in order to gain control over the formation of these assemblies, but also illustrate the numerous paths that can be exploited in order to achieve such an aim.

3.2 Techniques of deposition onto a solid substrate

The goal of this project is to observe, characterize and understand the organisation of nanoparticles deposited from a suspension onto a solid substrate. The particles are suspended in a volatile solvent. After the evaporation of the solvent, the particles have spread over the complete surface and appear to spontaneously form assemblies by the process called self-organisation that we have discussed earlier. The purpose of this section is to describe the various techniques that can be used to deposit the particles onto the substrate and, more precisely, the different ways the solvent can evaporate, leaving the solute on the substrate.

3.2.1 Far-from equilibrium configuration: spin-coating

The most widely used technique for depositing a solution onto a solid substrate is spin-coating. This process can be used to deposit single-phase solutions of various viscosities, and is particularly adapted in the electronic device fabrication industry for the deposition of photo-resists for lithographic processes, for example. In this technique, a certain quantity of the solution (typically a few tens of microliters for a $1cm^2$ sample) is first deposited on the substrate so that the drop of solution is pinned to the sample edge (Fig. 3.3(a)). The substrate is then spun at a chosen speed up to a few thousands revolutions per minute (rpm, typically 3500 to 4000rpm in our case). For well-chosen spinning speeds and durations, the layer obtained is flat and homogeneous over the entire substrate. The thickness of the film depends on the speed and duration of

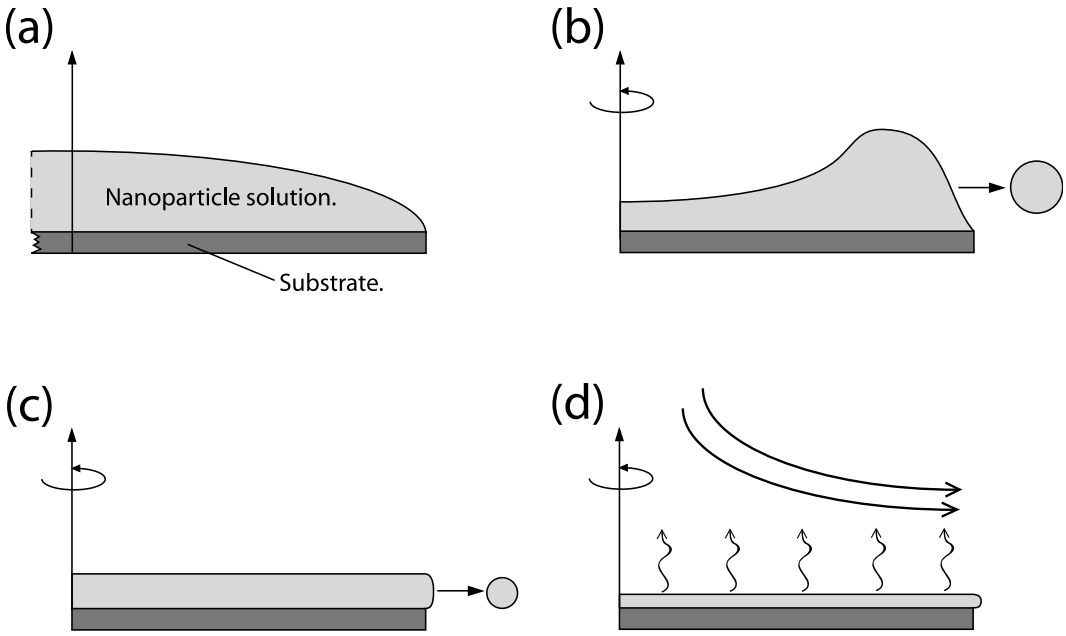

Figure 3.3: *The spin-coating process. Adapted from [47].*

the deposition. The process itself allows a very fast evaporation of the solvent, particularly in the case of a volatile solvent (just a few seconds for toluene in our case). The first stage of the spinning gets rid of the excess of solution on the surface (Fig. 3.3(b)), until the fluid has reached the same velocity as the substrate and rotates along with it. Then the layer of liquid is flat and its thickness decreases regularly by a radial flow (and ejection) of solution towards the edge of the sample (Fig. 3.3(c)). In the final stage of the spinning, the elimination of solvent by the effect of the radial acceleration is minimum and the solvent starts to evaporate (Fig. 3.3(d)), increasing the concentration of the solute in the thin layer until dewetting occurs. This process ends when all the solvent has evaporated / dewetted from the surface, which is then covered with one or several layers of particles.

Once the particles are on the surface (in the absence of solvent), they are

strongly physisorbed and immobile, and cannot be removed without further treatment, meaning the assemblies thus obtained can either be the result of aggregation during evaporation or due to the final dewetting stage. This is an important point, because there still exists a debate today to determine whether the mechanism of self-organisation generally occurs at the solvent-air interface [74,76] or at the solvent-substrate interface [1,81,92] or is a combination of the two. Although not very relevant to spin-coating (the evaporation takes place so quickly that all these processes would happen on the same time scale and thus would most certainly be impossible to distinguish), this issue applies in a much more critical manner in the deposition techniques that will be described below, where the evaporation time is much longer than a few seconds. As a consequence of the duration of the evaporation, spin-coated samples will be referred to as "far from equilibrium" systems, due to the fact that the drying is very quick, hence kinetically trapping the particles (the system is "quenched") into a non-equilibrium configuration [21, 80]. Other techniques are intended to prepare samples in conditions which are closer to equilibrium (although, importantly, not *at* equilibrium, since a drying drop is intrinsically a non-equilibrium system).

3.2.2 Drop deposition and coffee-stain effect

The most straight-forward technique to deposit a liquid onto a flat solid surface is to leave a drop of solution to evaporate from the surface in open air. The disadvantage of this technique, as has been experienced repeatedly, is the stains that drying drops leave on the surface. The thick line that forms at the edge of a drying drop due to the local accumulation of solute as the liquid evaporates

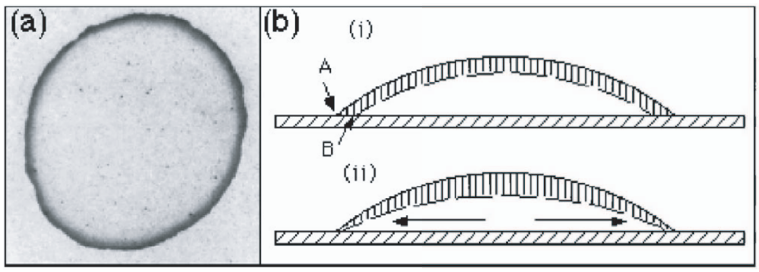

Figure 3.4: *(a) Photograph of a typical "coffee stain" left behind by a 5cm diameter drying drop of coffee. (b) Schematic of the dynamics of evaporation of a drop : (i) if the contact line is not pinned, it retreats from A to B and the evaporation is uniform over the whole surface of the drop, whose shape varies from the full line to the dashed line (the hashed layer evaporates); (ii) if the contact line is pinned (solute is locally adsorbed on the substrate), the contact line does not retreat and a flow is created (arrows) to compensate the loss of fluid. From [94].*

is commonly called the "coffee-stain" effect. A comprehensive study has been carried out by Deegan *et al.* on the dynamics of drying drops [93, 94], in particular on the self-pinning of the contact line with the substrate, from which originate coffee-stain-like drying lines (Fig. 3.4).

These residual stains often represent very large multi-layered aggregates of particles which are not of much interest for our study. As a result, this drop-deposition technique has to be used in a very controlled way in order to obtain homogeneous layers of evenly spread particles over sufficiently large areas. There exist a few examples of controlled drop deposition, in particular, the work by Lin *et al.* and Bigioni *et al.* described earlier [74, 76], where the evaporation of the solvent was controlled by adding some chemicals to the solution. They suggest that surfactants in excess move towards the solvent-air interface driven by their amphiphilic properties (apolar head / polar tail), hence forming a uniform layer at the exposed surface of the solution drop that supposedly facilitates the migration of the particles towards this interface [76].

In this case, and under very strict experimental conditions, the solvent can evaporate steadily and homogeneously from the substrate, without undergoing the usual early dewetting process and leaving time for the particles to move freely in the solution and to organise themselves into assemblies with a high degree of ordering.

3.2.3 Moving towards equilibrium: meniscus-driven evaporation

As proven by experience, the slow and steady evaporation of a drop of solution in air is a very tedious experiment to reproduce. The major part of the first year of this project has been dedicated to finding a systematic way to control the evaporation of the solvent with a good reproducibility. A novel technique for nanoparticle deposition was inspired by previous work on polystyrene spheres [51, 95]. For a solvent with appropriate wetting properties, such as toluene, a Teflon ring can be used for creating a meniscus of solution rather than a drop (Fig. 3.5). Indeed, the wetting properties of the [solvent - Teflon ring - substrate] system are such that the affinity of the solvent with Teflon is higher than that with silicon oxide (the samples onto which the solution is

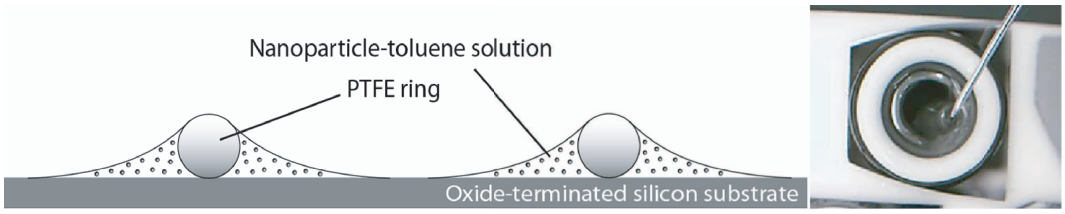

Figure 3.5: *(left) Schematic of the meniscus formation: (right) photograph of the nanoparticle solution being injected inside an 8mm (ID) PTFE ring lying on top of a silicon substrate.*

deposited in this study are native oxide-terminated silicon substrates), hence the formation of a meniscus.

Consequently, as it evaporates, the solvent now retreats from the *centre* of the sample *towards the edge* of the ring. It is important to note that although the ring can be clamped to the substrate like in [51, 95], here the ring simply lies on top of the silicon substrate and is held in place only by the capillary forces created by the addition of liquid. When the liquid reaches an area sufficiently close to the ring, the evaporation encounters the competition of capillary forces, due to the presence of the Telfon ring, which traps the liquid. Consequently, the evaporation is considerably slowed down in the area of the sample close to the contact line between the ring and the substrate, hence giving more time for the particles to organise.

One interesting observation when using meniscus-driven deposition is that the addition of surfactant (like in the previous case of drop deposition [74]) does not affect the evaporation duration significantly [92]. The rate of evaporation in this configuration is mainly dictated by the capillary forces related to the presence of the Teflon ring, rather than the presence of excess surfactants. Noticeably, for a solution containing excess surfactant molecules, initial dewetting does not tend to occur as rapidly in the centre of the sample as for a solution free of surfactants. But this, surprisingly, does not modify strongly the overall evaporation time. The local evaporation rates (in the centre and at the edge of the sample) are modified, but the average rate on the sample is similar in both cases (see chapter 4). The role of excess surfactants in solution will be discussed at length later (section 4.4). However, the duration of the evaporation in the "meniscus technique" is much larger compared to that in

the spin-coating process (several minutes or more compared to a few seconds) and samples prepared using this method will hence be considered as being "close to equilibrium" systems.

3.3 Atomic force microscopy

3.3.1 Introduction

The main analysis technique employed in this study is tapping-mode atomic force microscopy (TM-AFM). In this experimental technique, a very sharp probe is swept across the surface of the sample in (X,Y,Z), retracing the topography of the surface that is being scanned in a non-destructive manner. AFM belongs to the wide family of scanning probe microscopes (SPM), such as the scanning tunnelling microscope (STM), first developed by Binnig and Rohrer [22] in 1982, which gives a point-by-point representation of the densities of states at the surface of a conducting sample by measuring the tunnelling current between an atomically-sharp tip and the surface. Scanning probe microscopes also include scanning capacitance (SCM), electrostatic force (EFM) or magnetic force (MFM) microscopes to name a few. All these techniques provide a range of specific information on the physical properties at the surface of the sample (topography, density of states, capacitance, electric and magnetic fields).

The main limiting factor in AFM resolution is linked to the sharpness of the tip - and not to the diffraction limit like in optical techniques. A typical value of the radius of curvature of an AFM tip is of the order of 10 to 20nm, down to 1nm for ultra-sharp tips. Figure 3.6 shows pictures of an AFM cantilever and

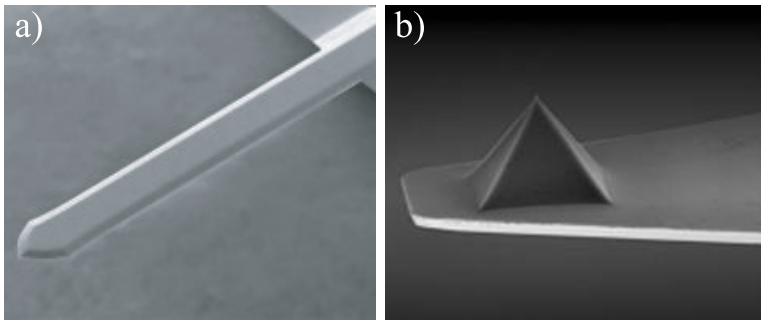

Figure 3.6: *Scanning electron microscope images of an AFM (a) cantilever and (b) tip on the end of the cantilever [47].*

the tip at its apex. In addition, it is important to note that, as opposed to STM, AFM can be carried out on insulators as well as metallic or semiconducting samples, since it measures intermolecular forces, which are always present, independently of the nature of the sample.

3.3.2 Vertical and lateral resolutions

The force between the surface and the tip is measured as a function of the tip deflection as it scans over the substrate. As a result, the sensitivity of this technique depends very strongly on the response of the tip and the sensitivity of the detection of this response. The design of the AFM cantilever must agree with the requirements of a maximum deflection in response to a given force and a minimization of the noise due to mechanical vibrations. In practice, this translates into a low value of the tip's spring constant - the lower limit being determined by the stability of the system - and a high resonant frequency. Laser beam deflection is the most widely used method of detection. The schematic of figure 3.7 shows its principle. The back of the tip is coated with a reflective layer of aluminium onto which a laser beam is focused and

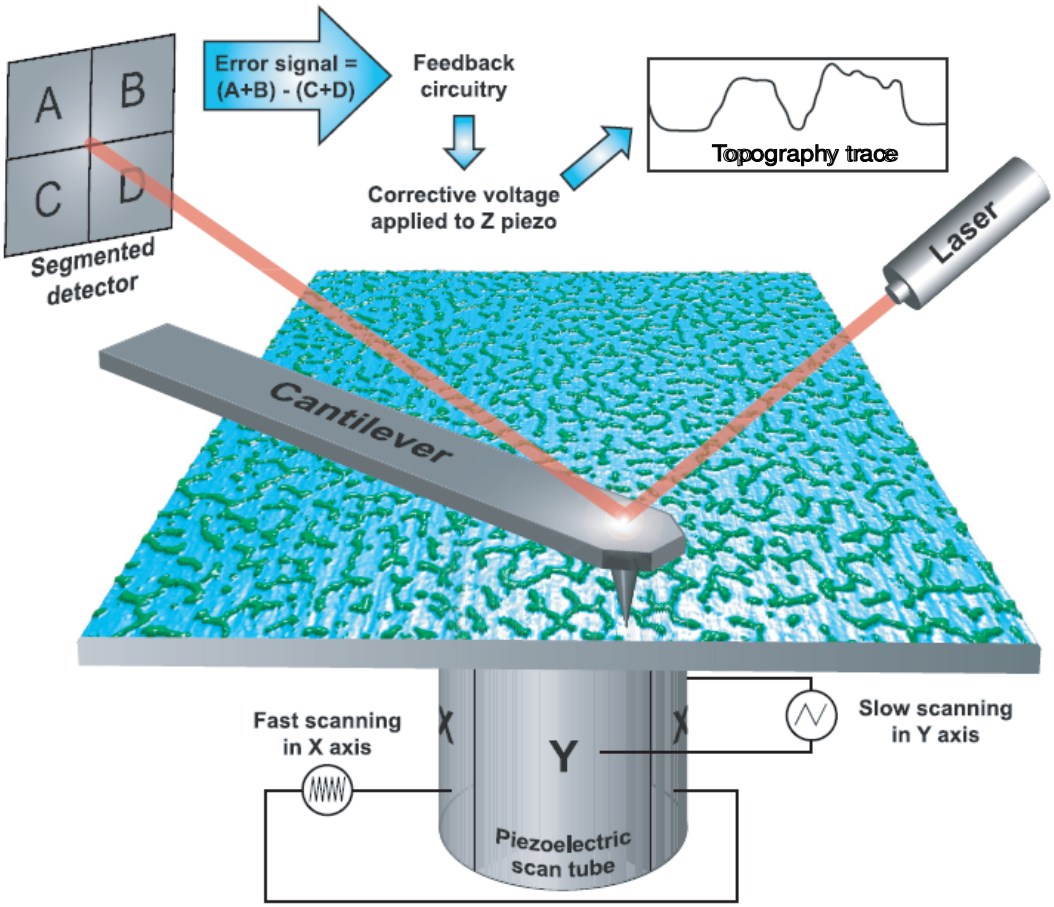

Figure 3.7: *Principle of the laser beam deflection detection system. Courtesy of C. P. Martin [50].*

reflected towards a photo-detector. Deflection of the cantilever modifies the position of the reflected beam onto the detector and alters the measured signal. Forces as small as $10^{-10} - 10^{-11}$N can be measured this way.

The typical lateral resolution of AFM is of the order of a few nanometres to a fraction of nm (it depends on the tip and its environment - the resolution will be much better in ultra high vacuum (UHV)). This is achieved using a complex combination of piezoelectric crystals which very accurately vary the position of the sample relatively to the tip. They are also used to change the

distance between tip and sample in response to changes in the deflection of the cantilever from its set point. This is called the feedback loop. The displacements associated with the response of the piezoelectric crystals are a direct measurement of the surface topography. Finally, an important consideration when it comes to the lateral resolution of AFMs is that the resulting image is always a convolution of the features on the surface and the shape of the tip. In most cases, the scale of the objects which we attempt to image is much smaller than the size of the tip itself (for example when one scans 2nm particles with a standard 20nm radius tip), meaning the image of single objects isolated on the surface will appear broadened. As a consequence, depending on the packing of several juxtaposed objects on the surface, it is possible that the convoluted profiles cannot be resolved individually (broadened profiles are superimposed), meaning the AFM image of the ensemble of objects will show a flat and featureless area (see Fig. 3.8). In extreme cases, this can give an indication on the degree of packing in a layer of particles (of which the size is known) since the detected signal will be an average of the height sensed by the tip (Fig. 3.8(c)).

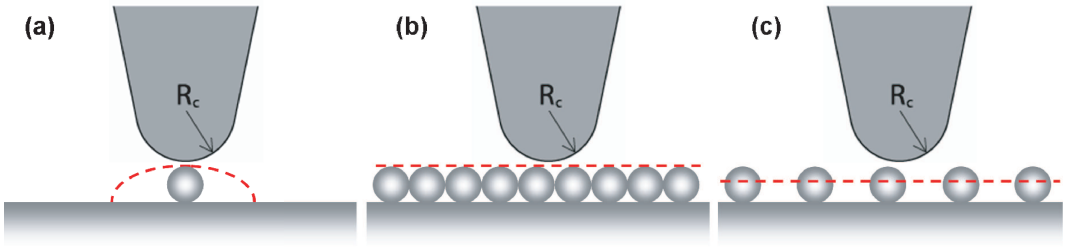

Figure 3.8: *AFM profiles of (a) an isolated object whose shape is convoluted with that of the tip (much broader profile), (b) a layer of close-packed particles (the average height is the real height of the particles), (c) a layer of loosely-packed particles (the average height is smaller than that of the particles).*

3.3.3 Tapping mode

AFM can be operated in two different imaging modes : contact and non-contact modes. In the first case, the atomically-sharp tip is in direct contact with the surface and the forces probed result from the short-range repulsive interactions between the tip and the surface. In non-contact mode, on the contrary, the tip scans over the surface from a distance, and the long-range (attractive) van der Waals interactions are the ones being measured. This is illustrated in figure 3.9. The main disadvantage of contact mode lies in the important lateral friction force applied by the tip on the surface and which can cause very important damage to "fragile" or "soft" structures, such as the nanoparticle assemblies of interest in this work. On the other hand, non-contact mode, although it avoids the risk of damage by the probe, requires that the tip remains sufficiently far from the surface, meaning the forces detected will have a reduced influence on the cantilever, affecting quite dramatically the amplitude of the measured signal and the resolution of images.

Tapping mode represents an alternative imaging technique, combining both the previous modes and a controlled oscillation of the cantilever. By oscillating the cantilever, one does not measure a *force* anymore, but the force *gradient* experienced by the cantilever. The oscillation is imposed to the cantilever at its resonant frequency. When a force gradient is detected by the tip, the frequency of oscillation is shifted. By detecting and adjusting the change in the oscillation frequency (via the feedback loop), the AFM can then detect very small variations (much smaller than the absolute forces measured in the two previous modes). Tapping mode is an hybrid mode of contact and non-contact AFM : the oscillating cantilever is placed closer to the surface than in non-

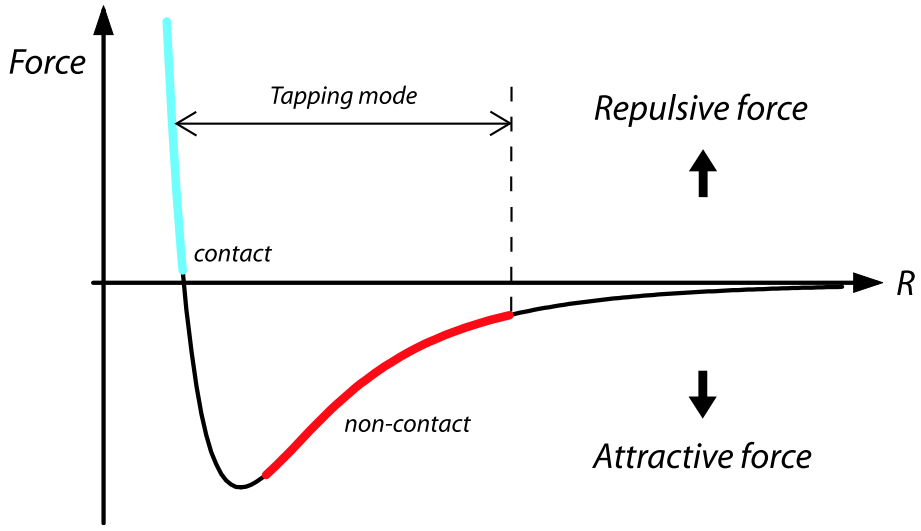

Figure 3.9: *Interaction potential for contact, non-contact and tapping AFM imaging modes.*

contact imaging mode. As a result, the tip actually comes into contact with the surface at every oscillation, from which originates a shift in the oscillation frequency and amplitude, corrected by the feedback loop. Thus, tapping mode offers the resolution of contact mode AFM (only limited by the radius of the tip), but due to the very brief period of effective contact between the tip and the surface, destructive lateral friction is removed, preserving the advantages of non-contact mode imaging.

3.3.4 Phase imaging

Finally, it is important for future developments to highlight that in addition to providing the topography of the surface, AFM can give us access to other information on the scanned sample. Phase imaging results from monitoring the difference in phase between the imposed oscillation signal and the effectively detected oscillation of the cantilever. This phase shift derives from the

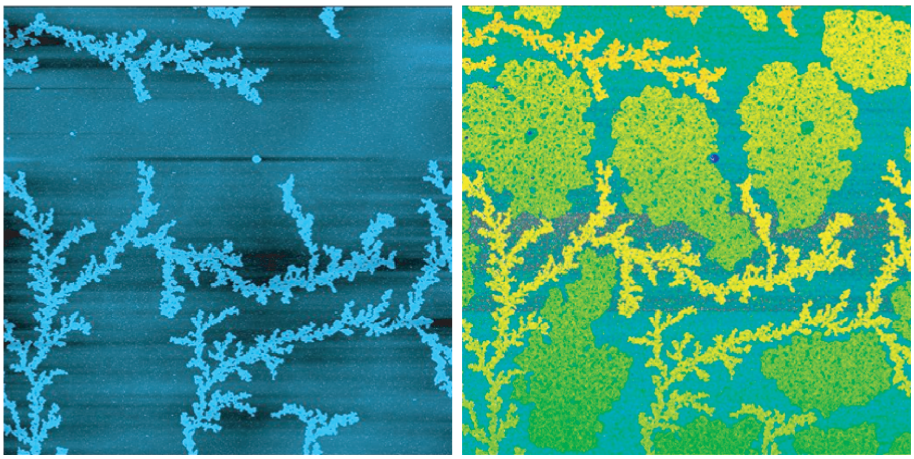

Figure 3.10: *AFM picture of a mixture of hydrophilic and hydrophobic nanoparticles spun onto a native-oxide terminated silicon substrate. The phase image (right) shows clearly some domains between the branching islands that are not visible in the height phase (left) and are of different nature than the islands or the substrate. Scan sizes are* $50\times50\mu m^2$.

dissipation of energy that occurs during the tapping of the tip on the surface; different materials will induce different energy dissipation, allowing their differentiation in an image, even on a topographically flat surface. Although it is not a quantitative mode of imaging, as is the height measurement (topography), when it comes to self-organisation on a flat sample for example, it can provide very useful information on the presence of regions with different properties at the surface.

Figure 3.10 illustrates the complementary roles of height and phase imaging. These images were obtained when spin-coating a mixture of a solution of hydrophobic particles in toluene (of size spreading from 5 to 8nm with *C9*-thiol ligands) and 15% in volume of a solution of hydrophilic particles in isopropanol (14nm in size with hydrophilic ligands). The height image (left) shows the topography of the surface where very long branching structures are visible. The phase image of the same area (right) shows exactly the same

structures but large domains are clearly visible between them that did not appear in the height trace. The phase shows the differences in properties (or material) over the surface. Thus, the domains are of different nature than that of the substrate but also than that the branches. We cannot, just by the comparison of these images, explain either what the different regions are made of, or what the mechanisms at play in the formation of the branches and the domains (which, as a matter of fact, do not exhibit any measurable height, which would imply that they are embedded in the surface) are. However, it is clear that the height image only would not have enabled to notice the presence of the "embedded" domains, hence the information provided by the phase image is essential in order to eventually understand the process that leads to the formation of such segregated assemblies. In addition, note that the differences observed can in some cases also help to identify a possible functionalisation of the tip by mobile molecules / particles on the surface.

3.4 Contrast-enhanced optical microscopy: Sarfus technology

In addition to AFM, another microscopic technique was used to characterise the top layers of nanoparticles on solid substrates, that requires the use of contrast-enhancing substrates to provide a nanometer scale vertical resolution in optical microscopy (usually limited to the range >200nm by the light diffraction limit). This new technology, baptised "Sarfus" by its designers at *Nanolane* [96], combines a standard optical microscope, with a polarized white source, with a specific type of mutli-layered substrates, called "surfs"

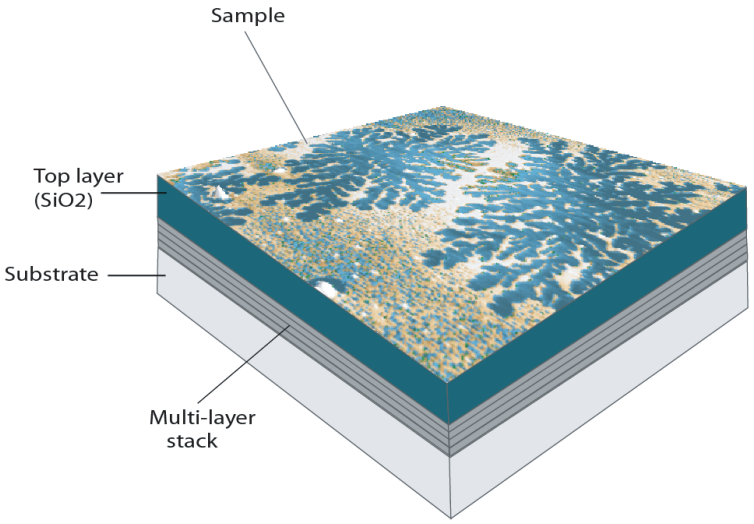

Figure 3.11: *Illustration of the structure of a Surf.*

(Fig. 3.11). It enables the real-time imaging of thin films of materials on a surface.

The reflection of the polarised light on a surf is perfectly known and controlled, and serves as a background calibration tool. Indeed, the polarisation of the light is unchanged by the reflection on a surf and can thus be systematically cut off from the analysed reflected signal, removing an important part of the background contribution, given by I_0 in the equation :

$$C = \frac{I - I_0}{I + I_0} \tag{3.1}$$

where C is the contrast and I represents the contribution of the sample top layer.

As a result, the presence of a small amount of matter on the surface will induce a very high value of the contrast. This technique can thus reveal the presence on the surface of nanometric objects or films of nanometric thick-

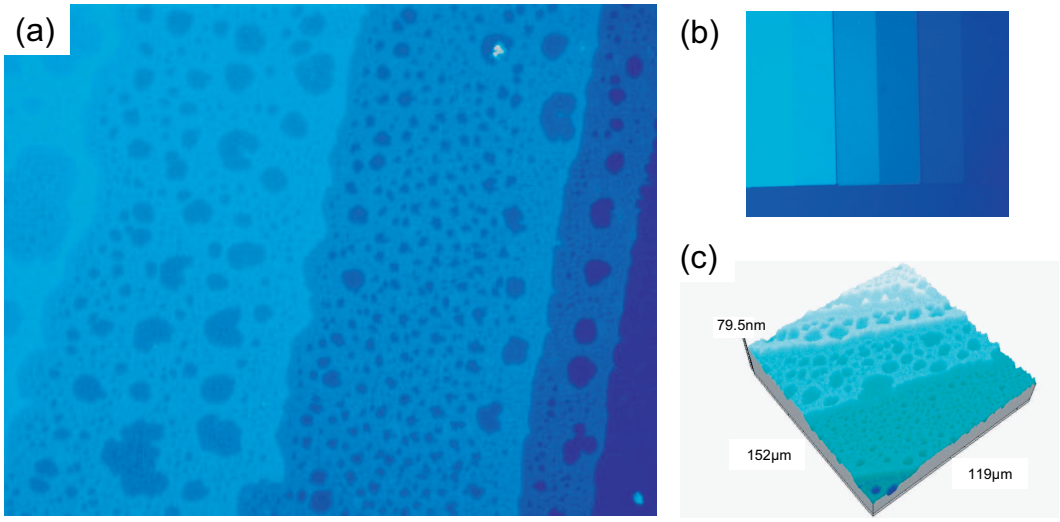

Figure 3.12: *(a) Example of an image taken with the Sarfus apparatus of 2nm decanethiol-passivated Au nanoparticles deposited from dichloromethane on a standard Surf (after O_3 plasma treatment) using the Teflon ring deposition technique. (b) A colour panel is used as a calibration scale for determining absolute optical thicknesses of the deposited layers. (c) A 3D reconstruction of the images is possible after calibration. (a) and (c) are 160µm×120µm in size, (b) is 80µm×60µm.*

nesses, without altering the lateral resolution of the optical microscope (usually ∼350-400nm). The Sarfus technology software then associates a colour panel with the thickness variations over the sample (Fig. 3.12), which is used for estimating the optical thicknesses of the observed objects. A combination of the Sarfus technology, which allows to observe areas up to square millimeters in size, with an AFM scan, which typically spans microscopic dimensions, constitutes a powerful tool to characterise the topography of one or several layers of particles deposited onto a solid substrate. Note that, conveniently, the top layer of standard surfs is a silicon oxide layer and can be treated the same way (cleaning procedures) as typical native-oxide-terminated silicon wafers. Moreover, the surface of surfs can be adapted to various applications, and materials can be altered to present different properties. Observation can also be carried

out in immersion for liquid samples [96]. In any case, the Sarfus technology offers the immense advantage to record real-time observations of the deposition and evaporation of a solution on a solid surface (see Chapter 5).

Chapter 4

Meniscus-Mediated Organisation of Colloidal Gold Nanoparticles

"Observons d'abord les amours d'un liquide et d'un solide. Et marions-les..."

Pierre-Gilles De Gennes.

The meniscus-driven evaporation technique introduced in the previous chapter was developed during the first year of this project. In this chapter, the experimental conditions associated with this deposition technique are exploited in order to influence pattern formation. The slow evaporation enables an enhanced degree of control of nanoparticle deposition and allows the drying process to be monitored by video camera. It provides valuable information on the mechanisms of drying and deposition, and highlights the influence of evaporation times and rates and of nanoparticle concentration on the selected patterns. This technique also led to the generation of close-packed monolayers

of nanoparticles and, as such, complements the usual drop deposition strategy, which remains difficult to implement [74, 76].

4.1 Introduction

Previous studies in our group exploited the correlation between the concentration of the solution and the formation of patterns on native-oxide terminated silicon substrates following deposition by spin-coating [47, 50, 81, 97]. A broad variety of patterns was observed, ranging from isolated droplets, dendritic structures and worm-like domains at low concentrations (see respectively Fig. 4.1(a), (b) and (c)), to cellular networks with various degrees of complexity and sometimes on several levels (Fig. 4.1(d) and (e)) and, occasionally, poorly developed hollow branched features (Fig. 4.1(f)) at high concentrations. Here, low concentrations range from 0.1 to 0.5mg/mL, whereas high concentrations lie within the 0.75 - 2mg/mL range typically.

In figure 4.1, all the scans show morphologies adopted by nanoparticles when trapped far from their equilibrium. The rate of evaporation undergone by the solution is roughly the same on most of the sample surface, which implies that the nanoparticle arrangement will be similar in all places on the substrate (with the exception of the edges, where the spin-coating process produces a slight hump of solution, hence locally a different concentration and film thickness during the evaporation process). Another important consideration is that as the concentration is increased further, a second layer of self-organised particles will form before the sub-layer is completed. This implies that, with these specific experimental conditions, a void-free, long-range ordered mono-

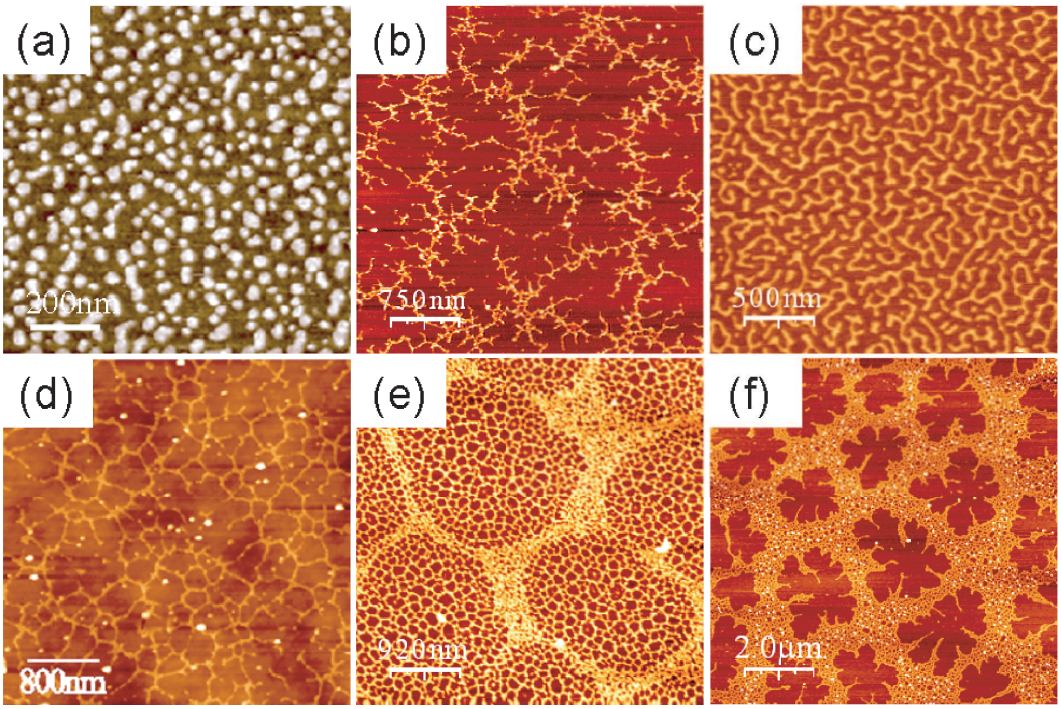

Figure 4.1: *AFM scans of C_8-thiol passivated nanoparticles on native silicon oxide. As the concentration increases, the morphologies adopted by the particles on the surface evolve from (a) a set of droplets at the lowest concentration (∼0.1mg/mL), to (b) dendritic structures, (c) worm-like domains and (d) cellular networks, sometimes on several length scales (e) for very high concentrations (∼2mg/mL), and occasionally to (f) poorly developed fractal-like structures. Scan sizes are given on the images. Courtesy of Matthew Blunt.*

layer of nanoparticles could not be obtained by spin-coating. In this chapter, we will see how the meniscus technique broadens the spectrum of tuneable experimental parameters and allows us to extend our field of investigation of pattern formation and complement past results on spin-coated samples.

General experimental conditions

The type of nanoparticles that we are working with here are 2nm octanethiol (C_8-thiol) or dodecane-thiol (C_{12}-thiol) passivated gold nanoparticles suspended in toluene. The nature of the passivating molecule is merely chosen

during the synthesis and does not involve any modification of the process, nor does it alter the stability of the particles significantly. The concentration of the solution can be varied by dilution and is given in mg/mL (dry nanoparticles can be weighted and redissolved at will in set amounts of solvent). The chosen solvent is toluene, but we will see in following chapters that other solvents are commonly used, such as hexane and dichloromethane (chapter 6). The substrates are typically $\sim$1cm$\times$1cm pieces of native-oxide terminated silicon (111) wafers. They are cleaned according to a standardised procedure that involves a 10 minute sonication in four different solvents, successively ethyl lactate, acetone, methanol and isopropanol. A supplementary cleaning step can be added, that takes place in a plasma reactor, where the solvent cleaned substrate is exposed to an O_2 plasma during several minutes, in order to remove all possible organic residues on the surface. The clean native oxide top-layer is 2 to 3nm thick and shows a roughness lower than 1nm. It exhibits an important degree of hydrophilicity, however toluene is found to wet the surface totally (the static contact angle was measured and estimated to be effectively zero within error). The wetting properties of the substrate can be altered by stripping the layer of oxide with an HF-based treatment, which creates an H-terminated surface, with a high degree of hydrophobicity. However, such samples will not be used for the purpose of the results presented in this chapter. Note that silicon substrates with a thick 80-200nm thermally grown layer of oxide, which provides an insulating layer between the particles and the semiconducting silicon underneath, can also be used. This is necessary in particular for carrying out electrical measurements on nanoparticle arrays (native oxide is too thin to prevent current leaks into the underlying silicon).

For now, we will suppose that the difference, in terms of interactions with the solvent and particles, between native oxide and thick oxide is not major and, in the case of a meniscus-driven evaporation, does not influence dramatically the nanoparticle self-organisation. However, we will have the opportunity to see later that although this assumption seems valid for these specific experimental conditions, it would be too strong in other cases (see Chapter 6).

4.2 Advantages of the ring deposition technique

As was explained in Section 3.2, the higher wettability of toluene on Teflon as compared to silicon oxide is exploited in the meniscus technique to deposit our toluene-based nanoparticle solution. In the experiment, dewetting occurs in the centre of the sample and the liquid front retreats towards the edge of the Teflon ring as the evaporation proceeds. Evaporation times up to 1 hour are achieved, although all visible solvent (that is, solvent that is not trapped directly under the ring by capillary forces) usually disappears within 5 to 20 minutes, depending on the experimental conditions. To make sure all solvent is removed before scanning the surface with an AFM, the samples are placed under vacuum for 12 hours following the 1 hour open air evaporation. The time scales of this experiment render the monitoring of the drying process possible and provide a high degree of control over the conditions of evaporation, improving the reproducibility of the experiments.

4.2.1 Reduction of the coffee-stain effect

One aspect of the standard drop deposition in open air (Section 3.2) is the difficult-to-avoid coffee stain effect. Unless one finds a way to prevent dewetting [74, 76], a retreating drying front will inevitably engender contact line pinning effects, due to the particles accumulating at the triple line and preventing further displacement of the front until they drop out of solution. This generally leaves macroscopic size aggregates on the surface. Figure 4.2 illustrates the difficulties associated with drop deposition. In the first case (Fig. 4.2 (a)), a simple drop of solution is deposited, that does not spread to the edge of the substrate. As it dries, the drop leaves a series of roughly circular macroscopic deposits, which impede AFM investigation (the aggregates are too large to be imaged). Whenever dewetting occurs, the same situation is observed. Figure 4.2(b) shows the case, as in Lin *et al.*'s and Bigioni *et al.*'s experiments [74,76], where an excess of thiol molecules is added to the solution. The evaporation process leaves a thick, viscous and non-volatile layer on the surface, whose nature we do not know precisely. This layer does not seem to be removable in a low vacuum environment. Once again, AFM investigation is impossible. Note that similar results, both for an excess-thiol-free solution and a solution containing excess thiol, are obtained for a drop that covers the entire surface of the substrate (i.e. initially pinned at the edges of the substrate).

A key advantage of the meniscus technique is that it prevents the "coffee-stain" effect, as shown in Fig. 4.2(c). Evaporation near the centre of the sample happens rapidly : initial dewetting is followed by a slow and steady movement of the front towards the edge of the ring. Contact line pinning effects exist [92], but importantly do not leave macroscopic aggregates on the surface.

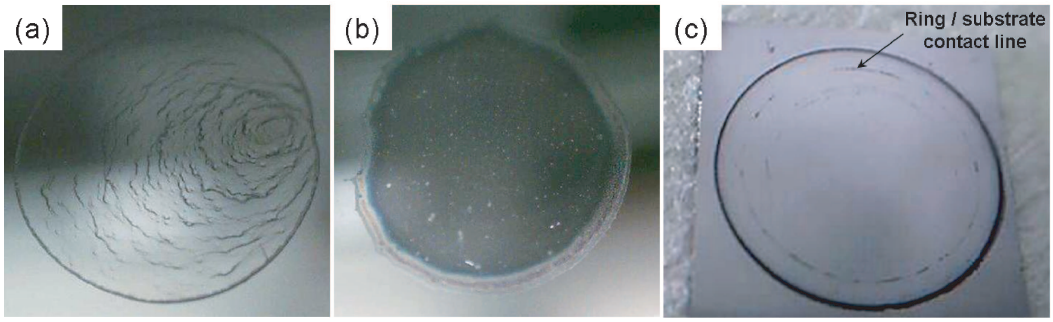

Figure 4.2: *Photographs of dry samples following deposition of a nanoparticle solution. (a) coffee-stain-like marks left by a 10μL drop of solution evaporated in open air on a 1×1cm^2 silicon sample ; (b) similar sample for a solution containing 0.1% excess C_8-thiol ; (c) a 1.5×1.5cm^2 silicon sample where 30μL of a solution containing excess thiol was deposited using an 8mm (ID) Telfon ring, then left to evaporate for 1 hour in open air before the sample was placed in vacuum for 12 hours. The location of the contact line between the ring and the substrate is indicated, and the thick aggregate at the edge of the sample marks the limit of the meniscus of liquid outside of the ring.*

Indeed, the pinning effect is counteracted by the capillary forces, which dictate the moving speed of the front. The duration of the pinning is thus shortened, meaning that fewer particles have the time to aggregate at the triple line and participate in the formation of a coffee-stain-like drying line. The only visible marks are present in the vicinity of the ring, where the solvent front retreats very slowly and the particles take up to one hour to self-organise. In particular, the contact line between the ring and the sample serves as a preferential site for aggregation. A thick drying line also forms naturally on the outside of the ring, where the meniscus only spreads over a short distance compared to the rest of the sample. Hence, this region - the thick line seen in Fig. 4.2(c) - presents a very high nanoparticle density, which explains the local aggregation.

4.2.2 Evaporation rate and concentration gradients

In addition to preventing the coffee stain effect, the meniscus technique enables a large range of parameters to be spanned *in a single experiment*. First, the evaporation is not homogeneous over the sample and the liquid front velocity is not constant. As a result, in the centre of the sample, the particles are deposited very rapidly, in far-from-equilibrium conditions, whereas the deposition occurs over very long time scales near the edge of the ring, corresponding to a much closer-to-equilibrium configuration (see Section 4.3.1).

Second, although the contact line pinning effects are small, they exist, and they influence the trajectory and regularity of the front's movement. This is called a "slip-stick" motion. The pinning effects can also create a non circular liquid front, with locally retarded evaporation due to pinning at one particular point (see Section 4.4.3). These irregularities in the dewetting / evaporation process induce the creation of specific morphologies and arrangements, as we will see in the next sections.

Third, there is an increase in the concentration of solute in the solution as the front moves towards the ring. Consequently, in addition to a gradient in evaporation speed, there exists a gradient in concentration over the surface of the substrate. The centre of the sample will be exposed to a low concentration solution, whereas at the edge there will be a much higher concentration and coverage (see section 4.3.2).

Finally, it seems that the ring deposition involves many *changing* experimental parameters, in the form of a concentration gradient and an evaporation speed gradient, and that these parameters vary in a manner that we cannot control specifically. However, we can control the global environment of the

sample and the main advantage of the meniscus approach is that evaporation is slow and easily monitored. As a result, for identical concentrations, substrates and quantities of solution, it is possible to obtain almost identical evaporation times (within tens of seconds) and local evaporation rates (considering that the pinning events are small, random and observed on every sample) for many samples. On the other hand, it is also possible to increase or decrease this global evaporation time with a high degree of accuracy, and to induce a larger number of instabilities in the front trajectory. In the following sections, the details of these changes will be given as appropriate while experimental results are presented. This gives an insight into the wide field of investigation that the use of the meniscus technique opens up.

4.3 Pattern selection and close-packed monolayers

This section aims to establish correlations between experimental data obtained using the meniscus technique and the experimental conditions and parameters. It specifically describes the set-up and sequence of events for each experiment, and the associated effects on the self-organisation of the nanoparticles, which is our main concern. Discussion of the evaporation process itself will be the subject of the following section (4.4).

4.3.1 A variety of patterns

As expected, colloidal gold nanoparticles deposited via the meniscus technique form a broad variety of patterns. Figure 4.3 shows the morphologies obtained on a typical sample prepared with C_{12}-thiol passivated particles deposited from toluene. In the specific case presented here, the solution contained an excess of 0.1% of C_{12}-thiol by volume, but Fig. 4.3(b) to (g) are also commonly observed in samples free of excess thiol. The case of Fig. 4.3(h) will be discussed separately.

A range of patterns, reminiscent of those seen for various samples prepared by spin-coating are observed coexisting on a single substrate. In the centre of the sample, isolated-droplet-type morphologies are observed, that are qualitatively very suggestive of patterns formed in the spinodal or "homogeneous nucleation" [1] regime (Fig. 4.3(b)). In this region, the evaporation is very fast and the concentration of the solution is low (the particles are well distributed within the volume of the drop), reminiscent of far-from-equilibrium spin-coated samples with low nanoparticle concentrations (Fig. 4.1(a)-(c)). As the evaporation time and the concentration increase, cellular networks start to form, such as those in figures 4.3(c) and (d), the latter exhibiting networks on several length scales. As one moves towards the edge of the sample, the sub-monolayer becomes more and more dense and close-packed. Holes in the shape of branched structures open up in the nanoparticle film, such as those in figures 4.3(e) and (f), up to the point, near the contact line between the ring and the substrate, where monolayers with few or no holes at all finally form (the evaporation takes anything up to 1 hour in these regions, Fig. 4.3(g) and (h)).

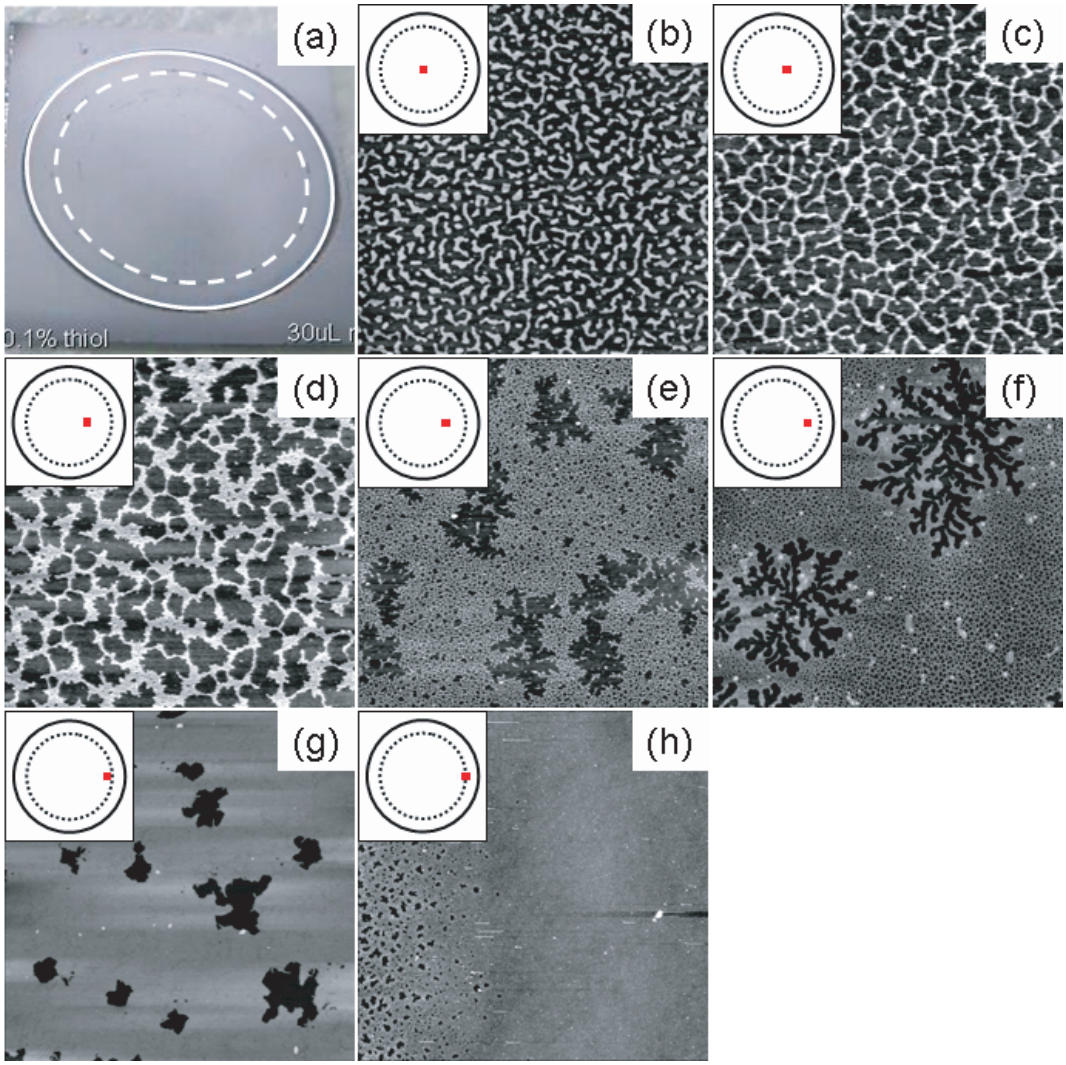

Figure 4.3: *(a) Photograph of the native oxide-terminated Si(111) sample following ring deposition of colloidal nanoparticles. The contact line between the ring and the substrate is represented by the dashed line, the thick line shows the outer edge of the meniscus of liquid. (b)-(h) Tapping mode AFM images of various C_{12}-thiol passivated gold nanoparticle arrangements on the substrate. The solution contained 0.1% excess C_{12}-thiol by volume. The inserts indicate the macroscopic region on the sample where the scan is taken - full and dashed lines correspond to those in (a). Scans (b)-(d) and (g) are 5μm$\times$5μm in size; (e), (f) and (h) are 20μm$\times$20μm.*

During this project, we have developed a particular interest in the final two types of patterns, namely branched features and void-free close-packed layers. A chapter is dedicated to the former (see Chapter 5). For now, let us just highlight two key points related to these fingering patterns that are relevant to meniscus-driven nanoparticle organisation : (i) the *isolated*, *well-developed* branching structures seen in Fig. 4.3(f) have not been observed in spin-coated samples (compare with Fig. 4.1(f), where the fingered holes were all adjacent, roughly identical in size and shape, and fingers were hardly developed at all); (ii) branched features form in a regime where there is an appreciable nanoparticle concentration *and* the time for solvent evaporation is relatively long. Aspects of finger formation and growth and the associated evaporation processes will be discussed at length later, but let us for now focus on the no-less fascinating void-free monolayers.

4.3.2 Close-packed monolayers of nanoparticles

As was discussed in Chapter 2, close-packed monolayers have been the centre of interest of numerous groups for well over a decade. However, producing long-ranged ordered assemblies of nanoparticles from solution is arduous. The conditions required are not all clearly identified, however, it is agreed that such organisation will preferably take place in a "slow" (compared to spin-coated samples, i.e. several minutes) evaporation process, for a specific concentration of the solution. The meniscus technique gives us the possibility to fulfil these basic requirements and, as expected, for a chosen concentration, enables the formation of such assemblies (Fig. 4.3(h)).

It is difficult to determine the precise concentration that is required to form

close-packed layers in our case. Indeed, the initial concentration was accurately chosen to be 0.5mg/mL and the quantity of solution deposited was adjusted depending on the size of the Teflon ring (e.g. a 30μL drop within an 8mm inner diameter ring), but as was said earlier, the actual concentration of the solution "seen" by the substrate in different regions varies as the front retreats and is extremely problematic to measure.

Despite these experimental difficulties, close-packed monolayers spreading over an area 5 to 25μm wide and as long as the perimeter of the ring were obtained with a very good degree of reproducibility. The fixed parameters of this experiment are as follows : the substrate is a 1.5cm$\times$1.5cm native oxide terminated silicon substrate, large enough to contain an 8mm diameter Telfon ring and the meniscus of liquid at the border of the ring; 30μL of a 2nm C_{12}-thiol passivated gold nanoparticle toluene-based solution, to which 0.1% excess C_{12}-thiol by volume has been added, were deposited within the ring using a micropipette. The solvent was left to evaporate in open air for 1 hour and then the sample was placed under vacuum for 12 hours. Tapping mode AFM investigation revealed that, under such conditions, close-packed monolayers could *reproducibly* be observed within the few tens of microns located just before the contact line between the ring and the sample, as illustrated in Fig. 4.4.

We found that the amount of excess thiol added to the solution did not contribute to broadening the width of the circular close-packed monolayer, nor did an increase of the initial concentration of nanoparticles (a second layer forms). However, for amounts of thiol above a few 0.1% by volume, the pattern formation process was greatly disturbed and morphologies such as those

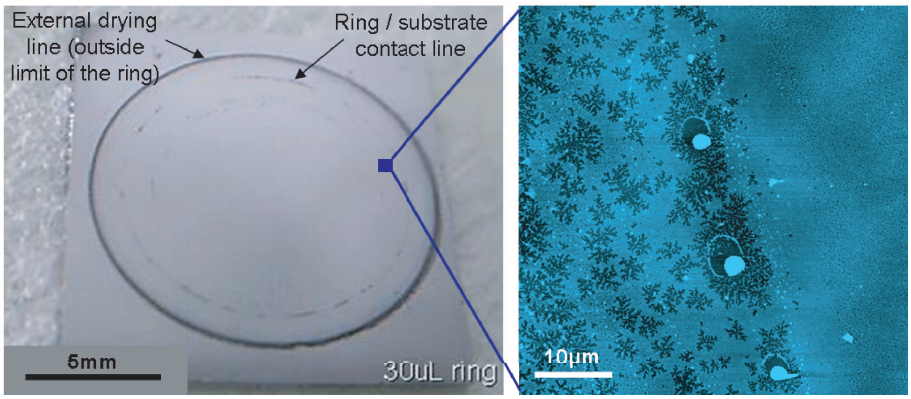

Figure 4.4: *(left) Photograph of the silicon sample following the ring deposition; (right) 50µm×50µm AFM scan of the region indicated by a dark square in the photograph, that shows the transition from a patterned sub-monolayer (on the left of the scan) to a void-free monolayer (on the right) close to the edge of the ring.*

illustrated in Fig. 4.3, and including close-packed monolayers, could not be as easily identified. Similar results could be observed when using different sizes of rings and samples, without having to modify the initial concentration, but merely the amount of solution. The fact that large-scale close-packed monolayers only form in the presence of excess thiol confirms observations by Lin *et al.* [74] and Bigioni *et al.* [76]. However, we have not observed a segregation and organisation of the particles at the solvent-air interface as suggested by Bigioni *et al.* [76], and we question the precise role of excess thiol molecules in the self-organising process. This will be discussed in Section 4.4.2 below. Note also that close-packed monolayers were obtained initially with C_{12}-thiol passivated nanoparticles (or, in short, "C_{12} nanoparticles"), but that C_8 nanoparticles could also be used (although the reproducibility of the experiment was not as high in the latter case).

Various morphologies on a *single* sample

The ability to obtain a variety of different arrangements of gold nanoparticles, including close-packed monolayers, on a single sample has significant potential with regard to elucidating the effects of network topology / morphology on electrical transport characteristics [48] (see also Section 2.3.1). An important first step, however, is to determine the extent to which the presence of electrodes affects solvent dewetting dynamics and nanoparticle self-organisation. Prior to solution deposition, we deposited 10μm wide, 20nm high Cr electrodes onto a 200nm thermal oxide terminated silicon substrate via optical lithography. A maximum of eight pairs of electrodes were radially positioned and evenly spaced with regard to the centre of the Teflon ring (Fig. 4.5(a)).

Figures 4.5(b)-(f) show examples of nanoparticle arrangements obtained between 10μm wide electrodes separated by a 10μm gap for a C_8 nanoparticle solution with an excess of 0.1% of C_8-thiol. As one moves towards the edge of the sample, the nanoparticle arrangements become denser, as in the previous case. The observed morphologies are similar to those obtained in the absence of electrodes and on native-oxide terminated silicon, and eventually void-free close-packed monolayers were formed in the desired area (Fig. 4.5(f)). In these images, it is clear that significant solvent dewetting does not occur close to the metallic contacts : there are no denuded regions in the vicinity of the Cr electrodes. This preliminary result is very encouraging for the study of electrical transport through nanoparticle arrays. The fact that all the different morphologies are on the same sample removes a large part of the uncertainties related to experimental errors from one sample to the other (cleaning process, concentration of the solution, quantity of solution, etc.).

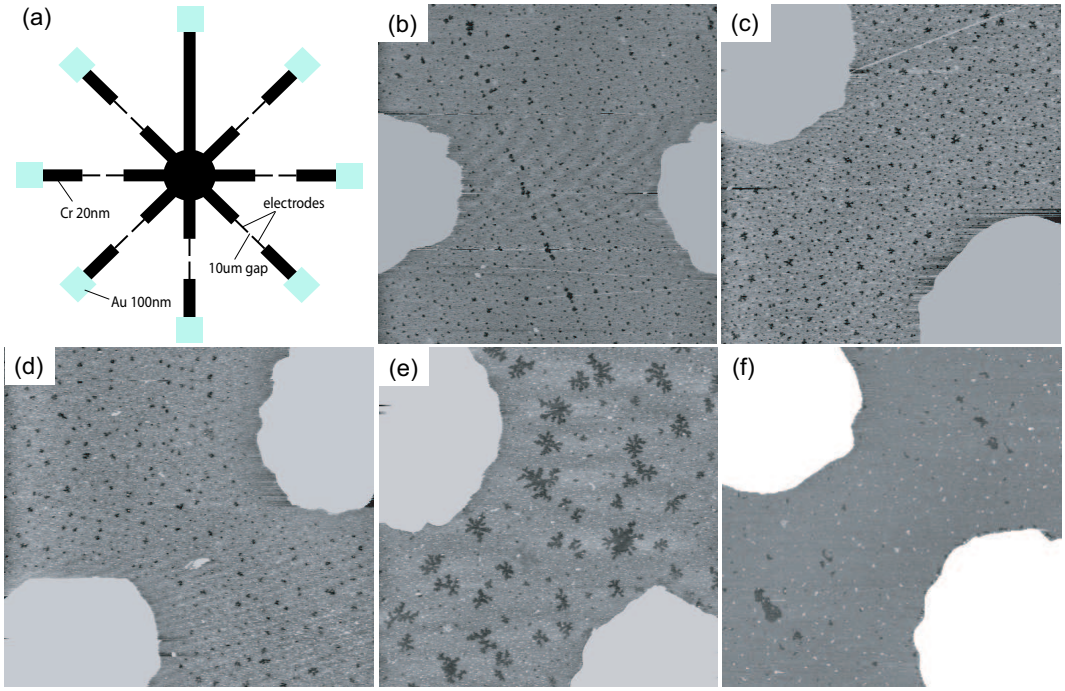

Figure 4.5: *(a) Schematic of the photomask used for the deposition of contacts via optical lithography, showing a possible configuration for the radial electrodes; (b)-(f) TM-AFM images of C_8-thiol passivated nanoparticle arrangements within the gaps separating pairs of electrodes (clear areas). The gap is located respectively at (b) 2.2mm, (c) 2.3mm, (d) 2.5mm, (e) 2.7mm, (f) 3.0mm from the centre of the sample. The solution contained 0.1% excess thiol by volume and was deposited following the usual ring-deposition procedure. All AFM scans are 20μm$\times$20μm.*

4.3.3 Drying "steps"

Finally, an intriguing phenomenon was observed at the boundary between regions exhibiting different types of pattern : in some cases, the transition between these areas is very abrupt, as illustrated in Fig .4.6. This effect is not always observed but whenever it occurs, it is particularly clear near the edge of the ring, where the widths of the regions decrease. Indeed, in section 4.2, we introduced the notion of "slip-stick" motion of the liquid front, due to contact line pinning effects. When particles drop out of solution at the

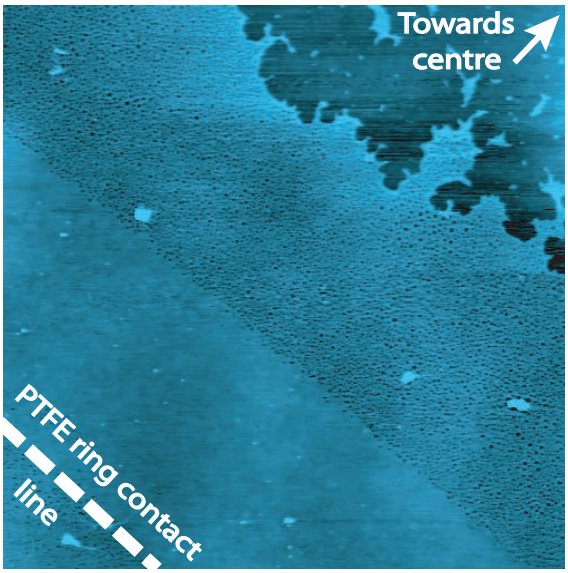

Figure 4.6: *AFM scan showing the clear transition between regions exhibiting different void concentrations : the boundary is very sharp and follows the shape of the Teflon ring. The approximate location of the contact point between the ring and the sample is represented by the thick dashed line. A solution of C_{12}-thiol passivated particles with 0.1% excess thiol was used. The size of the scan is 50μm$\times$50μm.*

contact line, the "released" front undergoes a sudden movement and retreats by one "step". Each step corresponds to a given evaporation time and a given concentration, that is, to a given type of nanoparticle arrangement. We believe that the clear boundary between a void-free and a void-ridden region in Fig. 4.6 corresponds to one of these steps. The reason why these transitions are much more visible at the edge of the sample is because the steps become smaller and smaller as one approaches the ring (this was indeed monitored by video camera), hence, in these regions, several transitions can sometimes be clearly seen on a single scan (in Fig. 4.6, one can successively see finger-like features, followed by a void-ridden layer, then by a close-packed monolayer). They are not systematically observed because, as it was stated earlier, the pinning of

the contact line does not always take place along the whole periphery of the meniscus, but can sometimes be localised in one or several isolated points.

This is just one consequence of the slip-stick motion of the liquid front, but we will see that the front's instabilities can induce other interesting phenomena and that in order to fully embrace the principle of pattern formation in our system, we need to dissect in more details the mechanisms associated with the evaporation and dewetting dynamics, the motion of the liquid front and the interactions and behaviour of the nanoparticles and excess thiol molecules.

4.4 Drying front instabilities

The previous section presented the main experimental results associated with our novel meniscus-driven evaporation technique. We shall now discuss some of the physical phenomena related to this new drying process. This section is separated from the experiment-based discussion above because some of the notions that will be dealt with here apply to the following chapters as well, wherever the meniscus technique is used.

4.4.1 The slip-stick motion and front velocity

We have so far focused on the assemblies at the microscopic level (by AFM investigation). We are also of course interested in what happens at the macroscopic level and how it influences the organisation of the particles at the smaller scale. More precisely, in the meniscus experiments, we have studied the motion of the liquid front and its behaviour depending on the nature of the solution deposited. The motion of the front, from initial dewetting in the centre of the

sample to the very slow evaporation near the Teflon ring, was monitored using a standard optical microscope in reflection. The working distance of the microscope did not allow us to observe the sample with a very large magnification, due to the presence of the 1 to 2mm thick ring on top of the substrate. However, the drying-related phenomena we are concerned with are observable at a sub-millimetre scale which was accessible with a low magnification objective.

Videos of the retreating front showed that for a standard C_8 or C_{12} nanoparticle solution in toluene, the motion of the front was regular, if not linear (see Supplementary Material of [92]). Dewetting in the centre of the sample usually occurs within the first few seconds of drying and the front then enters a stable regime where all visible solvent disappears rapidly, typically within 7 or 8 minutes, until the front reaches the edge of the ring. The only "defects" in the trajectory of the front arise from occasional pinning of the contact line, which creates the slip-stick motion described earlier. However, these effects are relatively minor. The blue curve in Fig. 4.7 represents the displacement of the contact line as a function of time for the first 2:30 minutes of evaporation following initial dewetting. It is interesting to note that the global evaporation time does not vary significantly with the size of the Teflon ring used, as long as the quantity of solution is adjusted. The blue curve shows the stable, almost linear motion of the front. Slip-stick steps would be represented by plateaux in this curve, but are not visible at this scale.

The important point is that, with the addition of thiol, one introduces very strong instabilities in the front motion. In particular, we observe oscillatory behaviour, that is to say, the motion of the contact line regularly *changes direction*. This motion is not adequately described by the term "slip-stick"

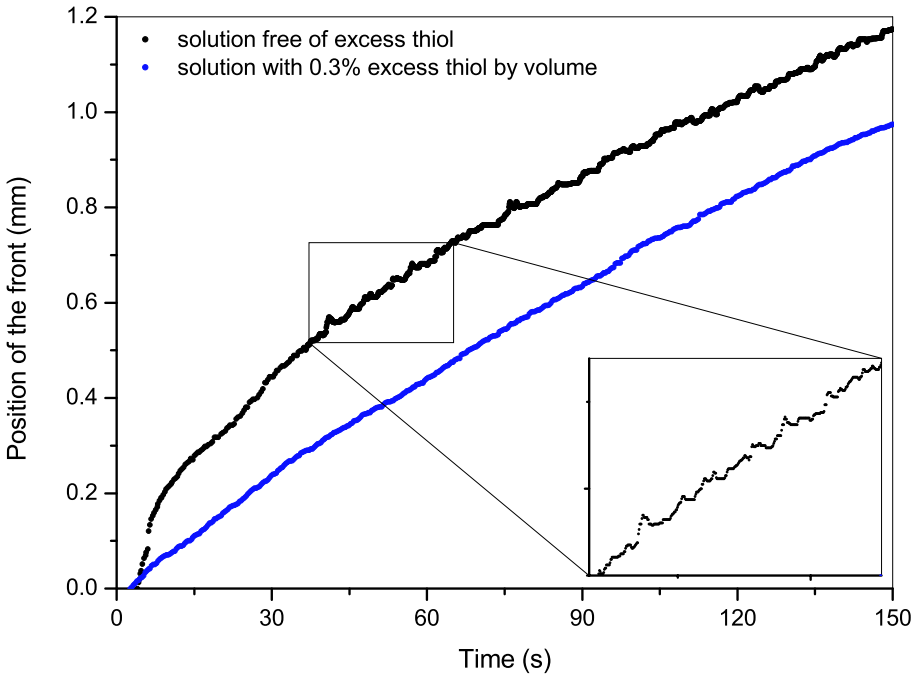

Figure 4.7: *Plot of the front position as a function of time during the first 2:30 minutes of drying following initial dewetting (in the centre of the Teflon ring). The graph shows the difference in the progression of the front velocity for a solution free of excess thiol (in blue) and a solution containing 0.3% excess thiol by volume (in black). The insert shows a close-up view of the oscillations observed in the presence of excess thiol.*

anymore (although this effect may still be present), it becomes rather erratic in space and time and the progression of the front and adsorption of the particles on the surface become very complex phenomena. This is illustrated by the black curve in Fig. 4.7 and the close-up view in the insert. The black curve presents irregularities that did not appear in the blue one, that is in the absence of excess thiol. The very fast progression of the front at the early stage of drying will be discussed in a moment.

Oscillatory behaviour of the front

First, one remarkable fact is that Fig. 4.7, which represents the front motion for solutions of nanoparticles with and without excess thiol, would look almost identical in the absence of nanoparticles suspended in the solvent (each curve would retain the same general shape). This means that the presence of excess thiol alone is sufficient to generate the strong contact line oscillations observed. As pointed out by Qu *et al.* [98], a change in the direction of contact line can only result from a modification of the Young's force at the triple line. The presence and, importantly, interactions of the free excess thiol molecules at (or close to) the contact line drives a change both in the value and the temporal evolution of the Young's force. This effect differs from a pure slip-stick motion driven by nanoparticle aggregation at the contact line, although in our case both slip-stick and oscillatory motion may occur during the dewetting process.

The influence of free surfactant molecules on contact line dynamics and evaporating liquid drops on solid substrates has been investigated in detail by a number of authors [98–105]. A variety of phenomena can couple to produce complex dynamics at the contact line and the associated precursor film. Truskett and Stebe [99] emphasise the importance of surfactant-mediated Bénard-Marangoni flow within the droplet. Others [98, 100] have focussed on the role of surfactant self-assembly. The closely-related phenomena of *super-spreading* and *autophobing* have also been studied in some depth [98, 101, 105], although there remain very many open questions. From the experiments described here, addition of thiol to a toluene-nanoparticle solution very strongly affects the contact line motion and thus the dynamics of nanoparticle assembly (see below section 4.4.2).

Front velocity

If we come back to the curves of Fig. 4.7, we notice that the front motion following initial dewetting is much faster in the case with excess thiol (black curve) than in the "normal" case. The drying process is actually very different in both cases. First, initial dewetting, in the case with no excess thiol, occurs very rapidly, within a few seconds. In the presence of excess thiol, however, this initial stage is much longer and can reach durations of 1 to 2 minutes. During this time, the distribution of the particles within the drop of solution changes (as observed by optical microscopy), and tends to become homogeneous (the "colour" of the solution becomes uniform). Once dewetting occurs, the front retreats at a rather fast rate. In the case with no excess thiol, the velocity of the front in this region is $\sim 7.5 \mu \mathrm{ms}^{-1}$, whereas it is closer to $12.5 \mu \mathrm{ms}^{-1}$ in the presence of excess thiol. This corresponds to the difference mentioned between the two curves in the early stage of evaporation.

Following initial dewetting, the motion of the front remains steady in the absence of excess thiol, with a progressive decrease of the velocity, down to $\sim 3.3 \mu \mathrm{ms}^{-1}$, as one approaches the edge of the ring. In the presence of excess thiol however, the velocity is greatly modified, and the font retreats more and more slowly, at less than $\sim 2.5 \mu \mathrm{ms}^{-1}$. Figure 4.7 only shows the first few minutes of drying *following dewetting*, which means that the plateau reached by the velocity in the latest stage of drying, on the black curve, is not shown.

In view of these considerations, it is expected that the two curves might intersect at some point in the drying process. Indeed, the *average* speed of the front calculated for both types of samples gave the identical value $5 \mu \mathrm{ms}^{-1}$. It is thus particularly interesting to note that past the initial dewetting stage, the

duration of solvent evaporation within the Teflon ring is not strongly affected by the addition of excess thiol.

4.4.2 The role of excess thiol

Following this discussion, it is now essential to ask ourselves what the precise role of excess thiol is. We have demonstrated that it does not influence the total evaporation time dramatically (although it does lengthen the initial dewetting stage). Truskett and Stebe [99] have made a similar observation for an insoluble surfactant (pentadecanoic acid) on an aqueous droplet - the presence of the surfactant did not affect the mean evaporation rate of the droplet. Moreover, under our experimental conditions, we have thus far not succeeded in directly observing the formation of nanoparticle islands at the solvent-air interface, seeded by excess thiol, as suggested by Bigioni *et al.* [76]. What is clear from the videos of the front motion that we were able to make, is that the addition of excess thiol plays a key role in the dynamics of dewetting both in the initial and final stages of drying.

What is perhaps somewhat surprising is that the thiol-induced modification of the contact line dynamics does not seem to affect the overall gradation of nanoparticle patterns from the centre to the edge of the ring (Fig. 4.3). However, the presence of excess thiol certainly is key for the formation of close-packed monolayers of particles. We will see in chapter 5 that it also contributes to determining some of the morphological characteristics of individual patterns. Following this discussion, we tentatively postulate that it is the thiol-induced modification of the wettability of the solvent that plays the key role in reducing the void density in nanoparticle assemblies. Recent

simulations by both Yosef and Rabani [82] and our group [86], based on the Rabani *et al.* Monte Carlo algorithm [1] (see details in section 5.5), show that the inclusion of disjoining pressure-induced dewetting (in addition of evaporative dewetting) is key in order to reproduce a range of nanoparticle patterns formed in the late stages of drying. The local evaporation rate is of course dependent on solvent wettability. Thus, while the overall evaporation time is very similar for solutions which are free of thiol and those with an added excess of thiol, *local* wettability and evaporation rates may be strongly influenced by the addition of thiol. We will have the opportunity to discuss the role of thiol again in both the following chapters, and will be able to partly complement our tentative explanation during the course of those discussions.

4.4.3 The fingering instability

To conclude this section and chapter, another instability that sometimes develops at the contact line is a macroscopic fingering instability (Fig. 4.8). It is often coupled with a strong and irregular contact line pinning effect, but not necessarily. The solvent can undergo transverse fluctuations, of the type of the Saffman-Taylor instability described in chapters 1 and 2. In theory, the presence of nanoparticles is not necessary for this instability to occur, although we have not specifically attempted to demonstrate this point. This fingering instability will be discussed in depth in chapter 5, where we will aim at establishing the correlation that may exist between this phenomenon at the macroscopic scale and the development of fingering structures at the microscopic scale. Note that the transverse instability grows and develops in intermediary regions on the sample (about half way between the centre and

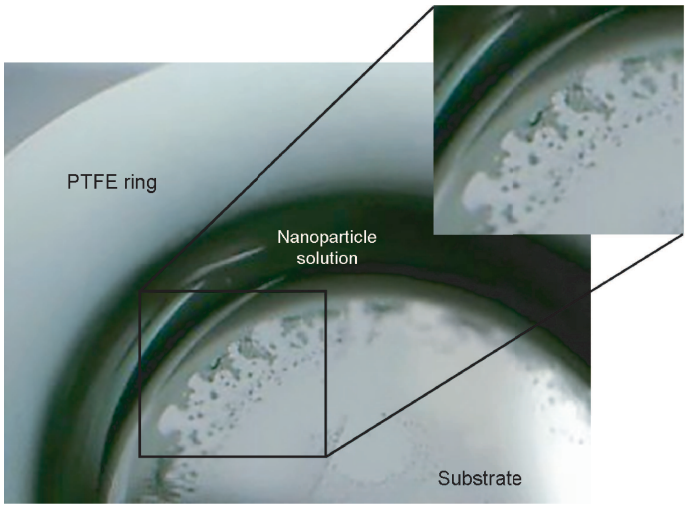

Figure 4.8: *Photograph of a $1.5\times1.5cm^2$ silicon sample onto which C_{12}-thiol passivated nanoparticle solution, with an excess of 0.1% of C_{12}-thiol by volume, has been deposited using an 8mm (ID) Teflon ring. The picture is taken during the drying process, as the front retreats from the centre of the ring towards its edge. Fingering instabilities similar to those described by Maillard et al. [69] and Xu et al. [85] are visible at the macroscopic scale.*

the edge of the ring), before being smoothed out as the front approaches the edge of the ring. Incidentally, it is also in these regions that fingered features are observed on the microscopic scale, such as those in the top right corner of Fig. 4.6 for example. In the absence of thiol, in our experiments, such instabilities have not been observed at the macroscopic scale, which once again raises the question of the contribution of excess thiol to the dewetting process. Such macroscopic instabilities are not unexpected - or uncommon - in nanofluids, and were previously observed in nanoparticle deposition experiments such as Maillard *et al.*'s [69] and Xu *et al.*'s [85]. We will dedicate one chapter (chapter 5) to the study of this particular type of instabilities and their manifestation both at the macroscopic and microscopic levels.

To conclude, by developing a meniscus deposition technique, we have pro-

duced an easily tunable tool to study the influence of deposition conditions on the formation of nanoparticle assemblies. Moreover, the meniscus method allows a systematic study of the evaporation / dewetting process and the motion of the receding liquid front. Despite its apparent complexity in terms of the correlation of the physical parameters of the system, this experimental set-up allows the production of steady conditions for the deposition of nanoparticles from solution and, as such, provides a high degree of reproducibility. The latter is of primary importance for the study of self-organisation processes and for the creation of long-range ordered nanoparticle monolayers, and addresses the requirement for a simple and reliable method of producing such assemblies. In chapter 5, in particular, this aspect will be exploited in order to study a particular type of pattern, namely fingering structures.

Chapter 5

Fingering Patterns in Assemblies of Thiol-Passivated Gold Nanoparticles

"L'énumération des paramètres, c'est l'agonie de l'espérance."

Daniel Pennac.

This chapter focuses on the formation of complex branching structures in assemblies of colloidal thiol-coated gold nanoparticles on a solid substrate following solvent evaporation. The primary aim is to determine the mechanisms involved based on both experimental observations and simulations. The branching features, sometimes referred to as "viscous fingers", were briefly introduced in Chapter 4. We were able to observe - in real time - the formation and growth of well-developed branched voids in particle sub-monolayers at the substrate interface [106]. The role of various parameters influencing the dewetting process are investigated including for instance the interparticle and

solvent-particle-substrate mutual interactions (by mean of the nanoparticle coating molecules and/or the presence of free surfactant molecules in solution) and the evaporation rates and times. We tentatively put forward theoretical considerations inspired from our data and earlier work [107–109] to account for the occurrence of such rarely seen patterns in nanoparticle assemblies. Finally, a simulation model adapted from that of Rabani *et al.* [1, 81, 82, 86] is presented, which gives an insight into the mechanisms of formation and growth of the fingering structures.

5.1 Viscous fingering, what is it?

Many systems in nature have the ability to form striking branching structures, which can sometimes exhibit fractal properties [6, 18, 110]. Typical examples include river beds and tree branches [6, 18, 111, 112], snowflakes and ice dendrites [54, 113], crystals resulting from the solidification of a melt [114], bacterial populations [6, 17], etc.

"Viscous fingering" describes the branching patterns formed at the interface between two fluids of different viscosities. This notion was introduced by Hill in 1952 [115], soon followed by publications by Saffman and Taylor (1958) [15] and Chouke *et al.* (1959) [116]. The physical phenomenon associated with the formation of these branching patterns is called the *Saffman-Taylor* instability, which takes place at the boundary separating two fluids. The instability refers to the fluctuation of the flat interface between two fluids of different viscosities, where the low-viscosity fluid pushes the high-viscosity one. As explained earlier in Chapter 1 (Section 1.1), Hele-Shaw cells (Fig. 5.1) constitute a fundamental

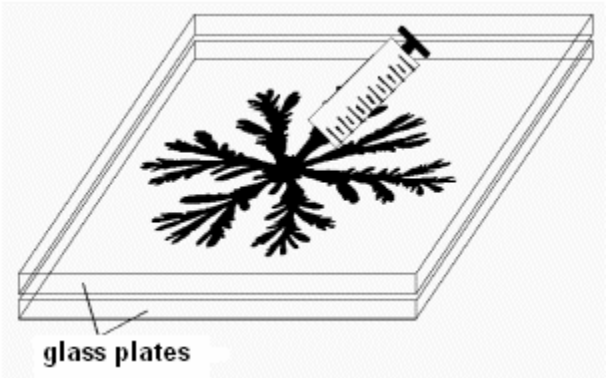

Figure 5.1: *Sketch of a Hele-Shaw cell illustrating the formation of viscous fingering by injection of a low viscosity fluid through a high viscosity fluid trapped within the cell.*

tool for the general study of fingering instabilities. They are commonly made of two parallel glass plates, separated by a very small gap into which the fluid of higher viscosity is placed (e.g. glycerin). A hole is punched into the top plate, through which the fluid of lower viscosity (e.g. air) is injected. As a result, the flow is effectively two-dimensional.

Shape of growing fingers

The manner by which the air/oil interface spreads into the oil depends on the pressure gradients created at the interface. In the presence of a bulge at the interface, the pressure gradients become locally more important, resulting in the front propagating faster in this region (Fig. 5.2). As a result, the gradient gets steeper as the finger grows and the growth process is self-amplifying and more and more rapid.

There have been many studies on finger growth and stability, with a particular focus on the determination of which size of finger will grow predominantly compared to the others [53, 117–119]. Surface tension plays a central role in

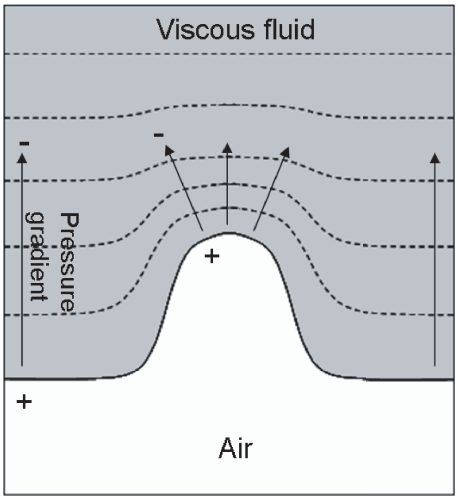

Figure 5.2: *Sketch of the fluid front between two fluids of different viscosities : due to the Saffman-Taylor instability, a bulge at the front grows into a finger. The phenomenon is enhanced as the tip advances and the growth becomes more and more rapid. The full and dashed lines represent isobars. Adapted from [6].*

defining the shape and characteristic dimensions of growing fingers, as will be explained below. Generally, there is always a preferred finger width, for which the pressure gradient at the finger tip will be larger than for any other finger widths. This finger hence develops faster and gets further ahead of the others, whereas smaller fingers, with a large pressure drop at the interface, tend to be smoothed out very quickly. Fingers form and develop with a certain degree of complexity : if the forcing velocity (the rate of injection of the low-viscosity fluid) is small, a single broad finger, spreading uniformly, will develop. Increasing the forcing will cause the finger to become narrower, up to the point where it undergoes a splitting and starts developing side-branches. What is generally observed is that the complexity of the fingering pattern increases with the forcing. This phenomenon is closely related to the presence of a non-zero surface tension at the interface.

The issue of fingering instabilities was also discussed by Maillard *et al.* [3]

in terms of Marangoni convection. Indeed, a solution of nanocrystals at high enough concentration [3] deposited onto a substrate can exhibit a fingering instability, which is attributed to a Marangoni effect and is presumably due to the nanocrystal concentration and the temperature gradients resulting from the evaporation process, from which originates a surface tension gradient at the interface responsible for the instability. Once again, the role of surface tension is presented as key.

The role of surface tension

To understand the origin of viscous fingering, one has to think once again in terms of competing forces, and in this case, the mechanism of finger growth resulting from the Saffman-Taylor instability is going to encounter the perturbing influence of the *surface tension*. Indeed, surface tension is always present at the interface of two immiscible fluids and determines its energetic cost. As a result, surface tension always tends to minimise the surface area. The broad fingers observed in viscous fingering, as opposed to the skeletal branches of a diffusion-limited aggregation model [57](this will be discussed in the next paragraph), are a compromise between the Saffman-Taylor instability, which promotes the formation of fingers, and the surface tension, which tends to smooth out the interface by pushing backwards the smallest bulges. As often in instability problems, this competition is usually accompanied with the emergence of a mode with a preferred length scale [118, 120]. Depending on the parameters of the problem, this gives rise to a multitude of branching patterns, from a circular bubble of low-viscosity fluid, to branching structures exhibiting a high degree of complexity.

The tendency of a system to form viscous fingering is characterized by its capillary number :

$$C_a = \frac{\mu}{\sigma} V \tag{5.1}$$

where μ is the viscosity of the high-viscosity fluid, V is the velocity of the interface and σ is the surface tension at the interface [53, 120]. What this definition tells us is that for small enough velocities, or large surface tension, the interface flattens out and the boundary spreads remaining straight. For intermediate values, a bump will be allowed to grow and locally form one stable finger, whose width is only determined by the balance of the different parameters. The regime that we are most interested in is that of high velocity or, equivalently, low surface tension. In this limit, the noise required to create an instability in a growing finger is very small. As a result, the front of the main finger itself will sooner or later undergo a Saffman-Taylor instability and the finger will split : a bulge will then grow on the interface into a secondary branch. Each new branch is temporarily stable, since it is thinner than the parent branch. However, due to the growth process, where the larger lobe develops faster than the others, a main finger will once again grow and undergo some splitting. The pattern hence repeats itself and develops according to this process. This accounts in particular for the fractal, or self-similar, character of these structures (a detailed description is given in [120]).

This rather intuitive process can be summarized by saying that : firstly, in the limit of large capillary numbers (small surface tension), many scales are allowed to develop and the dynamics of fingering formation becomes very

complex; secondly, the surface tension plays two roles in the formation of complex fingering patterns : it has to be low enough for the front of the tip to be unstable and it also causes the spreading and formation of *repeated branching*.

Diffusion limited aggregation (DLA)

There exist striking qualitative similarities between viscous fingering and a DLA pattern (introduced in Chapter 2, Fig. 2.2). However, the difference lies in the effect of surface tension. The DLA model, invented by Witten and Sander in the early eighties [56, 57], describes the aggregation of small particles, for example in a carrying medium or by sputtering. Incident particles diffuse in the vicinity of the originally formed aggregate until they find a site to fix themselves upon. This particular "hit and stick" phenomenon results in aggregates exhibiting a strong fractal character (with a fractal dimension estimated around 1.65 ± 0.05, see section 5.3.2).

There exists a clear difference between the DLA model patterns and viscous fingering. In the DLA model, no surface tension is introduced, meaning that the growth of a branch does not involve any energetic cost. In the case of viscous fingering, on the contrary, surface tension is responsible for the occurrence of a characteristic length scale, defined by the average width of the fingers. This difference in surface tension is also decisive when it comes to determining the influence of noise on the shape of fingering structures. Nittmann and Stanley [121] showed that they could reproduce the fat branches of viscous fingering in a DLA model by decreasing the randomizing effects, that is, by not allowing fingers to grow from a single particle impinged on the cluster,

but only on sites where several particles are already present. This introduces a criterion of "site selection". According to this selection, for a very low simulated level of noise, fat branches are generated (standard DLA representing the limit of high levels of noise). Conversely, by introducing randomizing contributions to a Hele-Shaw cell, one can produce very complex branching networks, very much like DLA structures. In summary, DLA corresponds to the zero-surface-tension case of the Saffman-Taylor instability problem. Hence at small values of the surface tension, the effect of noise becomes more and more critical (reiterating what was said in the previous paragraph) : finger "deformation" ranges from a slight asymmetry to splitting and eventually to highly branched dendritic structures as the surface tension becomes smaller and smaller.

The solidification analogy

The analogy between the formation of viscous fingering in Hele-Shaw cells and our colloidal gold nanoparticles is rather intuitive. Indeed, one can consider the nanoparticle solution as a very viscous fluid and when nucleation occurs, air is injected into it, forming branching structures. However, occasionally, a solidification analogy is also used [108], where a nanoparticle "solid" forms from a nanoparticle "melt". As a matter of fact, the process of solidification happens at the interface between the solid and its melt. The solid-liquid front sees an accumulation of solute and a high local temperature gradient, which leads to say that the liquid ahead of the front is "supercooled". This creates an instability, very much like in the case of viscous fingering, and the solid enters what is called the "dendritic phase", the resulting crystals exhibiting a strong branching character.

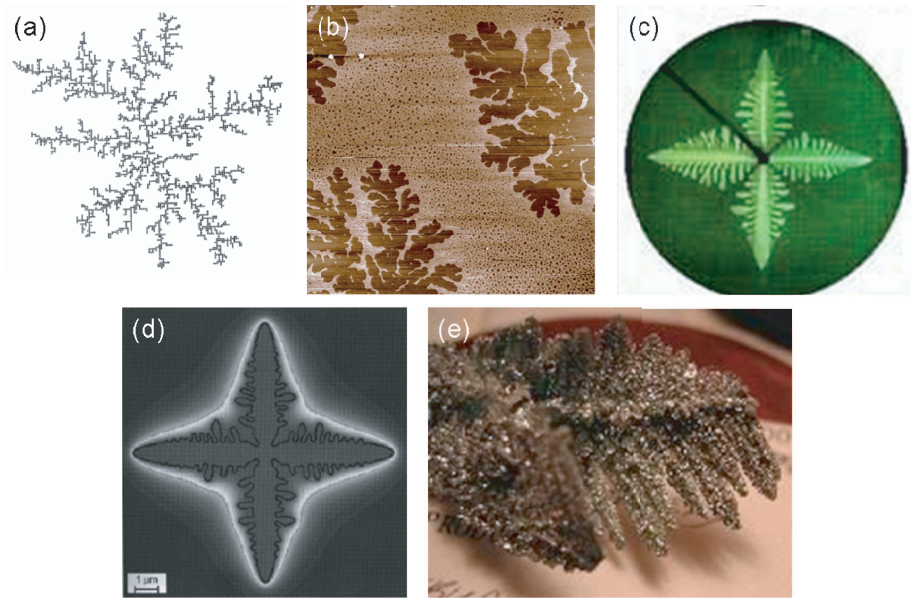

Figure 5.3: *(a) DLA model, from [56], (b) AFM image of gold nanoparticles deposited from solution onto a silicon substrate, (c) dendritic formation in a Hele-Shaw cell (from [122]), (d) model of the solidification of pure nickel and (e) dendritic crystal of zinc from partially solidified melt ((d) and (e) from [123]).*

Figure 5.3 illustrates the similarities between the various systems that we have described. The solidification and the Hele-Shaw cell analogies have sometimes served as a basis for theoretical interpretation of the viscous fingering formation and growth mechanisms in the past [108, 109]. However, the actual relevance of these analogies for dewetting films remains an open question.

5.2 A direct observation of viscous fingering formation

The system studied is a solution of 2nm thiol-passivated gold nanoparticles suspended either in toluene or in dichloromethane and deposited onto a native oxide-terminated silicon substrate. As we have seen in Chapter 4, following

evaporation via the meniscus technique, these particles form a broad variety of patterns on the surface, including viscous-fingering-like voids (refer to Chapter 4, Fig. 4.3(e) and (f)).

Using the new Sarfus technology described in section 3.4, it was possible to monitor the deposition and evaporation of the solution on a special silicon oxide terminated substrate ("surf"). The contrast enhancement provided by the surf allows one to monitor nanoparticle adsorption on the surface in real time. This provides considerable insights into the mechanisms of evaporation / dewetting of the solvent, pattern nucleation and growth within the nanoparticle-solvent film, and self-organisation of the particles.

5.2.1 Experimental observation

For the purpose of imaging the samples with the Sarfus apparatus, dichloromethane-based solutions were used. Dichloromethane is much more volatile than toluene, meaning that the evaporation time is reduced to less than a minute and the entire evaporation process can be acquired using a video camera (1 image per 0.125s). The formation of viscous fingering is not impeded by the use of dichloromethane rather than toluene as a solvent. The preparation of the substrate does not involve any particular cleaning procedure, since the surfs are covered by a thin protective film that is removed at the last moment. However, it is possible to modify the chemistry of the silicon oxide surface by placing the substrates for several minutes in an O_3 plasma, which tends to increase the hydrophilicity of the surface.

The microscope objectives provide magnification from $\times 5$ ($1200\mu m \times 1600\mu m$ frame) up to $\times 100$ ($60\mu m \times 80\mu m$ frame). Videos are usually acquired with

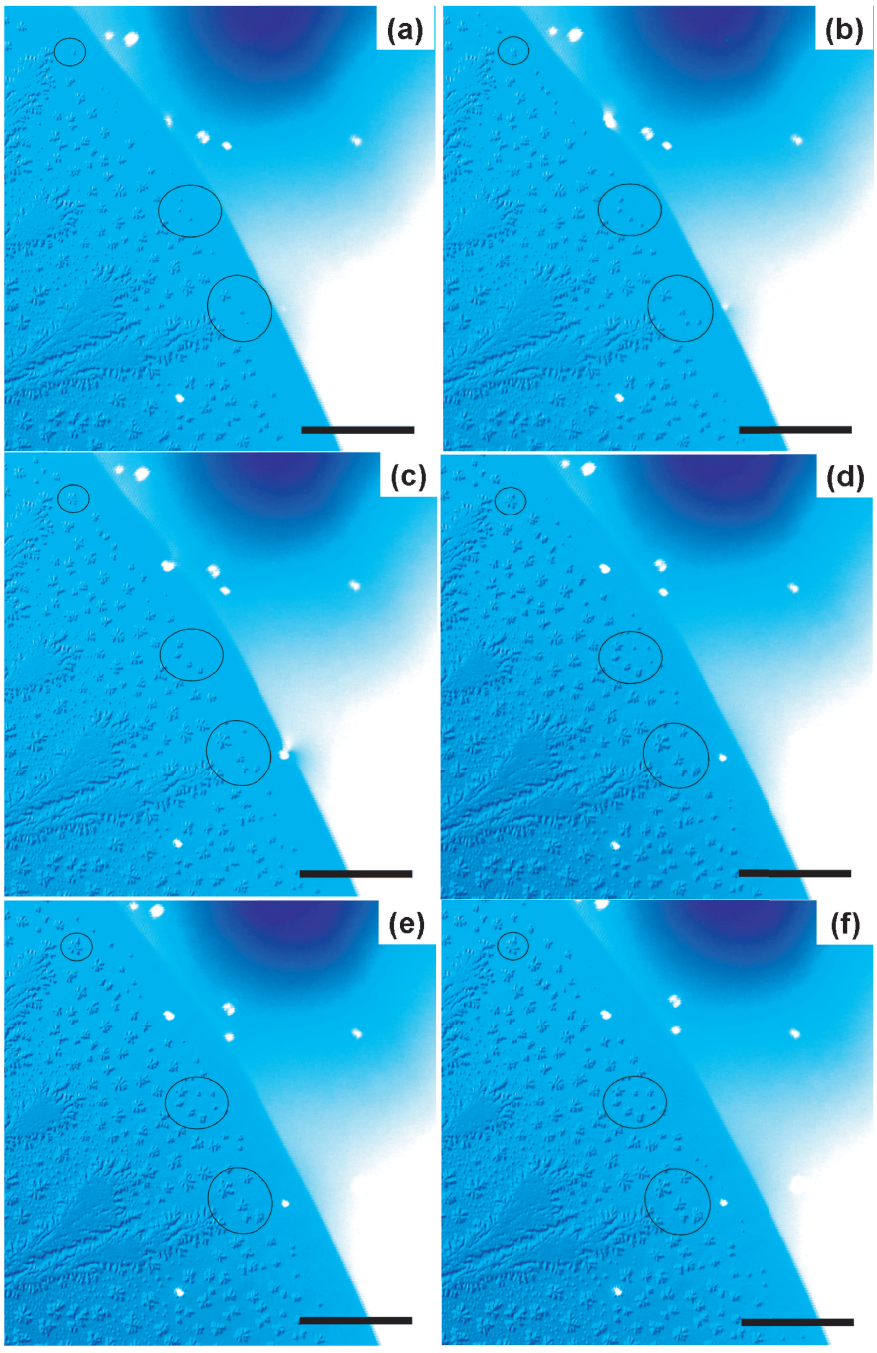

Figure 5.4: *2D images, obtained using the Sarfus optical microscope, of C_8 nanoparticle deposited from dichloromethane, via the meniscus technique, onto a standard surf. Images are acquired every 0.125 seconds. The clear area on the right is the evaporating liquid. The fingering patterns are empty (branched voids in a sub-monolayer of particles). A thin "precursor" film can be seen at the base of the meniscus, where the patterns develop (highlighted by random circled regions on the images). The scale bar represents 100μm.*

magnification $\times 10$ (600μm$\times 800\mu$m frame) or $\times 50$ (120μm$\times 160\mu$m frame). As explained in section 3.4, although the lateral resolution of the microscope is that of a standard optical microscope (350-400nm), the vertical resolution is improved dramatically by the contrast enhancing substrate (that strongly reduces the background contribution of the reflected light to the calculation of the contrast, see Eq. 3.1) and is better than 1nm. Note that it is not the topographical thickness of the layer that is measured, but rather its optical thickness (which is related to the former by a factor dependent on the material studied).

The region we are interested in is that near the receding front. One can see the finger-shaped voids forming at the base of the meniscus of liquid as the front retreats, as illustrated in Fig. 5.4, which is a series of captures from one of the videos. The thin precursor film that is left behind the front, at the base of the meniscus, is close to one nanoparticle thick. The topography of the sub-monolayer is more clearly visible in the 3D reconstructions of Fig. 5.5. Some nucleation sites have been chosen and circled on Fig. 5.4 to show their evolution as the front retreats (successive images are separated by 125ms). The most important information provided by the video is that these patterns clearly go on evolving *after the front has retreated*, within the thin "precursor" liquid film left on the surface behind the receding front. This confirms previous experimental and theoretical predictions [1, 81, 82, 92] concerning the assembly of colloidal particles at the solvent-substrate interface and implies that the mechanism involved must differ from that described by Bigioni *et al.* [76], who observed gold nanoparticle assembly at the solvent-air interface (see below). Moreover, as one moves towards the ring, where the global evaporation time

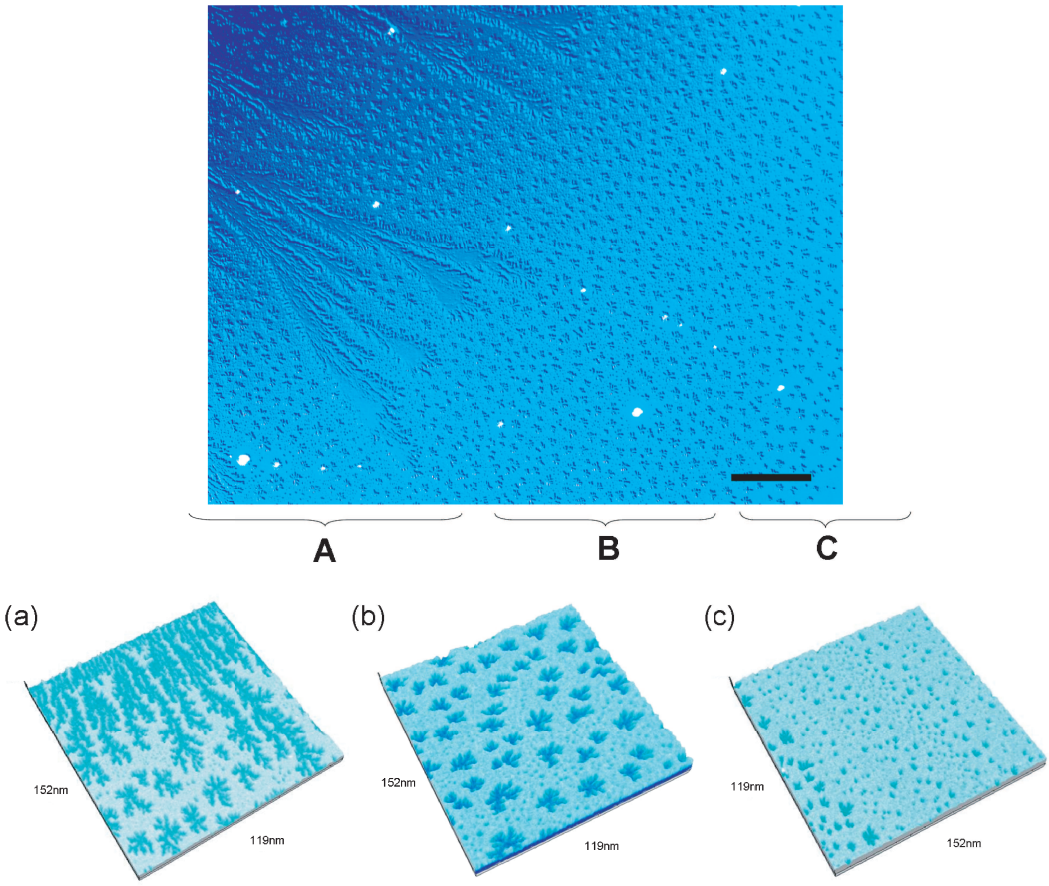

Figure 5.5: *(Top) Capture image from a video showing the first real-time observation of viscous fingering formation at the substrate-solvent interface (within a thin "precursor" film at the base of the meniscus). The scale bar corresponds to 100 μm. (a)-(c) 3D views corresponding roughly to regions A-C indicated on the top image, going from the centre towards the edge of the sample. 3D images are $120\times160\mu m^2$ in size.*

becomes longer, the layer of particles becomes denser and the branched voids within the layer tend to become smaller, although their degree of complexity remains high (Fig. 5.5(a), (b) and (c)). Note that because the evaporation time is shortened by the use of dichloromethane and no excess thiol molecules are added to the solution, no close-packed layers are formed in this experiment.

5.2.2 Assembly at the solvent-substrate interface

As discussed in previous chapters, there remain many questions regarding the conditions under which assembly of colloidal nanoparticles takes place. On one hand, Bigioni *et al.* [76], as we have seen in Chapter 4, have observed the formation of nanoparticle islands at the solvent-air interface, which coalesce in order to form a micrometre-scale defect-free monolayer on the surface of the drop, preceding complete evaporation and dewetting (Fig. 5.6). However, if we accept this description of nanoparticle self-organisation, it then becomes very difficult to imagine a mechanism that would lead to the formation of branching patterns such as that in Fig. 4.3(f), obtained via the meniscus deposition. Indeed, in our case, nanoparticles do not form *islands*, but *voids*. This type of pattern naturally leads us to imagine that void formation originated from a nucleation event in a thin liquid film.

On the other hand, Eran Rabani's group in Tel Aviv developed a model to describe systems similar to ours several years ago [1], which explicitly assumes assembly at the substrate-solvent interface. Indeed, their model originally described the motion and organisation of nanoparticles in a 2D film of solvent (see description in Section 5.5). This model, as we will see, reproduces many of the patterns that we have so far obtained experimentally. The mechanisms

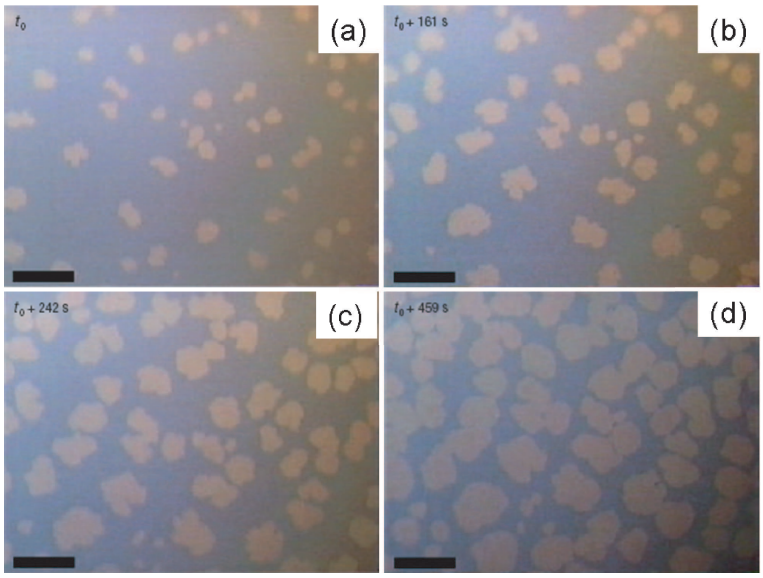

Figure 5.6: *Optical microscope images of dodecanethiol-passivated gold nanoparticle flat islands forming at the surface of an evaporating drop, at times (a) t_0, (b) t_0+161s, (c) t_0+242s and (d) t_0+459s. The scale bar represents 50μm. From [76].*

of organisation that it proposes support our assumption that assembly may occur at the substrate-solvent interface, rather than at the surface of the drop. The direct observation of the evolution of fingering patterns in a precursor thin film after the front has retreated strongly suggests that our system behaves according to Rabani *et al.*'s description [1,82] and that we are in a configuration that differs from that of Bigioni *et al.* [76]. In addition, the formation of islands on the surface of the liquid should have been visible while monitoring the evaporation by standard optical microscopy, which it was not.

Thus, in addition to providing the first real-time observation of nanoparticle adsorption on a surface, the Sarfus technology allows us to formulate a number of schemes concerning the self-organisation process of colloidal nanoparticles. This gives us a basis for future development of models which capture the

mechanisms at play in the formation of viscous-fingering-like structures in these assemblies, with the help of a simulation strategy that has already proven its reliability for systems prepared in different conditions (i.e. by spin-coating [47, 50, 81]). This will be discussed in detail in Section 5.5.

5.3 Controlling and tuning finger formation

We know from our first set of experimental data (Chapter 4) that viscous fingering only forms in given regions of the sample, that is within a certain range of experimental parameters. Surprisingly, the formation of viscous fingering is not commonly reported in assemblies of colloidal thiol-passivated gold nanoparticles, although our system is one of the most broadly studied in this field. That our system should form viscous fingering is not surprising in itself. We said earlier that analogies with a Hele-Shaw cell (a two-dimensional viscous fluid through which a less viscous fluid is displaced) or with the supercooled front of a solidifying melt could be easily established. However, it may be that the range of parameters that enables the formation of these patterns is very narrow and that only an adapted deposition technique (e.g. the meniscus technique) allows to gather all the necessary conditions for their occurrence. We have investigated this range of parameters and monitored their influence on fingering formation. Although fingering can be observed for different solvents - with toluene in Chapter 4 and with dichloromethane above for instance - we will focus here on a unique solvent (toluene) and on a unique type of substrate (native oxide terminated silicon) to facilitate the decoupling of the contributions of the various experimental parameters.

5.3.1 Experimental data: decoupled effects of experimental parameters

As explained in the introduction to this chapter, the formation of viscous fingering is closely related to surface tension and viscosity (see Eq. 5.1). The viscosity of the solution is dependent on the interparticle interaction within the solution. In other words, if particles "diffuse around each other" easily, the viscosity of the solution is low. The interparticle interaction can be varied for our particles by modifying the length of the thiol molecule carbon chain. Indeed, the core-core interaction is dictated by van der Waals forces and its strength depends on the interparticle distance. By lengthening the passivating molecule, one increases this distance hence decreasing the interaction and - in theory - the overall viscosity of the solution. However, longer chains also imply a stronger interdigitation of passivating molecules (up to C_{12}, see [124], for C_{14}, end gauche defects in the polymer chains reduce the interdigitation compared to C_{12}), which has the opposite effect on viscosity. The overall effect is bound to be a balance of these two contributions.

Another factor that influences both viscosity and surface tension is the addition of an excess of thiol to the solution. Indeed, the presence of free surfactants in solution tends to reduce the surface tension (the surfactants move towards the free interface to satisfy their amphiphilic property). But since thiol molecules are not very volatile and are bound to interact with the thiol molecules that form the coating of the particles, they tend to increase the viscosity of the solution as well (this is clearly visible by eye : an addition of 0.1% of thiol by volume is sufficient to modify the appearance of the solution

and make it look more viscous).

Our goal here is to determine what the optimal parameters for the occurrence and growth of viscous fingering are, and to identify their individual roles. Ultimately, we aim at deciphering the mechanisms at play in the formation of this specific type of pattern (see Sections 5.4 and 5.5).

Effect of the thiol molecule chain length

Pentane-thiols (C_5), octane-thiols (C_8), decane-thiols (C_{10}), dodecane-thiols (C_{12}) and tetradecane-thiols (C_{14}) can be used to passivate our gold nanoparticles, which are suspended in toluene. The concentration is adjusted in order to form as well-defined and well-developed branching features as possible, on the largest possible area of the substrate following ring deposition. The "ideal" experimental conditions typically yield fingering structures of the sort of those shown in Fig. 4.3(f) of Chapter 4, for C_{12}-particles in a solution containing 0.1% excess C_{12}-thiol. After drying (1 hour in open air, then 12 hours under vacuum), the sample morphologies are investigated thoroughly and systematically by tapping-mode AFM. All regions are scanned from the centre of the sample to the ring contact line at the edge (along one line, since the samples exhibit radial symmetry). Scans are then selected that qualitatively show the best defined branching structures found on the sample. For samples where fingering could not be observed, the most typical nanoparticle arrangement in the region corresponding to the usual fingering formation area is chosen. This area is roughly identical on all samples and is located about two thirds of the way towards the edge of the ring, and spreads over tens to hundreds of microns depending on the sample. The selected scans are shown in Fig. 5.7.

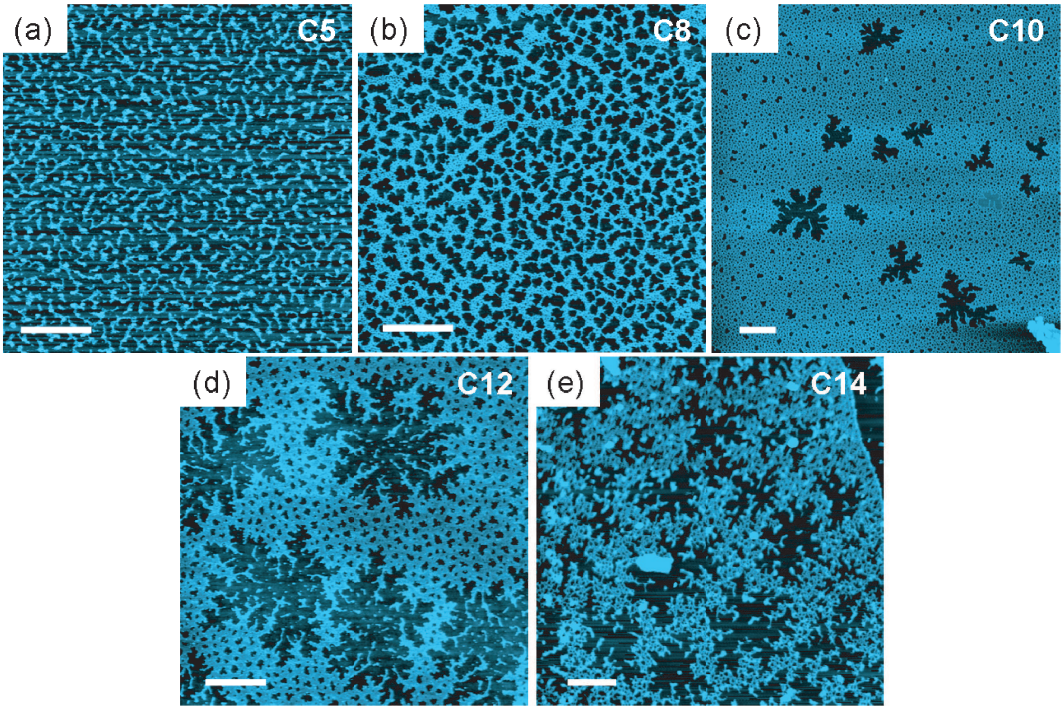

Figure 5.7: *AFM scans of (a) C_5-, (b) C_8-, (c) C_{10}-, (d) C_{12}- and (e) C_{14}-gold nanoparticles deposited via the ring-deposition technique onto a silicon substrate. The samples are prepared with a solution containing no excess of thiol. In every case, the best defined branching structures that were found on the samples are shown, or the most typical type of patterns present wherever viscous fingering does not occur (for (a) C_5 and (b) C_8 here). The scale bar represents 1μm. The average values of the ratios R = perimeter/area for (c)-(e) are respectively 0.24, 0.19 and 0.19.*

Noticeably, no fingering patterns were obtained for C_5 and C_8 nanoparticles (Fig. 5.7(a) and (b) respectively). Although we cannot exclude the possibility of fingering formation with these particular toluene-based solutions, it was not observed on any of our samples within the range of experimental parameters investigated (solution concentration - [0.1;4]mg/mL, quantity of solution used - [10;100]μL, and Teflon ring size - [5;8]mm inner diameter, corresponding to a broad range of evaporation times - [1;60]min). On the contrary, for C_{10}, C_{12} and C_{14} nanoparticle solutions, viscous fingering is obtained easily and repeatedly, as shown in Fig. 5.7(c), (d) and (e). Hence, viscous fingering occurs preferably for a longer chain length of the passivating molecule. This can be understood in terms of *interdigitation* of the thiol molecules of adjacent particles, which becomes more important as the length of the chain increases (with the exception of C_{14}), thus slowing down the diffusion of particles around each other and reducing their mobility. The dependence of the strength of the van der Waals interaction on the interparticle distance - which would contribute to decreasing the overall viscosity of the solution - does not seem to counteract the effect of interdigitation. However, we will see in the following section that a classification of the obtained fingering patterns reveals that such a competition of effects is taking place to a certain degree.

Effect of an excess of thiol molecules

An excess of thiol is now added to each of the solutions. The added molecule corresponds to that used for the passivation of the particles in each case. As explained before, the presence of excess thiol reduces the surface tension of the solution and increases its viscosity, both effects contributing to enhanc-

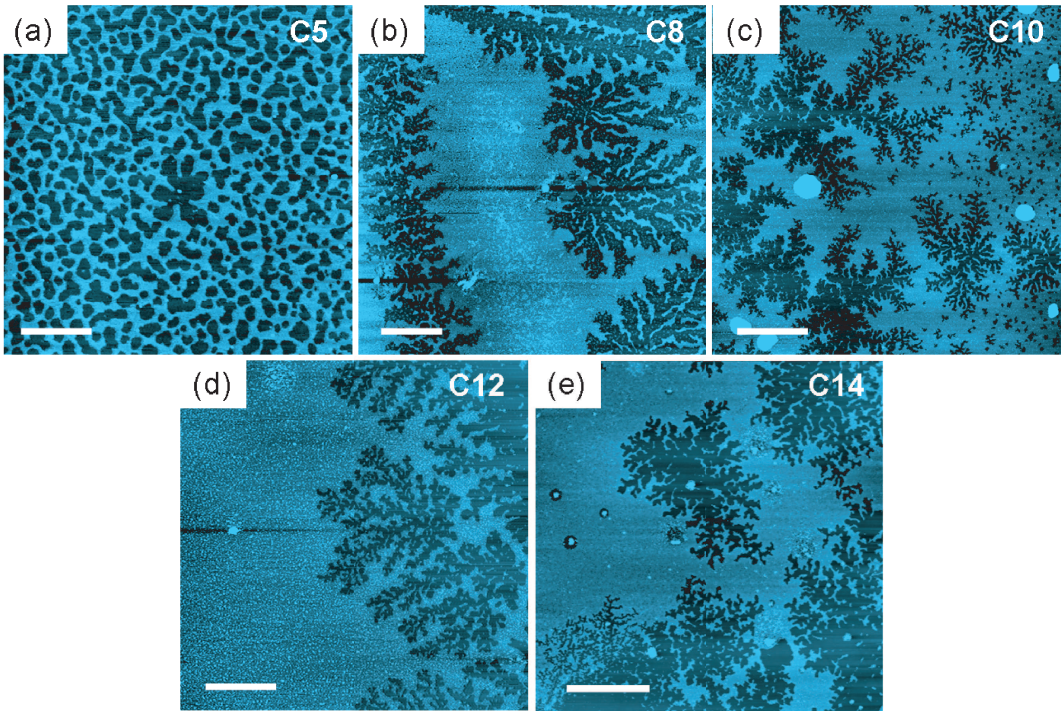

Figure 5.8: *AFM scans of (a) C_5-, (b) C_8-, (c) C_{10}-, (d) C_{12}- and (e) C_{14}-gold nanoparticles deposited via the ring-deposition technique onto a silicon substrate. The samples are prepared with a solution containing 0.1% excess thiol by volume. In every case, the best defined branching structures that were found on the samples are shown. The scale bar represents : (a) 1µm, (b)-(e) 10µm. The average values of the ratios $R = perimeter/area$ for (b)-(e) are respectively 0.26, 0.30, 0.26 and 0.25 (the value is not estimated for (a), which is an isolated event).*

ing the formation of viscous fingering, according to Eq. 5.1. Note that the addition of an excess of thiol to the solution does not influence significantly the evaporation time once dewetting has started in the centre of the meniscus (see Chapter 4) and for the purpose of our problem, we will assume that the velocity of the flow is near constant. The previous experiment is reproduced with the same concentration of the solution, identical substrates, ring dimensions and quantities of deposited solution. Scans are selected according to the same process as previously (patterns that are found to qualitatively exhibit the highest degree of complexity are selected). Results are shown in Fig. 5.8.

In this case, fingering patterns could be seen for each of the solutions, on at least one sample. For C_5 and C_8 nanoparticle solutions (Fig. 5.8(a) and (b)), branching patterns - often poorly defined - are sometimes observed, whereas no fingering patterns were obtained in the absence of excess thiol. For C_{10}, C_{12} and C_{14} nanoparticle solutions (Fig. 5.8(c), (d) and (e)), the formation of viscous fingering is considerably enhanced, as expected, and patterns spreading over tens of microns are observed (the scale is multiplied by 10 between Fig. 5.7(c), (d), (e) and Fig. 5.8(c), (d), (e)). Qualitatively, the presence of excess thiol enhances the formation of viscous fingering and promotes it in systems where they would not occur otherwise (for C_5 and especially C_8 nanoparticle solutions).

5.3.2 Data analysis: classifying fingering patterns

The previous section gave a succinct qualitative description of experimental results. It is clear that in order to compare the characteristics of fingering patterns from one sample to the other and quantify the respective effects of

the thiol molecule chain length and the excess of thiol, we need to establish a classification of these patterns.

Box counting algorithm and fractal dimension

Finding a suitable quantification method for radial viscous-fingering-like patterns is not trivial. Viscous fingering is typically associated with a fractal dimension. A standard box-counting algorithm [125] was initially used to estimate the fractal dimension D_f of isolated objects in our experimental images, such as those shown in Fig. 5.9. These binary images correspond to the fingering patterns of Fig. 5.8, obtained for solutions with an excess of thiol.

However, when comparing the results for the various patterns observed experimentally, one finds that they are all identical within error. Indeed, for instance for C_8, C_{10} and C_{12} nanoparticle solutions with excess thiol (Fig. 5.9(b), (c) and (d) respectively), the values obtained are respectively D_f=1.74±0.06, D_f=1.71±0.04 and D_f=1.77±0.04 (calculated using the *Image J* free software). For comparison, a standard DLA model is found to have a fractal dimension of D_f=1.68±0.05. Thus, while these values are close to the value

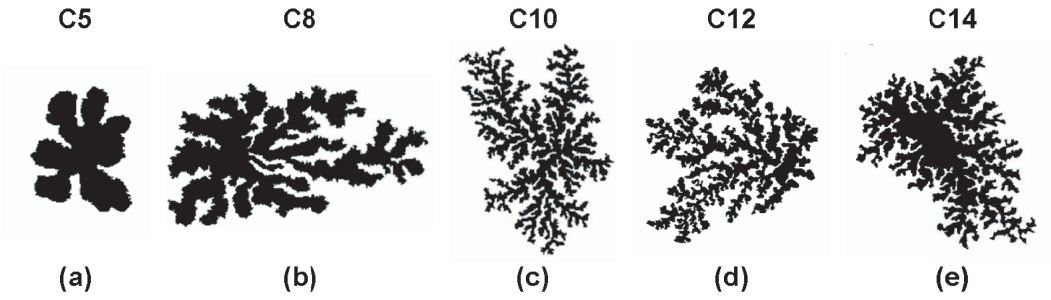

Figure 5.9: *Silhouettes (binarised images) of isolated branched patterns taken from the AFM images of Fig. 5.8 for C_5 to C_{14} nanoparticle arrangements. A box-counting algorithm can be performed on these binary images to obtain the estimated fractal dimension of the objects.*

for a DLA aggregate, they do not allow us to classify the patterns in terms of the degree of "fractal character". As a result, the fractal dimension seems an ill-suited quantification tool for describing the effects of experimental parameters on the formation and shape of our viscous-fingering-like patterns, and we need to find an alternative method.

Classification by geometric ratio

Ideally, the parameter that would allow us to describe fingering patterns quantitatively is the average finger width [53, 119]. However, defining "fingers" in our AFM images is problematic to say the least. Instead, a simpler approach to classifying our patterns is to determine a geometric ratio that will characterise their physical shape, such as :

$$R = \frac{perimeter}{area} \tag{5.2}$$

This parameter relates to the aspect ratio of the fingers and the degree of complexity of the overall structure. The higher R is, the more developed the fingering structures are. R is calculated on binary images such as those shown in Fig. 5.9. We prepared several samples with each of the 10 solutions (5 solutions without excess thiol, 5 with excess thiol) and scanned their surface as thoroughly as possible with an AFM. R was estimated on the various AFM images for the qualitatively best defined and most developed fingering structures - according to the same principle that was used for selecting the images of Fig. 5.7 and 5.8. An average value and the standard deviation were calculated (extreme values were excluded from averaging each time). Results

are shown in the tables below (Fig. 5.10).

Solution	C_5	C_8	C_{10}	C_{12}	C_{14}
R	-	-	0.24 $\pm$0.02	0.19 $\pm$0.02	0.19 $\pm$0.02

Solution	C_5 + 0.1%thiol	C_8 + 0.1%thiol	C_{10} + 0.1%thiol	C_{12} + 0.1%thiol	C_{14} + 0.1%thiol
R	-	0.26 $\pm$0.03	0.30 $\pm$0.03	0.26 $\pm$0.02	0.25 $\pm$0.02

Figure 5.10: *Values of the ratio R = perimeter / area for fingering patterns formed by C_8 to C_{14} nanoparticles from solutions without and with excess thiol (0.1% in volume). On average, these values relate to the type of patterns shown in figures 5.7 and 5.8. No value of R is estimated for C_5 nanoparticles in the second table due to the lack of statistics (Fig. 5.8(a) is an isolated event).*

Note that for some solutions, e.g. for a C_8 solution with excess thiol, the statistics over the calculation of R is poor, since few samples were found to exhibit viscous fingering. In the case of a C_5 solution, only one such feature was found (Fig. 5.8(a)), which was not considered sufficient to give a consistent estimation of the value of R (the dispersion is sometimes rather important for other averaged values). In the absence of excess thiol, no value could be estimated for C_5 and C_8 since no viscous fingering was observed. These results are summarised in Fig. 5.11.

Noticeably, and despite the presence of important error bars (shown on the graph, Fig. 5.11), the ratio R follows interesting and slightly unexpected variations. All the values of R are higher in the case with thiol as compared to equivalent samples in the one without thiol. This implies that *the presence of an excess of thiol enhances the fingering phenomenon*, as prompted by a qualitative analysis. However, the effect of the thiol chain length does not appear to be linear. On average, better defined fingering structures are observed

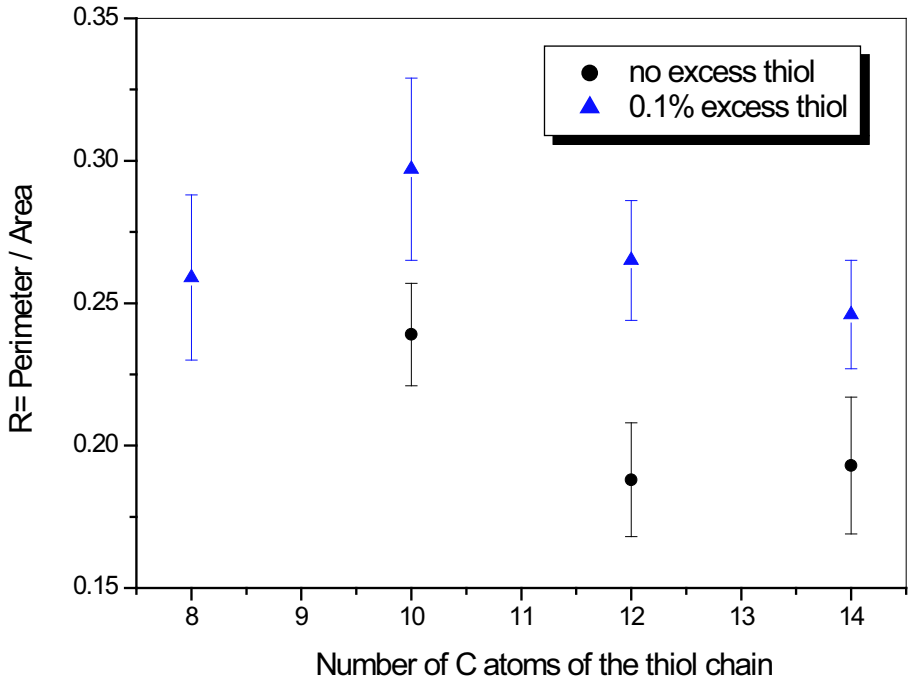

Figure 5.11: *Variation of the ratio R (associated with the degree of complexity of a given pattern), as a function of the thiol chain length of the passivating layer of the particles, in both the presence and absence of excess thiol in solution.*

on samples prepared with a C_{10} solution, compared to other solutions. In the absence of excess thiol, a threshold in the thiol chain length (between C_8 and C_{10}) seems to exist for the formation of well-defined fingering. This threshold is somewhat less obvious in the presence of thiol, where the error bars are larger. R decreases for longer chains, indicating less complex structures for C_{12} and C_{14} solutions (which exhibit similar values of R in both cases).

The most plausible explanation of these results is the interdigitation effect discussed earlier. The fact that the variation is not monotonic and peaks around a 10 carbon atom chain seems to indicate that the competing effect mentioned earlier between interdigitation and van der Waals interaction, to either slow down or facilitate interparticle diffusion, is possibly taking place.

Indeed, the apparent peaking of R for C_{10} particles may arise due to some balance of interparticle interaction energy (which decreases as a function of chain length) and nanoparticle fluid "viscosity" or "stickiness" (which increases as a function of chain length). For longer chains, the interaction between the gold kernels becomes weaker but, in the mean time, the interdigitation between adjacent particles is bound to be higher and thus increase considerably the diffusion barrier that particles that come into contact with each other have to overcome, hence increasing the overall viscosity of the solution. These results suggest that C_{10} particles may have the correct level of "stickiness" (in terms of both thiol-thiol and Au-Au interactions) to drive the formation of very well-defined and developed fingers, reminiscent of DLA-type structures.

For C_{12} and C_{14} nanoparticle solutions, the complexity of the fingering patterns decreases significantly compared to the C_{10} case, both in the absence and in the presence of excess thiol. We may refer here to the work by Motte and Pileni [124], who state that end gauche defects in C_{14} chains (which determine the cis-trans conformation of the molecule, refer to [124] for a complete description) tend to produce interdigitation which is less pronounced than for shorter thiol chains - a plausible origin of the less well-developed fingering observed for C_{14} (Fig. 5.7(e) and 5.8(e)). However, although this effect may explain the decrease of the fingering complexity for C_{14} particles, it does not justify a similar behaviour for C_{12} particles (where it is not present).

Finally, excess thiol either enhances the formation of fingering or induces it in unfavourable cases (C_5 and C_8 particles), but, on average, does not seem to alter the variation of R significantly (the highest values of R are always measured for C_{10} particles, and values for C_{12} and C_{14} particles, although

lower, remain in the same range with regard to each other). Indeed, it is sensible to suppose that the presence of excess "sticky" molecules in solution will contribute to slowing down the particle diffusion, but will not influence the interparticle interaction, thus enhancing only one of the competing effects. *On average*, the values of R are multiplied by 1.2, 1.4 and 1.3 in the C_{10}, C_{12} and C_{14} cases respectively, which would suggest that the strength of this effect does not increase linearly with the length of the molecule chain, but is almost constant. However, a better statistics on our values would be necessary to confirm this assumption.

Density-density correlation function

In a first approximation, the ratio R represents a satisfactory mean of establishing a hierarchical order of complexity within our fingering patterns, but error bars due to either poor statistics or high dispersion are sometimes problematic, as illustrated in the case with excess thiol discussed above (Fig. 5.11). On the longer term, we have decided to adopt another description that involves the fractal dimension of the patterns, since this parameter is most universally chosen for quantifying branched structures. This quantification method, which uses the so-called correlation function algorithm [126], yields results which are coherent with the box-counting fractal dimensions [127], and error bars which are generally smaller. The fractal dimension calculated with either algorithm must be interpreted critically, but the combination of these methods seems to lead to accurate determinations of fractal character. The correlation function method will be used thereafter for establishing the comparison between experimental and simulated results (see Section 5.5.3).

A brief description of the correlation function algorithm is as follows. The density-density correlation function is defined as :

$$C(r) = \langle \rho(r')\rho(r'+r) \rangle \tag{5.3}$$

with ρ=1 in the least viscous phase (air) and ρ=0 in the most viscous phase (nanoparticles). r is the distance from the "centre" of the correlation function. In practice, binary images of the isolated patterns are converted into a density map $\rho(x, y)$, which is then two-dimensionally Fourier transformed using a FFT algorithm. The spectral density $\sqrt{2\pi}|\tilde{\rho}(k_x, k_y)|^2$ is obtained, which is inverse Fourier transformed to give $C(x, y)$. $C(r)$ is obtained by radially averaging $C(x, y)$ [106, 128]. $C(r)$ is calculated and averaged over several similar-looking fingering patterns on the sample, whenever possible. It follows a power law $r^{-\delta}$, where the fractal dimension D_0 is related to δ by :

$$D_0 = d_e - \delta \tag{5.4}$$

where d_e is the Euclidean dimension and equal to 2 here.

An application of this algorithm is shown in Fig. 5.12. The initial experimental AFM image, Fig. 5.12(a), was obtained with C_{12} nanoparticles after ring deposition and shows several similar-looking fingering structures. Each of these patterns is isolated in turn, as illustrated in Fig. 5.12(b). The correlation function $C(r)$ is calculated for this specific pattern and the fractal dimension is deduced from the variations of the slope of $C(r)$ (graph annotated "D_0" in Fig. 5.12(c)). The same procedure can be carried out on the other fingering patterns of the initial image and D_0 averaged. The region of the $D_0(r)$ graph

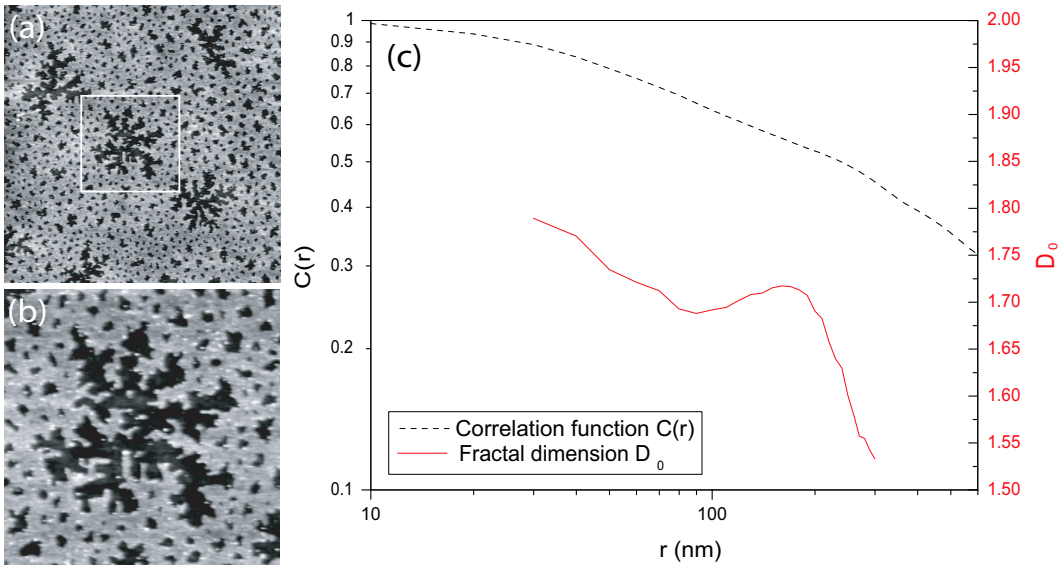

Figure 5.12: *(a) 10µm×10µm AFM scan of viscous fingering patterns obtained with a solution of C_{12} nanoparticles; (b) close-up view of one isolated fingering pattern, corresponding to the 2µm×2µm square in (a); (c) correlation function $C(r)$ and "local" fractal dimension D_0 (local slope of $C(r)$) associated with (b). r is the correlation length. Courtesy of Andrew Stannard.*

to be considered for estimating the fractal dimension is the intermediary region between the two inflexion points [127]. The chosen value for D_0 is that corresponding to the median point of this region (for a sufficient number of averages, this region will be flat). In this example, we find $D_0 = 1.70 \pm 0.05$. A good approximation of the fractal dimension associated with fingering patterns on a given sample can generally be obtained by combining this method with the results of a standard box-counting algorithm.

5.4 Theoretical models of nucleation and finger growth

Only a very small number of theoretical models have been established to describe the formation and growth of branched patterns in liquid thin films. Moreover, the presence of nanoparticles has not been taken into account in these models. Recently, theories such as that proposed by Elbaum and Lipson [107], have attempted to provide a coherent picture of the nucleation events and the receding of the liquid front following nucleation, in particular in the presence of a solute. Possible models have also been put forward in the literature in order to explain fingering formation at the liquid front. We will review in particular the descriptions by Samid-Merzel *et al.* [108] and Lyushnin *et al.* [109]. These theoretical considerations constitute the only analytical theories which have attempted to identify the mechanisms at play in the formation of ramified holes in dewetting thin liquid films. This remains an open question, in particular in the case of colloidal solutions of nanoparticles.

5.4.1 Formation of a solvent bump - Coexisting thin and thick films

Our system falls into the category of volatile totally-wetting films, a subject which certainly lacks the well-developed literature on non-volatile partially-wetting liquids. However, Elbaum and Lipson [107] have turned their attention to such systems by studying the dewetting of water from a clean mica surface, and have put forward a number of theoretical considerations from experimental

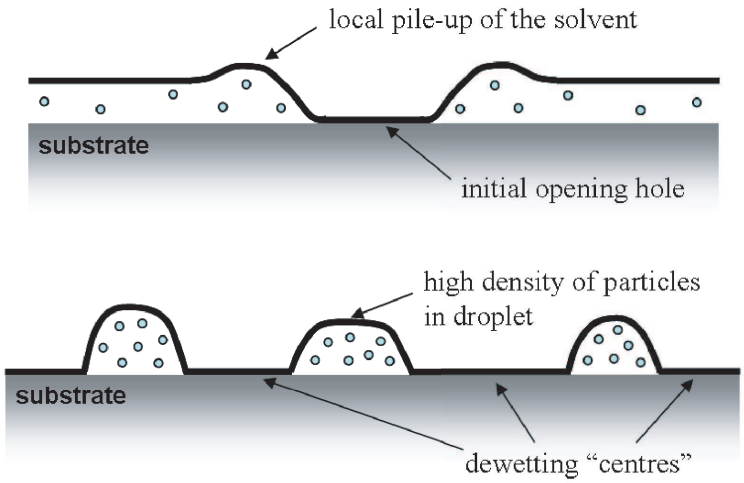

Figure 5.13: *Model proposed by Elbaum and Lipson [107] : a solvent bump forms at the edge of the initially nucleated hole. As more and more holes open, regions of very high nanoparticle concentration are created where a second nucleation step occurs, introducing secondary length and time scales into the dewetting process, that can account for the coexistence of different types of patterns with different length scales, as seen experimentally.*

observations. They thereby extend the proposition made by Brochard-Wyart and Daillant [129] that stated that the nucleation of patches could occur even in totally-wetting films of non-volatile solvent. After observing these nucleation events experimentally for water in equilibrium with its unsaturated vapor on a mica substrate, Elbaum and Lipson made the assumption that the spreading of the nucleated hole led to the formation of a solvent bump at the edge of the patch (the nucleation itself originates from the evaporation or disjoining pressure, see [107] and [129]).

This concept needs to be considered in the context of colloidal gold nanoparticle solutions. In this configuration, the nucleation and growth processes would occur according to the mechanism depicted in figure 5.13. Once a nucleated hole opens in the totally-wetting layer of solution, the sol-

vent front (or "bump") retreats, carrying with it nanoparticles. When several patches open in the vicinity of the initial hole, the receding fronts meet and form droplets of very high nanoparticle concentration, into which a new nucleation event can then take place. This description introduces a second length scale and time scale to the problem : the holes nucleated in regions of high nanoparticle concentration will be significantly smaller than the initial ones (they spread within droplets which are limited in size by the initial patches) and will form later in time (once the retreating bumps of nearby patches have met). In particular, this mechanism accounts for the formation of patterns on different length scales, such as multiple cellular networks, as seen in the introductory section of Chapter 4.

Based on this description of solvent bump formation, Samid-Merzel *et al.* [108] made the additional assumption that at the edge of the nucleated patch, a molecularly thin film and a macroscopically thick film coexisted. The thin

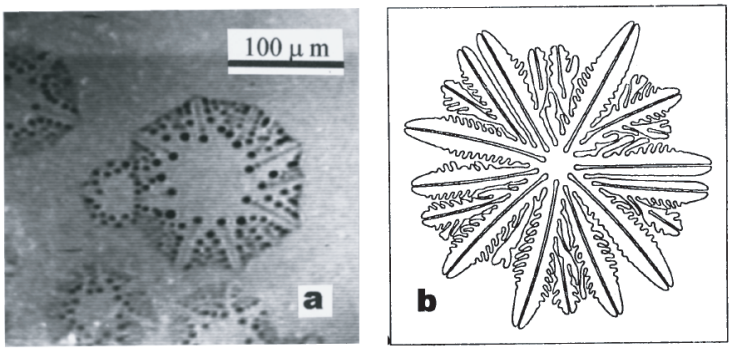

Figure 5.14: *Pattern formed by water dewetting from a clean mica surface : (a) experimental image, (b) pattern produced with the model proposed by Samid-Merzel et al. [108] : a molecularly thin film at the bottom of a nucleated hole and a macroscopically thick film at its edge coexist, which exhibit different dynamics. The rim undergoes and instability which finally produces complex branching patterns. From [108].*

film remaining at the bottom of the nucleated hole and the macroscopic rim formed at the edge of the growing patch exhibit different dynamics that drive the pattern growth and, in particular, are responsible for the development of an instability in the retreating front. As the instability occurs, the front starts forming fingers that grow into creating a very complicated drying pattern (Fig. 5.14(b)). They indeed observed these patterns experimentally, once again in a thin water film dewetting from mica (Fig. 5.14(a)). The details of the development of this instability will be discussed in the following paragraph. For now, note that the description of a thin precursor film left behind the retreating front is very reminiscent of the experimental observations of section 5.2, where fingering structures were found to evolve in a thin film *after* the front has receded.

5.4.2 Drying front instability

The theoretical models proposed by Elbaum and Lispon [107] and Samid-Merzel *et al.* [108] offer a convenient explanation of the evaporation process and the mechanism of pattern formation in systems such as ours. The validity of these models are discussed below, in Section 5.4.3. A third model was developed by Lyushnin *et al.* [109] in order to explain the influence of the evaporation rate on the growth of the fingering instability. In their model, Lyushnin *et al.* reproduced the shape of the retreating front (including a solvent bump and the coexistence of a thin and a thick film) at the edge of a nucleated hole, and monitored its evolution in time (Fig. 5.15(a)). They observed that for a quick evaporation (high evaporation rate), the bump gradually decreased and that the possible transverse perturbations along the interface

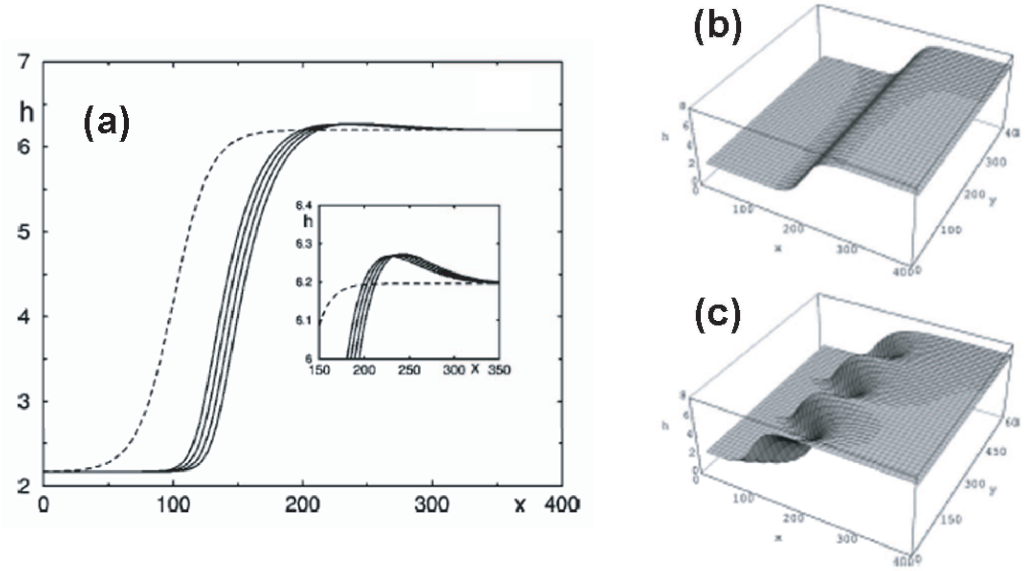

Figure 5.15: *(a) Profile of the retreating front (height) as a function of position. Lyushnin et al.'s model [109] monitors the evolution of the retreating front at the edge of a nucleated hole as a function of time. (b) For a quick evaporation, the bump gradually decreases and no perturbation has the time to develop perpendicular to the retreating front, which remains smooth (flat interface). (c) For slow evaporation times, the bump persists over a longer time and normal perturbations have the time to develop and grow, a fingering instability occurs.*

decayed very quickly in time, until being smoothed out (Fig. 5.15(b)). In these conditions, the resulting patterns do not exhibit a strong fingering character. On the contrary, in the case of slow evaporation (low evaporation rate), the bump persists over a much longer time and the transverse instability (Fig. 5.15(c)) is allowed to develop over much larger length and time scales, giving rise to fingering patterns that spread further than in the quick evaporation case. This proposition is rather intuitive and helps to understand why, in the case of spin-coated samples (quick evaporation), fingering patterns are very difficult to obtain, whereas they are quite common on samples prepared with the meniscus technique (slow evaporation). However, we have occasionally ob-

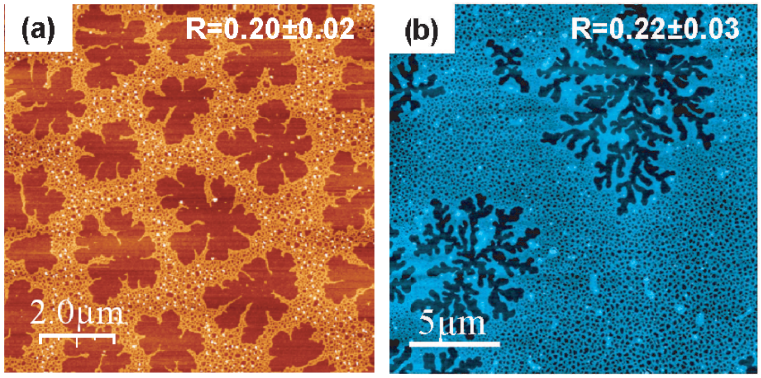

Figure 5.16: *(a) Quick evaporation of a C_8 nanoparticle solution onto a silicon substrate (by spin-coating) and (b) slow evaporation of a C_{12} solution onto a similar susbtrate (by meniscus-driven evaporation). The scales of the AFM scans are given in each case, as well as the value of the ratio R, that quantifies the degree of complexity of branched structures.*

tained poorly-developed fingering structures from spin-coating, as illustrated in Fig. 5.16, which indeed correspond to Lyushnin *et al.*'s description, .

Figure 5.16(a) shows an AFM scan of a sample prepared by quick evaporation (spin-coating), whereas figure 5.16(b) was taken on a sample prepared by slow evaporation (meniscus-driven evaporation). In the first case, we "freeze" the system at an earlier time so that the fingers cannot develop. In the second case, the feature spreads over distances that are about 5 times superior to the first case ($\sim$10μm compared to $\sim$2μm). However, the calculation of the ratio R for both images shows that the structures formed in both cases are - within error - of similar complexity, despite their strikingly different appearances (R=0.20$\pm$0.02 in the first case, 0.22$\pm$0.03 in the second case).

5.4.3 Validity of the theoretical models

The Sarfus experiment described in Section 5.2 was the first real time observation of nanoparticle adsorption on a surface during evaporation and shed light

upon the mechanism of solvent evaporation and front instabilities, hence confirming some of the theoretical considerations presented above, while ruling out others (video available in [92] - Supplementary Material). Indeed, no solvent bump formation was witnessed at the rim of nucleated holes, which contradicts Elbaum and Lipson's assumption [107]. However, it was demonstrated that nucleation occurred within a very thin "precursor" film at the solvent-substrate interface, after the front has retreated, which is coherent with the coexistence of a molecularly thin and a macroscopically thick film described by Samid-Merzel *et al.* [108].

Concerning the formation of a fingering instability *at* the solvent front, the video showed that such an instability was only present at the beginning of a meniscus-driven evaporation but disappeared towards the end, as the evaporation rate is reduced [92]. For a slow enough evaporation, fingering occurs following nucleation in a thin liquid film, not *at* the liquid front. This contradicts Lyushnin *et al.*'s prediction [109] : the fingering instability *at* the solvent front does not grow at low evaporation rates, it disappears. According to experiment, it is only present for a fast enough evaporation.

However, in the video, we are considering the phenomena at the *macroscopic front* of liquid following initial dewetting in the centre of the Teflon ring. If we now consider the microscopic dewetting front within the thin precursor film - at low evaporation rates - *at the edge of a nucleated hole*, the resolution of the video does not allow to prove such a contradiction with Lyushnin *et al.*'s model anymore. It is possible that the microscopic dewetting front indeed evolves as described by Lyushnin *et al.*, which would explain why such well-defined and widely-spread *radial* fingering structures are observed on the

edge of samples prepared with the meniscus technique - where the evaporation rate is the lowest. Note however that Lyushnin *et al.* assumed the presence of a solvent bump at the rim of a nucleated hole, which could not be observed experimentally.

As a conclusion, the three models discussed here propose several interesting leads to explore in order to identify the mechanisms at play in dewetting-induced pattern formation. An uncertainty remains on the formation of a solvent bump at the rim of a nucleated hole and the development of a transverse front instability at low evaporation rates. However, the coexistence of both a thin and a thick film seems probable in view of experimental results (Section 5.2). In 2003, a simulation model was developed by Rabani *et al.* [1], that was later improved and extended by Martin *et al.* [81] and Yosef and Rabani [82], to describe evaporation and dewetting of thin nanoparticle-liquid films such as ours. Their simulations adopt some of the assumptions and considerations detailed above. This model, and subsequent modifications we have made to it, will be the subject of our final section and brings considerable insight into the mechanisms of pattern formation in colloidal nanoparticle assemblies.

5.5 Simulations

The tuning of pattern formation has been the centre of attention in the course of this thesis. Previous studies in our group [47, 50] have helped clarify some of the mechanisms of pattern formation and identify the interplay of principles responsible for the behaviour of colloidal nanoparticles on solid substrates. Some experimental cases have been successfully related to spinodal dewetting

effects, heterogeneous nucleation, Marangoni convection effects, etc. and to some degree, the mechanisms of the formation of a number of patterns in given experimental conditions have been identified [47, 50]. This has been made possible by the elaboration of a model, inspired from previous work by Rabani *et al.* [1] and further developed within the group by Martin *et al.* [81], which simulates the behaviour of nanometer-size particles deposited from a volatile solvent onto a wetted solid substrate. The details of the model are given below. However, the development of the meniscus technique puts into play some very specific experimental conditions, which cannot be accounted for in the initial model. As a result, further development of the model [86] has been necessary to adapt the theoretical description of the system to these new experimental conditions and the new types of patterns associated with them.

5.5.1 Two-dimensional model

We use a model adapted from that of Rabani *et al.* [1] to describe the self-organisation of colloidal gold nanoparticles. In this model, the solvent is represented as a two-dimensional square lattice gas. Each lattice cell is occupied by either liquid, nanoparticle or gas (empty) and is 1nm (ξ) in size, which corresponds approximately to the correlation length of the solvent. Each particle is represented by a square of side 3nm (Fig. 5.17). In the original 2D model, the amount of energy associated with every liquid-vapour conversion (or vice-versa) is calculated while taking into account the nearest neighbours of each site only. The improved version of the 2D model by Martin *et al.* [81], which has since then been generally adopted, incudes the next-nearest neighbours as well. The Hamiltonian of the system is given in Eq. 5.5 :

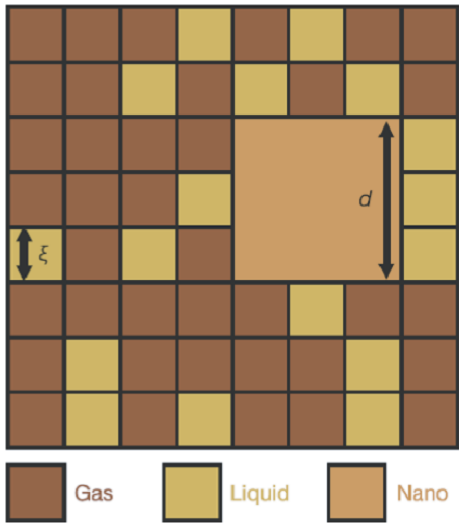

Figure 5.17: *A sketch of the square lattice and length scales of the model. Each lattice cell of size ξ is occupied by gas, liquid or nanoparticle. Each nanoparticle spans 3×3 cells. Nanoparticles can only move into "wet" sites. From [1].*

$$H = -\epsilon_l \sum_{<ij>} l_i l_j - \epsilon_n \sum_{<ij>} n_i n_j - \epsilon_{nl} \sum_{<ij>} n_i l_j - \mu \sum_i l_i, \tag{5.5}$$

where ϵ_l, ϵ_n, and ϵ_{nl} are the attraction strengths between two adjacent sites that are occupied by solvent, nanoparticle, or solvent and nanoparticle, respectively. The equilibrium state of the solvent is defined by μ, the chemical potential, and T, the temperature of the system. The model relies on a Monte Carlo algorithm , where nanoparticles perform a random walk across the lattice. An important assumption is that nanoparticles can only move into "wet" sites, that is if they have 3 neighbouring liquid sites on one side (the nanoparticle in Fig. 5.17 can only move to its right, for instance). Once adsorbed on the surface, nanoparticles are immobile. A given mobility is assigned to the particles in the solvent, depending on the experimental conditions that are being reproduced.

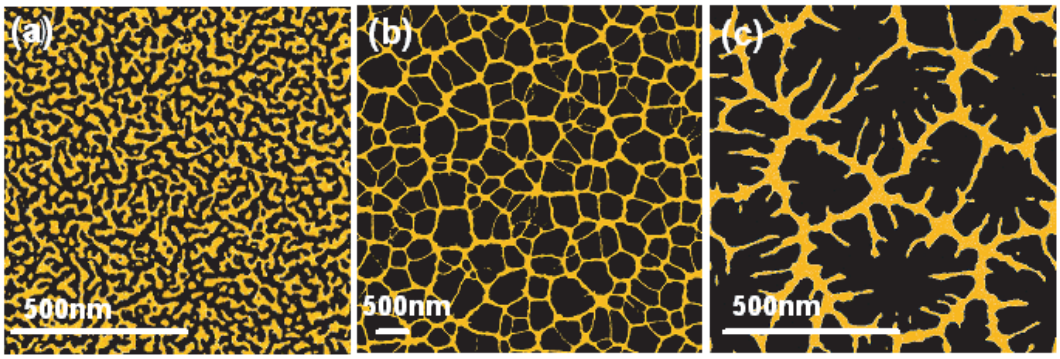

Figure 5.18: *Different morphologies obtained from simulations showing (a) a 1008×1008 lattice at a given temperature T, high mobility M and a coverage of 30%, after 69 Monte-Carlo steps, (b) a 4008×4008 lattice at temperature T/2, mobility M, coverage 20%, after 1003 MC steps and (c) a 1008×1008 lattice at temperature T/2, low mobility M/3, coverage 20%, after 1003 MC steps (courtesy of Christopher Martin).*

Using this model, a broad range of structures were produced. Three examples of simulated pattern formation are represented in figure 5.18. Fig. 5.18(a) shows ribbon-like interpenetrating domains of particles, very reminiscent of spinodal decomposition (see chapters 2 and 4). This is obtained when the mobility of the particles is high and with a 30% final coverage. Fig. 5.18(b) shows cellular networks and is obtained in conditions similar to (a). Only the temperature has been varied, which is equivalent to changing the volatility of the solvent (higher in the first case). Figure 5.18(c), on the other hand, has been obtained by reducing drastically the mobility of the particles. In this case, the particles cannot move fast enough as the liquid front retreats following nucleation. As a result, the front does not keep its polygonal shape when growing (like in Fig. 5.18(b)) and the particles are pinned to the surface in finger-like protrusions reaching into each cell. All these patterns have been observed repeatedly in experiments involving spin-coated samples, where the evaporation is very fast and resulting nanoparticle arrangements are homogeneous over the

whole substrate [47, 81].

These straight forward Monte Carlo simulations allow us to understand the formation of some types of patterns, depending mainly on the evaporation rate of the solvent, its volatility, the mobility of the particles and the coverage over the surface (some of these parameters being intrinsically related to one another). A more detailed comparison of the model with experimental results is available in [47] and [81]. However, it presents a number of apparent limitations. For example, it does not produce patterns over several length scales (cellular networks) or several types of coexisting patterns (branched patches surrounded by secondary nucleated small holes, like in Fig. 4.3(f) of Chapter 4 for example). The reason for this could be that if the theory of a solvent bump formation holds, then it cannot be reproduced in a two-dimensional model. The present model would need to include a third dimension or, more generally, a description encompassing solvent flow (i.e. convection) - rather than just evaporation [1] - in order to account for the existence of a macroscopically thick layer of liquid as well as a quasi-2D thin film. More basically, no interaction with the substrate is described by the Hamiltonian of Eq. 5.5, which is bound to introduce flaws into the model. These were some of the reasons that led to the extension of the model in order to include a third dimension. Several approaches are possible to solve this issue (which implies a considerable complexification of the present model), which will now be discussed in terms of their relevance to our experimental conditions and results.

5.5.2 Three-dimensional model

Yosef and Rabani (YR) [82] have recently developed a 3D model based on Rabani *et al.*'s original 2D code [1], including Martin *et al.*'s later modifications [81]. For the first time, they simulated ring-shaped nanoparticle assemblies, which had been observed experimentally several times in the past [2,69], notably by Pileni's group, and more recently by ourselves (see Chapter 6). Their 3D model introduces a third spatial dimension by considering the last few layers of solvent above the substrate during evaporation. A nucleation site is inserted in a given location on the surface prior to evaporation, where the hole will start growing following dewetting. Importantly, the global evaporation rate of the solvent, the hole growth rate and the hole nucleation rate can be adjusted separately. Note that in the YR model, the particles are attracted to the surface and that nucleation occurs in the thin layer of liquid directly above the substrate, that is at the solvent-substrate interface, due to the effect of disjoining pressures [1, 82, 107]. This is in agreement with our experimental observations (section 5.2).

For a set of values in the parameter space that corresponds to a long evaporation time and a low mobility of the particles (i.e. a slow global evaporation compared to that at the rim of the nucleated hole, and a slow diffusion of particles), the ring of particles evolves into a striking fingering structure (Fig. 5.19). The conditions described by the YR model are very reminiscent of our own experiment. Indeed, in the region of the sample where viscous fingering is usually observed, evaporation typically takes from a few to tens of minutes. Furthermore, the mobility of the particles is considerably reduced for the particles with the longest thiol molecules or in the presence of excess thiol.

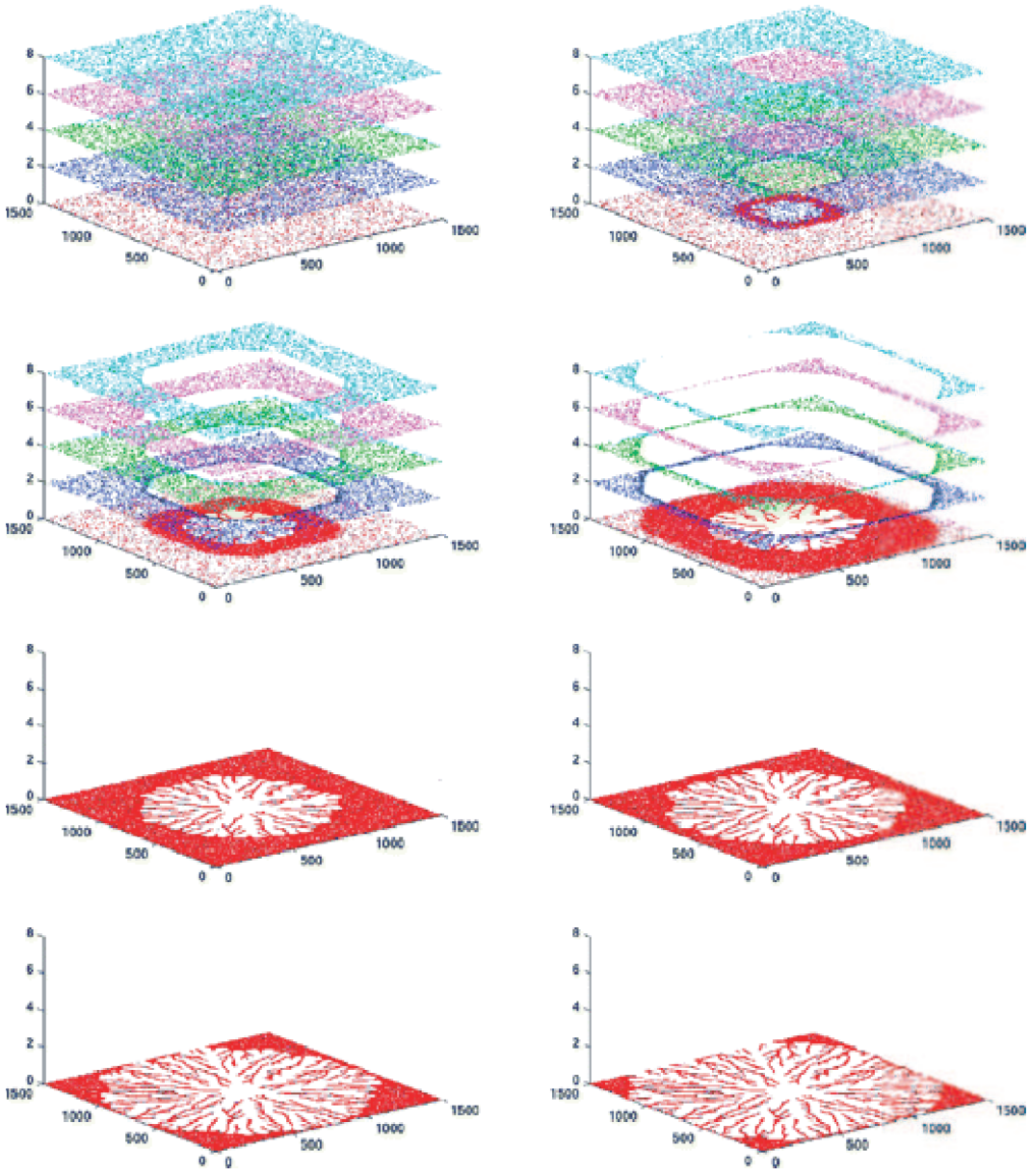

Figure 5.19: *From top left to bottom right (from 100 to 3800 Monte Carlo steps) : evolution of the nanoparticle arrangement in an initially thick film of nanoparticle solution evaporating from a solid substrate (the bottom eight layers of nanoparticle solution are shown in steps of two layers, each particle is* $2\times2\times2$ *lattice sites in size). The conditions are : low evaporation rate, very low mobility of the particles and long diffusion time. The scales of the graphs are given in nm (1500nmtimes1500nm frames). From [82].*

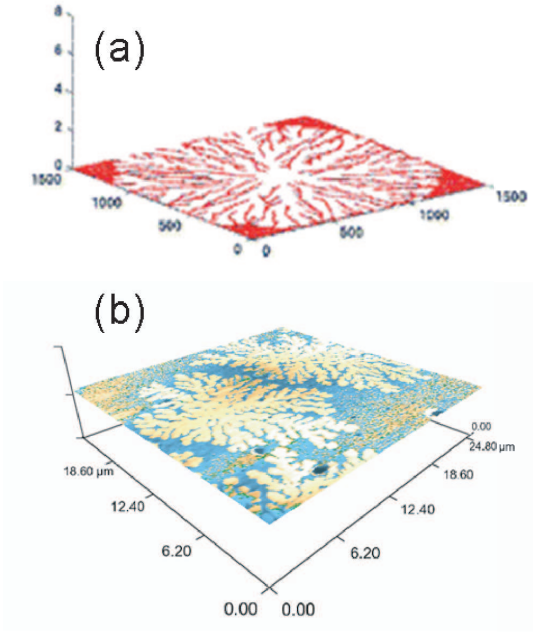

Figure 5.20: *(a) Final snapshot (3800 MC steps) of the YR simulation in the case of slow evaporation and slow particle motion, from [82]; (b) 3D representation of an AFM image of dodecanethiol-passivated nanoparticles onto silicon native oxide. In both cases, the branched feature is a hole, i.e. free of nanoparticles. The image sizes are respectively 1.5µm×1.5µm and 25µm×25µm.*

When monitored by video camera, the actual evaporation of the solvent takes place in 3 steps, very similar to the ones described by YR (first the film thins slowly and homogeneously, then dewetting occurs and the front retreats very rapidly before reaching a slower and stable evaporation regime in the outer regions of the sample, where viscous fingering forms). The fingering structures observed experimentally for C_{10}- or C_{12}-nanoparticles (for which the ratio R is the highest) show striking similarities with the highly complex branched patterns obtained by YR, as shown in Fig. 5.20.

This improved fully-3D model represents a major advance into the description of our system. For the first time, it reproduces the formation of fingering

holes in sub-monolayers of colloidal nanoparticles, in a parameter range that fits perfectly with our experimental conditions. However, YR do not report the experimental observation of such patterns. In addition, while their model produces well-defined isolated fingering structures, it does not seem to reproduce isolated structures separated by different length scale patterns, such as what we see in our experiments. Finally, one major discrepancy of the YR model with regard to experiments is that it necessitates the introduction of a predetermined site for nucleation to take place, which has no physical equivalence experimentally.

5.5.3 Pseudo-3D model

The initial 2D model, although it reproduces numerous nanoparticle arrangements both qualitatively and quantitatively, does not produce patterns such as those seen in Fig. 4.3(f), where several structures and, often, length scales coexist. The 3D model produces isolated rings and fingering patterns such as those seen experimentally but involves the introduction of a nucleation site at the solvent-substrate interface as an initial condition to dewetting. A different approach was developed by Martin *et al.* [50] and consists of including a dependency of the chemical potential of the solvent, μ, as a function of solvent density (i.e. solvent coverage) into the original 2D model - where μ only defined the equilibrium state of the solvent and was used to represent any interaction not otherwise explicitly taken into account. The new Hamiltonian of the system is thus given by Eq. 5.6 :

$$H = -\epsilon_l \sum_{<ij>} l_i l_j - \epsilon_n \sum_{<ij>} n_i n_j - \epsilon_{nl} \sum_{<ij>} n_i l_j - \mu(\nu) \sum_i l_i, \qquad (5.6)$$

where ϵ_l, ϵ_n and ϵ_{nl} are, as in Eq. 5.5, the liquid-liquid, nanoparticle-nanoparticle and liquid-nanoparticle interaction energies respectively, and ν is the fraction of liquid that has converted to vapour.

By exploring the parameter space of this *pseudo-3D* model, one can obtain spontaneously forming viscous fingering surrounded by smaller secondary nucleated holes, as illustrated by Fig. 5.21. The experimental images of Fig. 5.21(a) and (b) show such nanoparticle arrangements, whereas Fig. 5.21(c) and (d) show the simulated images. The latter are calculated with conditions reminiscent of that described in the YR model : low mobility ratio, i.e. slow diffusion of the particles compared to solvent evaporation ; low temperature, such that the rate of nucleation is reduced and features are given enough time to grow and develop ; high nanoparticle coverage (up to 50% in order to match typical experimental data). In Martin *et al.*'s *pseudo-3D* model, the chemical potential is no longer constant - unlike in the 2D model [1,81] - but is a function of global solvent density. An increase in chemical potential magnitude results in increased evaporation, hence, increasing the chemical potential as the solvent layer thins results in an increased evaporation rate with decreasing solvent coverage [50, 130]. A chemical potential inversely proportional to the solvent density leads to the creation of nucleated holes in the film and nanoparticle rings are produced, surrounded by smaller length scale nanoparticle arrangements [50]. In order to produce the patterns observed in Fig. 5.21(c) and (d), a sigmoid-derived functional form of the chemical potential, of the form given

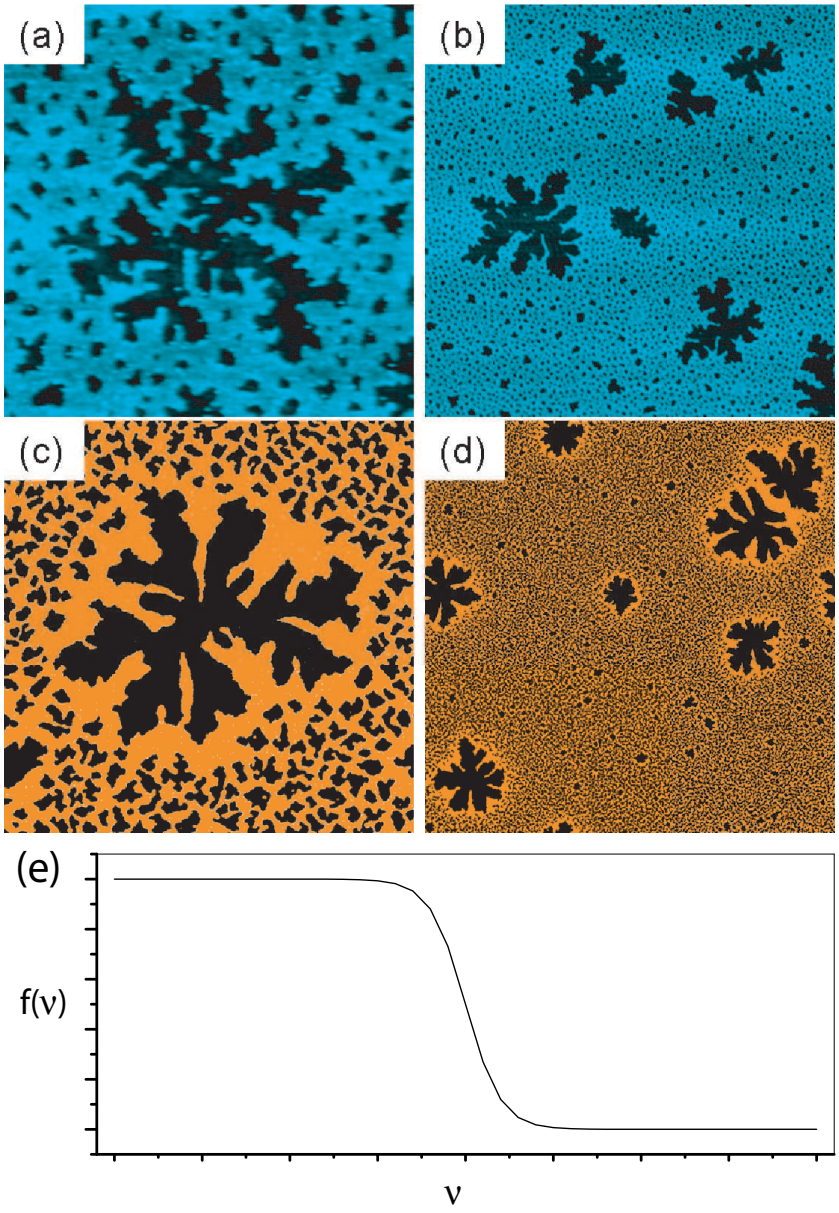

Figure 5.21: *(a)-(b) AFM images of fingering patterns obtained by depositing a C_{12} nanoparticle solution via the meniscus technique (scans 2×2 and 10×10μm^2 in size respectively); both images display coexisting fingering patterns with secondary nucleated holes. (c)-(d) Final frames of numerical simulations (frame size 2048×2048, equivalent to 2×2μm^2) involving low mobility, low temperature and high (50%) coverage; courtesy of Andrew Stannard. (e) Schematic of a sigmoid-like function.*

by Eq. 5.7, is used (Fig. 5.21(e)).

$$\mu(\nu) = \mu_0(1 + \frac{\Delta\mu_f}{1 + \exp(-\frac{\nu-\nu_s}{\sigma})}) \tag{5.7}$$

where μ_0 is the initial chemical potential and $\Delta\mu_f$ is the fractional change in chemical potential (i.e. the step height, Fig. 5.21(e)). ν_s defines the position of the centre of the step and σ is the step width. A switch in chemical potential between two values occurs for a certain solvent coverage : initially, fingering structures form - as a consequence of the chosen parameters described above - via nucleation and growth at a given chemical potential. Then, as the solvent density decreases (i.e. ν increases), the chemical potential coupling causes the solvent evaporation rate to increase : thermal nucleation occurs widespread throughout the simulation and the smaller length scale features are formed [128].

The simulation images of Fig. 5.21(c) and (d) qualitatively reproduce the experimental images to a very good approximation. The fractal dimensions of both experimentally and numerically obtained patterns are estimated according to the method described in section 5.3.2. The comparison of the resulting correlation functions and fractal dimensions for images 5.21(a) and (c) is shown in Fig. 5.22. The value obtained for the simulated pattern, Fig. 5.21(c), averaged over 8 realisations, is 1.75±0.03 which is consistent within error with the fractal dimension of the target image, Fig. 5.21(a), as calculated in section 5.3.2, i.e. 1.70±0.05 (Fig. 5.12). The simulated image is thus in good *quantitative* agreement as well with the experimental data.

To conclude, although viscous fingering was not, so far, a very commonly

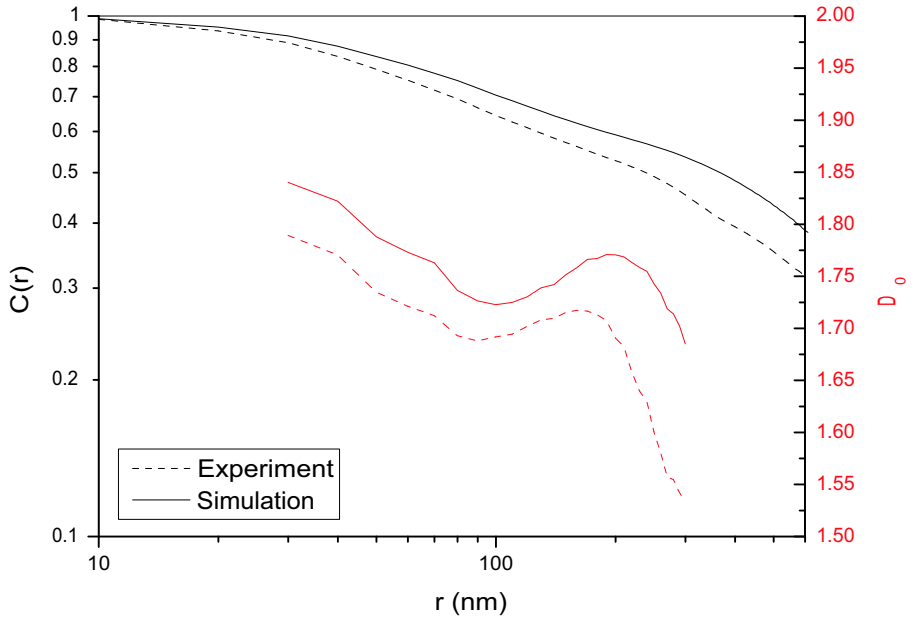

Figure 5.22: *Averaged correlation functions ($C(r)$) and "fractal dimensions" (D_0) calculated for the experimental (dashed line) and numerical (full line) images of Fig. 5.21(a) and (c) respectively. The calculation for the experimental data is taken directly from section 5.3.2 (Fig. 5.12) and yields $D_0 = 1.70 \pm 0.05$. The calculation for the numerical image is averaged over 8 realisations of fingering structures and yields $D_0 = 1.75 \pm 0.03$. Results are quantitatively consistent within error. Courtesy of Andrew Stannard.*

observed feature in nanoparticle assemblies, we have identified the narrow experimental parameter range associated with the phenomenon, and were able to deduce a number of mechanisms to account for the formation and growth of such patterns. Thanks to the real-time observation of nanoparticle deposition carried out with the Sarfus apparatus, we can now confidently assert that nanoparticle assembly, in the case of a meniscus-driven evaporation, takes place at the solvent-substrate interface [106]. This, in addition, is to some extent in agreement with some pre-existing theoretical considerations [107–109] and with the convention adopted for the simulations [1,81,82]. Fingering patterns form in a nanoparticle-solvent thin film following hole nucleation. The

manner in which they develop and their degree of complexity then depend on the experimental conditions, which influence quite dramatically the solvent-nanoparticle-substrate mutual interactions. The role of each experimental parameter has been elucidated, to the extent where the effects can be linked to a key parameter : the nanoparticle mobility or, in terms of a continuum, rather than microscopic, picture, the fluid viscosity. Finally, the pseudo-3D model that was developed within our group [86, 128] produces fingering patterns that are faithful (both qualitatively and quantitatively) to the experimental data and offers a description of the nucleation and growth processes, as well as the evaporation processes, that are consistent with experimental observations. This model is a simpler alternative to a fully 3D model, such as that developed by YR [82], and it does not necessitate the artifacts required by YR for the occurrence of hole nucleation, thus offering the most realistic description of the behaviour of our system to date, and confirming the mechanisms of viscous fingering formation hinted by experimental results.

Chapter 6

Wetting Properties and Pattern Formation

"Savoir s'étonner à propos est le premier pas fait sur la route de la découverte."

Louis Pasteur.

In Chapter 4 it was demonstrated that colloidal nanoparticle self-organisation could to some extent be tuned via a novel deposition technique and the associated variation of the evaporation process. More fundamentally, the behaviour of the nanoparticle-solvent-substrate system that we are studying is dictated by numerous interactions, over which we can gain a certain degree of control. The wetting properties of the system, in particular, play a central role in pattern formation. These properties can be altered at the nanoparticle level (e.g. via functionalisation of the nanoparticle surface), but also from the point of view of the surrounding media (solvent and substrate). The roles of both the solvent and the substrate in determining nanoparticle organisation are examined here.

6.1 Wetting of the solvent

The aim of this chapter is to demonstrate that one can use wetting-related variations in order to influence the self-organisation of colloidal nanoparticles on a surface. In a way, this idea is neither original nor new : our group and others have worked and published on this subject in the past, be it to report advances concerning the wetting properties of the nanoparticles themselves [90], or improvements in the control of the substrate's wettability and its influence on nanoparticle arrangements [86]. However, many open questions remain about the direct correlation between wetting properties and pattern formation. Hydrophobic and hydrophilic particles were introduced in Chapter 3 and represent an apparent ideal combination to obtain wetting-directed self-organisation (although it was explained before that finding a solvent or a well-controlled mixture of solvents to keep both types of particles in suspension is an important issue to be addressed). As for the alteration of the substrate's wetting properties, the creation of micro- or nanoscopic hydrophilic areas on an hydrophobic substrate using an AFM tip (see [47] and [50] for a description of the technique) offers a reliable technique for designing substrates with custom-made local wettability [86]. However, both these experiments are out of the scope of this thesis and we shall concentrate in this chapter on the wetting properties of the remaining element of the system - the solvent - and its influence on nanoparticle pattern formation via the modification of the nanoparticle-solvent-substrate mutual interactions and, hence, the dewetting process.

6.1.1 Altering solvent-substrate-nanoparticle interactions

The 2nm thiol-passivated gold nanoparticles that are used in this study (Section 3.1) are suspended in toluene following two-phase synthesis [87]. However, they can be dried out of solution and redissolved at will in a different organic solvent. To strongly affect the dewetting of the nanoparticle solution on a substrate, we need to find solvents which exhibit significant differences, that is solvents whose physical constants cover as large a range of values as possible. In particular, we have seen in Chapter 2 that the Hamaker constant, which describes the interaction of two media through a third one, depends directly on the dielectric constants of the three media involved. Moreover, another major difference can arise from the volatility and viscosity of a given solvent. Each of these considerations is discussed below and contributed to the choice of relevant solvents for our experiment. Note in addition that several types of substrates are available for this experiment, ranging from native oxide terminated silicon to hydrogen passivated silicon, with which various degrees of hydrophilicity / -phobicity are associated.

Solvent-substrate interaction

The wetting of a surface by a liquid is influenced by the physical properties of the liquid (medium 3), the solid (medium 2) and the surrounding medium (air, medium 1), and in particular depends on their dielectric constants and refractive indices. We gave the Lifshitz definition of the Hamaker constant in Chapter 2 (Section 2.1.2, Eq. 2.4). For the practical purpose of calculating Hamaker constants in this chapter (see Section 6.1.2), however, we shall use a description adapted from that of Bergström [131] :

$$A_{132} = \frac{3kT}{2}\Delta_{13}(i\xi_m)\Delta_{23}(i\xi_m) \tag{6.1}$$

where ξ_m is defined as follows :

$$\xi_m = m\frac{4\pi^2 kT}{h} \tag{6.2}$$

For the purpose of this calculation, m is taken equal to 1 [131]. The $\Delta_{pq}(i\xi_m)$ terms are of the form :

$$\Delta_{pq}(i\xi_m) = \frac{\varepsilon_p(i\xi_m) - \varepsilon_q(i\xi_m)}{\varepsilon_p(i\xi_m) + \varepsilon_q(i\xi_m)} \tag{6.3}$$

with [p,q]=[1..3,1..3] corresponding to the various media. $\varepsilon_p(i\xi_m)$ and $\varepsilon_q(i\xi_m)$ are the imaginary components of the dielectric responses of materials p and q respectively (p=1,2 or 3 and q=1,2 or 3) and are given by :

$$\varepsilon_p(i\xi_m) = 1 + \frac{C_{UV}(p)}{1 + \frac{\xi_m}{\omega_{UV}(p)}} \tag{6.4}$$

where $C_{UV}(p)$ is the absorption coefficient of material p in the UV range, given by $C_{UV}(p) = n_p^2 - 1$ (n_p, refractive index of material p), and $\omega_{UV}(p)$ is the characteristic absorption frequency of material p in the UV range.

This definition explicitly highlights the dependence of the Hamaker constant on both dielectric constant and refractive index. The values of ω_{UV} can be taken equal for all materials ($\sim 2\times10^{-6}$ rad/s), although this will lead to a systematic overestimation of the Hamaker constant (refer to [131]).

The dielectric constant and refractive index of *toluene* are respectively ε=2.379 and n=1.4961 [132]. Most organic solvents have a refractive index

within the 1.4–1.5 range, so we may look for a solvent that has a dramatically different dielectric constant instead, e.g. *dichloromethane*. The dielectric constant and refractive index of dichloromethane are respectively ε=8.93 and n=1.4242 [132]. A summary of all the values of physical constants that will be considered in this section can be found in Table 6.1.

Solvent-nanoparticle interaction

Changing the solvent in which nanoparticles are suspended also influences the diffusion of the solute in suspension. Nanoparticles diffuse both "freely" in the solvent and "around" each other. Interparticle diffusion will be discussed in Section 6.2. Diffusion in solution, for a given type and size of particle, is dictated by the "friction" between solvent and solute, which is usually weak for systems such as ours, as demonstrated by Wuelfing and co-workers [133]. In this limit of "slip conditions", for a given nanoparticle type (hence hydrodynamic diameter, see [133]), the diffusion coefficient of the solute only depends on the solvent viscosity and is inversely proportional to it.

The solvents that we have chosen for this study all exhibit viscosities which are similar, but not equal. For instance, there is a factor of two approximately between the viscosity of hexane (the least viscous of our solvents) and that of nonane (the most viscous one) [132]. Hence, when changing the nature of the solvent, one has to consider not only the wetting differences associated with the altered solvent-substrate interactions, but also to some extent the modification of the solvent-nanoparticle interaction. That is one of the reasons why, for the purpose of this study, we did not include dodecane in the list of solvents used, because its viscosity is much higher than that of any other selected

solvent (twice the value of nonane [132]), which would have induced a strong modification of the solvent-nanoparticle interaction, making it difficult to decouple the respective effects of individual experimental parameters. However, for now, we wish to concentrate on how altering wetting properties influences pattern formation. The study of the variation of diffusion coefficients and their subsequent effects constitute a different field of investigation altogether (which we touched on in the previous chapter).

Experiment : Choice of relevant solvents and substrates

Material	Molecular formula (organic solvents)	Dielectric constant ε	Refractive index n (at 589nm)
Air	n/a	1	1
Hexane	C_6H_{14}	1.8865	1.372725
Heptane	C_7H_{16}	1.9202	1.385525
Nonane	C_9H_{20}	1.9722	1.40582
Benzene	C_6H_6 (a)	2.2825	1.50112
Toluene	C_7H_8 (a)	2.379	1.49612
Mesitylene	C_9H_{12} (a)	2.279	1.49942
Dichloromethane	CH_2Cl_2	8.93	1.42422
Si	n/a	12.1	4.01
SiO_2 (silica)	n/a	4.42	1.46

Figure 6.1: *Dielectric constants and refractive indices of the various media interacting in our experiment. Molecular formula are given for organic solvents, accompanied by "(a)" for those with a benzene aromatic ring. All values were obtained from [132].*

To conclude this summary of the experimental conditions that were considered in order to carry out this study, let us summarize the various solvents and substrates that will be used and what we expect their influence to be. As explained earlier, toluene and dichloromethane seem to be good candidates for illustrating the effects of the dielectric constant on wetting and, hopefully, on

pattern formation. More generally, for the purpose of comparing several families of solvents, benzene-derivatives (i.e. toluene), chlorinated solvents (i.e. dichloromethane) and alkanes are taken into consideration, the latter for the range of viscosities, degree of volatility, and molecular steric volumes that they can span.

Table 6.1 lists the selected solvents. Values for the viscosities and surface tensions are not given because they are specifically taken similar for all solvents (however, they can be found in [132]). Keeping these values within a restricted range avoids the "interference" of several competing effects, possibly influencing nanoparticle self-organisation and pattern formation, as explained above. On the other hand, dielectric constants and refractive index are given since they will be necessary in Section 6.1.2 to estimate values of Hamaker constants.

In our system, the solvent constitutes the intermediary medium in the wetting problem (medium 3). Medium 1 is always air in our experiments. As for medium 2, the substrate, it is mostly of two different natures : either native-oxide terminated silicon or thermally-grown thick oxide terminated silicon. In the first case, the oxide layer is approximately 3nm thick, whereas it is 200nm thick in the second case. This will influence the wetting properties of the solvent on the substrate, as was demonstrated by Seemann *et al.* [64, 134] and will be highlighted again below. Media 1, 2 and 3 are listed in the table above. Note that other substrates were available for this study, such as hydrogen-terminated silicon (SiH). However, native and thick oxide terminated silicon substrates beneficiate from a reasonably large amount of literature, which is why there were prioritised for this experiment. Further studies - presently

carried out within our group - involve different types of substrates.

6.1.2 Patterns and Hamaker constants

Values of Hamaker contants can be deduced from the mathematical description of the solvent-substrate interactions given above. As explained above, in order to take into consideration only the influence of the solvent-substrate interaction, we have tried to choose experimental conditions so that (i) the solvent-nanoparticle interaction does not vary significantly (similar values of solvent viscosities), and (ii) the nature of the nanoparticles remains unchanged (C_8-thiol passivated nanoparticles) [133]. In a first approximation, we are thus expecting the Hamaker constant to reflect the wetting behaviour of each of the selected solvents on both types of substrates used.

In parallel, we conducted an initial experiment based on the considerations of the previous section (choice of solvents and substrates). Three goals can be defined : (i) test the relevance of Hamaker constant calculations in order to predict the wetting behaviour of a given-solvent-based nanoparticle solution on substrate, (ii) determine the effects of different solvents on the self-organisation of nanoparticles and hence the role of wetting in pattern formation, and (iii) identify one or several solvents of particular interest. For now, we shall concentrate on the first two points, the third being discussed in more detail in section 6.2.

Hamaker constants

The Hamaker constant describes the interaction of two media through a third one. Typically, for a thin liquid film on a surface, the liquid is said to be

wetting for negative values of the Hamaker constant, *non-wetting* for positive values. The Hamaker constant is calculated according to Eq. 6.1, derived from Bergström's description [131]. However, Eq. 6.1 is only valid for a 3-layer system. In our case, the substrate does not consist of a single material, but of two different materials : silicon oxide (3 or 200nm) and silicon, that we will note "SiO_2/Si" for "silicon oxide on silicon". We thus need to consider a 4-layer system in order to take into account the presence of the oxide layer and estimate the value of the Hamaker constant. This problem was already addressed by Seemann *et al.* while studying dewetting of polystyrene films from solid substrates [64, 134]. Seemann *et al.* proposed that the non-retarded van der Waals force for a 4-layer system, described in terms of the effective interface potential ϕ_{vdw} [64], should satisfy Eq. 6.5 :

$$\phi_{vdw}(h) = -\frac{A_{SiO_2}}{12\pi h^2} + \frac{A_{SiO_2} - A_{Si}}{12\pi(h+d)^2} \tag{6.5}$$

where, in our case, A_{SiO_2} and A_{Si} correspond to the Hamaker constants for the air-solvent-SiO_2 and air-solvent-Si systems respectively. h is the thickness of the liquid film, taken close to one nanoparticle height ($\sim$2nm), and d is the thickness of the silicon oxide layer (3 or 200nm). If the interaction of the *pseudo*-3-layer system air-solvent-SiO_2/Si is described by the global Hamaker constant A such that :

$$\phi_{vdw}(h) = -\frac{A}{12\pi h^2} \tag{6.6}$$

then we can write :

$$A = A_{SiO_2} - \frac{(A_{SiO_2} - A_{Si})h^2}{(h+d)^2} \tag{6.7}$$

A_{SiO_2} and A_{Si} can be calculated directly from the approach described in section 6.1.1, from which we deduce the value of A for our 4-layer systems. The results for each solvent on either native oxide (3nm) or thick oxide (200nm) terminated silicon are given in the tables below, Fig. 6.2 and Fig. 6.3.

Stack	A
Air / Hexane / SiO_2 3nm / Si	-0.2173eV
Air / Heptane / SiO_2 3nm / Si	-0.2155eV
Air / Nonane / SiO_2 3nm / Si	-0.2116eV
Air / Benzene / SiO_2 3nm / Si	-0.1763eV
Air / Toluene / SiO_2 3nm / Si	-0.1788eV
Air / Mesitylene / SiO_2 3nm / Si	-0.1772eV
Air / Dichloromethane / SiO_2 3nm / Si	-0.1999eV

Figure 6.2: *Hamaker constants for 4-layer systems air / solvent / native silicon oxide (3nm) / silicon. Algorithm adapted from [131] and [134].*

Stack	A
Air / Hexane / SiO_2 200nm / Si	-0.0636eV
Air / Heptane / SiO_2 200nm / Si	-0.0562eV
Air / Nonane / SiO_2 200nm / Si	-0.0433eV
Air / Benzene / SiO_2 200nm / Si	+0.0341eV
Air / Toluene / SiO_2 200nm / Si	+0.0295eV
Air / Mesitylene / SiO_2 200nm / Si	+0.0325eV
Air / Dichloromethane / SiO_2 200nm / Si	-0.0225eV

Figure 6.3: *Hamaker constants for 4-layer systems air / solvent / thick silicon oxide (200nm) / silicon. Algorithm adapted from [131] and [134].*

Detailed comments on these values will be made in the discussion section below. For now, note that our initial (and very strong) approximation for the calculation of Hamaker constants - not detailed here - was to consider that the

presence of native oxide did not influence the wetting properties of bare silicon significantly, and that on the contrary, 200nm of silicon oxide is sufficient to remove completely the contribution of the underlying silicon substrate. This approximation enabled the use of the 3-layer model to estimate Hamaker constants : the air / solvent / native silicon oxide / silicon stack was replaced by air / solvent / silicon, whereas the air / solvent / thick silicon oxide / silicon one became merely air / solvent / silicon oxide. This approximate calculation yielded results which were surprisingly convincing in terms of signs (positive and negative values of Hamaker constants were preserved), which would have led to the same conclusions as the more accurate 4-layer algorithm in terms of wetting or non-wetting solvents. However, the values obtained for the air / solvent / silicon system differed from the air / solvent / native silicon oxide / silicon by roughly an order of magnitude. The approximation concerning the negligible effect of native oxide has thus to be considered as erroneous (which we strongly suspected). On the other hand, the values obtained for the air / solvent / silicon oxide were practically equal to those obtained with the 4-layer model in the presence of a thick oxide. This proves that 200nm of oxide are indeed sufficient to "screen" the effect of the underlying bulk silicon in terms of van der Waals interactions and wetting properties.

Finally, the fact that for Hamaker constants of solvents on thick SiO_2, the values obtained have *absolute* values ranging from 0.0225 to 0.0636eV should not be overlooked. The value of kT - the thermal agitation - at room temperature is approximately 0.025eV, which is contained within this interval. However, our calculation highlights a clear trend with regard to relative wettabilities of solvents on thin and thick silicon oxide. The values in Tables 6.2

and 6.3 are separated by an order of magnitude, which demonstrates that the wettabilities on these two surfaces are significantly different for all solvents. Such a difference should have observable effects on pattern formation.

Experimental results

In Section 6.1.1, we identified the solvents that were pertinent for our experiment, namely some alkanes (hexane, heptane and nonane), benzene derivatives (benzene, toluene and mesitylene) and an halogenated solvent, dichloromethane. The two types of substrates on which to deposit the particles are native-oxide- and thick-oxide-terminated silicon (111) wafers. Once suspended in each of the chosen solvents, the nanoparticles (30μL of solution) were deposited on 1cm$\times$1cm substrates by spin-coating (4000rpm, 30 seconds) and the resulting morphologies were investigated by tapping mode AFM. The concentrations of the solutions were adjusted to offer a high enough, but sub-monolayer coverage of the surface. This finally led to a concentration of $\sim$0.7mg/mL. Experimental results are shown in Fig. 6.4 and 6.5. In both these figures, images (a), (b) and (c) show nanoparticles deposited from alkane-based solutions, (d), (e) and (f) from benzene-derivatives, and (g) from dichloromethane. Fig. 6.4 shows samples prepared on native (3nm) oxide terminated silicon substrates, whereas Fig. 6.5 presents the results obtained on thick (200nm) oxide terminated silicon substrates.

First of all, the formation of patterns such as cellular networks and spinodal decomposition-like domains (see Chapters 2 and 4) occurs within a *thin film* of liquid. This necessitates the uniform spreading of the liquid on the surface in the latest stage of drying, which implies a good wettability of the substrate

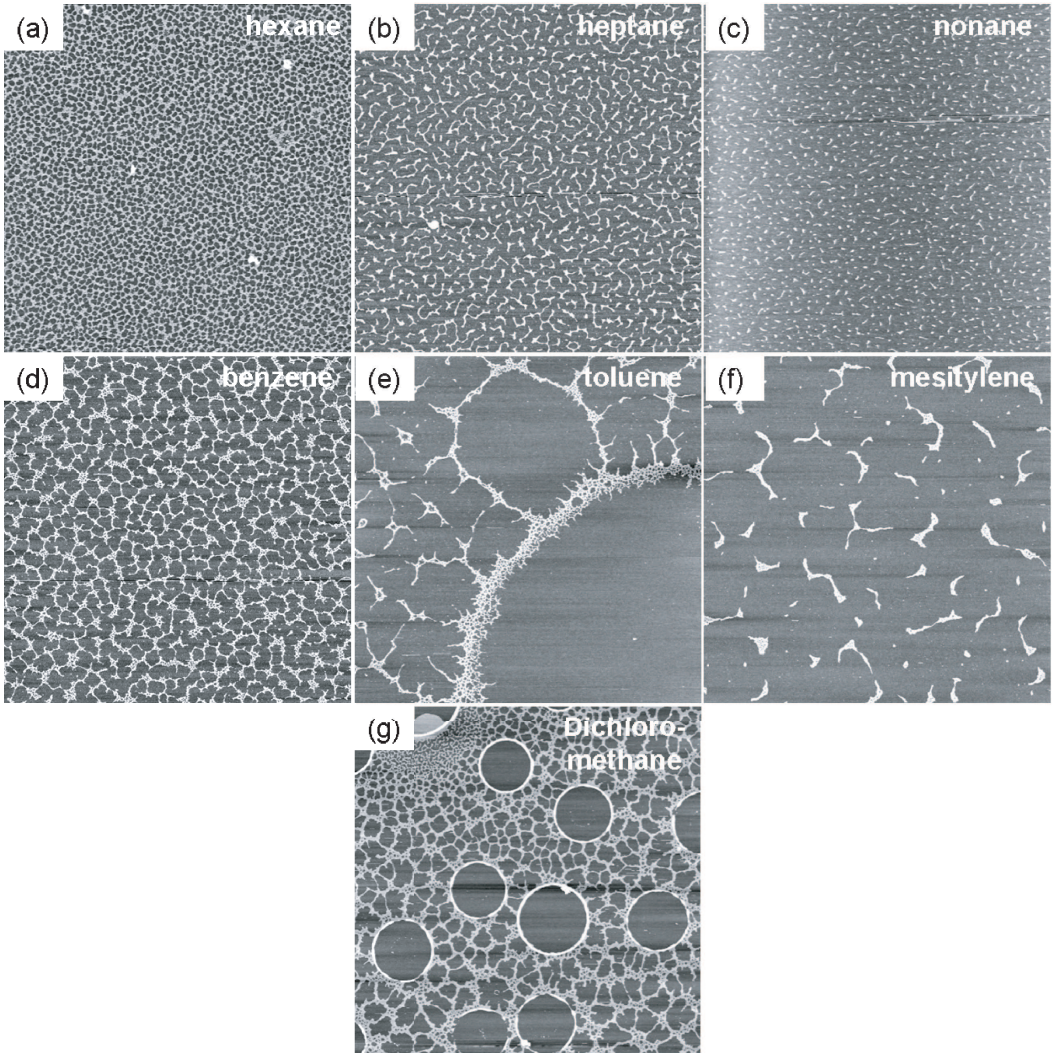

Figure 6.4: *TM-AFM images of 2nm C_8-thiol passivated Au nanoparticle arrangements on native-oxide (3nm) terminated silicon substrates following deposition by spin-coating of a (a) hexane-, (b) heptane-, (c) nonane-, (d) benzene-, (e) toluene-, (f) mesitylene-, (g) dichloromethane-based solution, of concentration ∼0.7mg/mL. Scans are 10μm×10μm in size.*

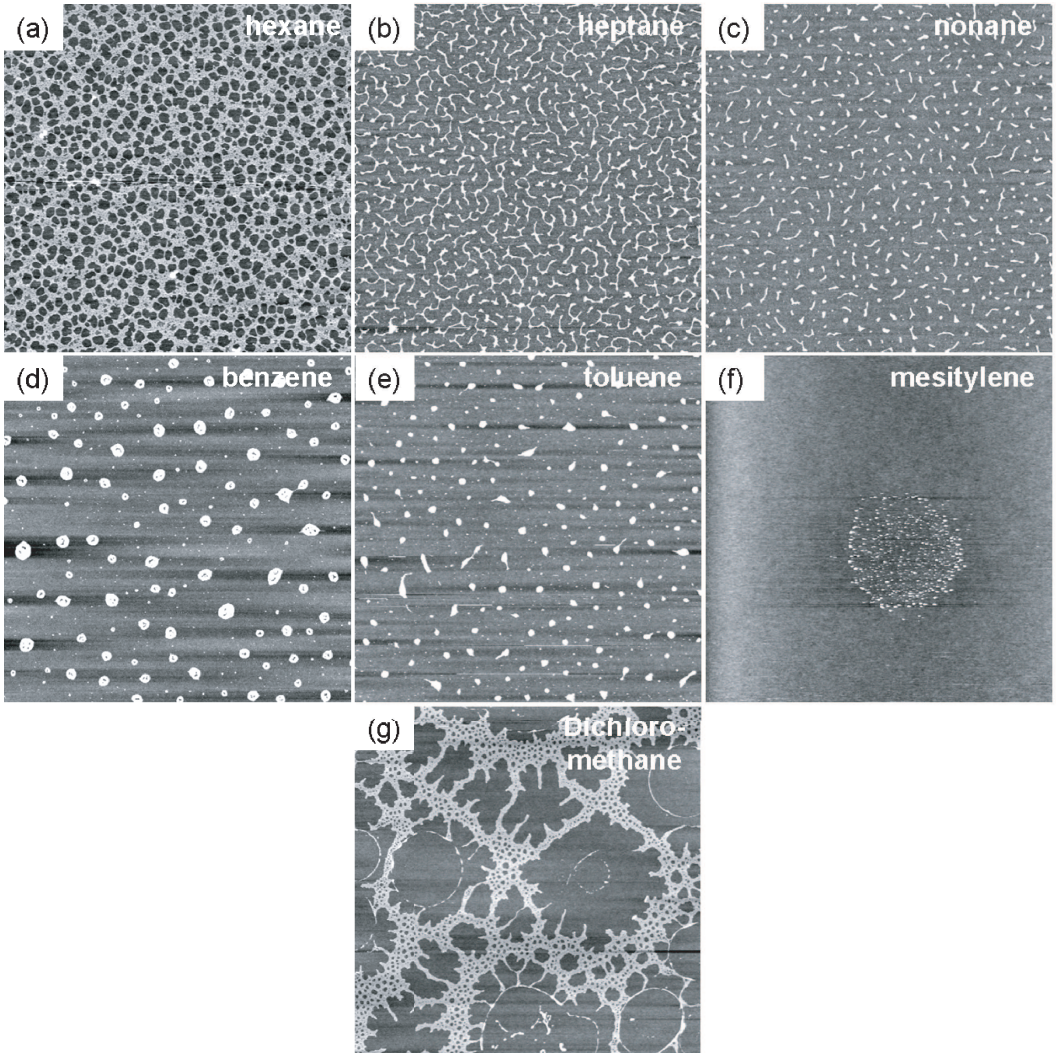

Figure 6.5: *TM-AFM images of 2nm C_8-thiol passivated Au nanoparticle arrangements on thermally grown thick oxide (200nm) terminated silicon substrates following deposition by spin-coating of a (a) hexane-, (b) heptane-, (c) nonane-, (d) benzene-, (e) toluene-, (f) mesitylene-, (g) dichloromethane-based solution, of concentration ∼0.7mg/mL. Scans are 10μm×10μm in size.*

by the solvent. In this case, the solvent is either "totally wetting" or at least "partially wetting". If the solvent is non-wetting, then it beads on the surface and does not allow the formation of uniform patterns over the surface. In that case, one ends up with droplets of solution, whose evaporation leaves isolated aggregates, or islands, of nanoparticles on the surface (Fig. 6.5(d), (e)). However, note that nanoparticle islands can also result from a different mechanism : the nucleation of several holes in a thin nanoparticle-liquid film can lead to the formation of islands within the regions separating adjacent expanding holes. As the expanding holes meet, nanoparticle islands are left on the surface, that are expected to be one nanoparticle high. In our case, the islands observed in Fig. 6.5(d) and (e) are more than a nanoparticle high, which suggests that solvent beading is responsible for their formation.

Figures 6.4(a)-(f) clearly show that all solvents wet native-oxide terminated silicon. This is indeed what we expected from the values of Hamaker constants calculated in the previous section (which were all negative on thin silicon oxide). The solutions generate various patterns depending on their physical characteristics (e.g. the strength of van der Waals interactions, i.e. the absolute value of the Hamaker constant , the solvent volatility, the ratio of nanoparticle diffusion and global evaporation rates, the ratio of nucleation and evaporation rates, etc.). The worm-like features of Fig. 6.4(b) and (c), obtained for the longest alkane molecules (heptane and nonane) suggest that pattern formation occurs following a spinodal-like dewetting process (that is, a very fast homogeneous process, see Section 2.2). Surprisingly, however, this is not the case for hexane, which forms cellular networks, just like benzene (Fig. 6.4(a) and (d) respectively). The very small difference in the absolute values

of Hamaker constants between the three alkanes did not incline us to foresee such a strong difference in the nature of the patterns formed.

The presence of secondary length scales within these cellular networks, particularly visible in the case of benzene, prompts the coexistence of several dewetting processes, including spinodal decomposition and Marangoni convection (refer to Section 2.3.2 and [21]). Patterns formed by particles deposited from toluene, mesitylene and dichloromethane (Fig. 6.4(e), (f) and (g) respectively) originate from dewetting mechanisms that are more difficult to identify. The first two seem somewhat "in between" the two processes described above (spinodal dewetting and Marangoni convection). The latter, however, is strikingly different from any type of pattern observed so far in our experiments. Dichloromethane-based solutions produce almost perfectly circular nanoparticle rings separated by smaller length scale networks (Fig. 6.4(g)). This will be discussed at length later : this primary series of experiments highlights the particularity of dichloromethane as a solvent compared to benzene-derivatives and alkanes, and we shall try to identify from where this difference has originated and what subsequent effects can be deduced in terms of pattern formation and tuning (section 6.2). Note for now that in terms of Hamaker constants, dichloromethane exhibits an intermediary value between benzene derivatives and alkanes. However, no clear correlation can be determined, in view of these experimental images, between the absolute value of the constant and the type of patterns formed. Although the cases of heptane, nonane, benzene and toluene seem to imply that worm-like structures are associated with large Hamaker constant absolute values (or very negative Hamaker constants), whereas cellular networks result from a smaller absolute value of the Hamaker

constant, the cases of hexane and mesitylene remain unsolved.

As opposed to Fig. 6.4, Fig. 6.5 illustrates several cases of apparently "non-wetting" solvents, namely for benzene- and toluene-based nanoparticle solutions (Fig. 6.5(d), (e)) on thick silicon oxide. In these cases, isolated islands of nanoparticles form, homogeneously distributed on the surface, and result from solvent beading. These islands are generally several nanoparticles high. This experimental observation is in perfect agreement with the estimation of the Hamaker constants of these solvents, which are positive on thick silicon oxide. On the contrary, alkane-based solutions all exhibit patterns similar to those observed on native silicon oxide (cellular networks for hexane, worm-like domains for heptane and nonane, Fig. 6.5(a), (b) and (c) respectively). Dichloromethane generates yet a different type of pattern : the nanoparticle rings from Fig. 6.4(g) seem to have "extended" to form large scale, poorly-developed fingering structures, surrounded once again by smaller scale networks. We do not to date understand what the formation of these very complex features implies in terms of dewetting mechanisms (although we strongly suspect that several mechanisms might be at play here). Mesitylene seems to be an intermediary stage between a wetting solvent and a non-wetting one. Indeed, nanoparticles do not form the easily recognisable regularly distributed islands resulting from a non-wetting liquid. Instead, they seem to gather into sparse one-nanoparticle thick aggregates, formed of small isolated nanoparticle islands, and randomly localised on the substrate (Fig. 6.5(f)). This aggregation may result from a self-organisational behaviour (involving at least a partially wetting solvent), but the very small quantity of nanoparticles present on the substrate suggests an instantaneous dewetting of the solvent at

the time of spin-coating, not leaving the time for nanoparticles to be adsorbed on the surface, which would imply that mesitylene is in fact non-wetting. This issue is partly answered by the calculation of the Hamaker constant, which implies that mesitylene is indeed a non-wetting solvent. However, the beading of the solvent and the deposition of the particles apparently do not follow the same mechanism as for benzene and toluene.

Finally, it is not clear, once again, what the absolute values of the Hamaker constants reveal about the wetting interaction and the selection of patterns. Indeed, although the absolute values are very different from Fig. 6.4 to Fig. 6.5, alkanes for example form the same types of patterns on each of the substrates.

Discussion : influence of wetting properties on pattern formation

Several comments have already been made concerning the relevance of Hamaker constants for determining the wetting properties of solvents and their influence on pattern formation. First, all the solutions behave, in terms of wettability, as predicted by the estimation of their Hamaker constants. This validates the use of this parameter to characterise the wetting behaviour of nanoparticle solutions, based only on their solvent and the substrate. However, in certain cases, and in particular in the cases where the absolute value of the constant is very small (as on thick oxide here), it seems that the wetting effects predicted by the sign of the constant can be overcome by increasing the nanoparticle concentration. This is for example the case of samples prepared in view of electrical measurements : it is possible to create arrays of nanoparticles exhibiting various degrees of structural disorder from toluene on thick

silicon oxide, for a high enough nanoparticle concentration, within a pair of gold electrodes, both by spin-coating [47,48] and via the ring-guided deposition technique (Chapter 4, Fig. 4.5) [92]. In these cases, experimental conditions seem to prevent the beading of the solvent and the formation of nanoparticle islands. In particular, the presence of gold contacts may contribute to trap some of the solvent locally, increasing the evaporation time locally. The role of the evaporation rate will be discussed again later (Section 6.2).

Secondly, our preliminary experiments did not allow us to establish a clear dependence between the selected patterns and the absolute value of the Hamaker constant. If A_{worm}, A_{cell} and A_{ring} are the Hamaker constants associated with the formation of worm-like domains, cellular networks and nanoparticle rings respectively, then some experimental results tend to indicate that : $A_{worm} < A_{ring} < A_{cell}$. Unfortunately, isolated cases such as those of hexane and mesitylene cast an uncertainty upon this proposition.

There remain several other points to be addressed, starting with the comparison of the Hamaker constants of toluene and dichloromethane based solutions, which do not yield the expected difference. In Section 6.1.1, we had chosen the latter because of its very high dielectric constant, which was about four times that of toluene, and the use of dichloromethane certainly leads to patterns radically different to those formed with other solvents. Whether the difference between dichloromethane and other solvents lies in its dielectric constant or in an other intrinsic / extrinsic property (volatility, viscosity, nanoparticle mobility, etc.) remains unclear and will be investigated in further experiments (Section 6.2).

Further experiments would also be required in order to identify the possi-

ble correlation between a given solvent and the type of patterns selected. The influence of solvent-substrate interactions was partly investigated here, but the exact contributions of the variations in solvent-nanoparticle and nanoparticle-substrate interactions - which were considered as constant here - need to be taken into consideration too. In addition, the solvent-substrate interaction can also be altered artificially, in particular by locally creating areas of different wetting properties on a substrate (such as hydrophilic oxide patterns on an hydrophobic H-terminated silicon substrate [47, 86]). The range of experimental parameters is extremely vast, which makes the problem of tuning pattern formation incredibly complex. However, the preliminary results presented here put forward a very simple way to predict the behaviour of a thin film of nanoparticle-solvent solution on a substrate, exclusively based on the calculation of van der Waals interactions, and prompts that there may exist a simple correlation between the wetting properties of a system and the resulting patterns that are formed.

6.2 Rings of nanoparticles

Section 6.1 explored the effects of various solvents on pattern formation and highlighted the very peculiar self-organising behaviour of gold nanoparticles when deposited from dichloromethane onto native silicon oxide : they form almost perfectly circular rings of nanoparticles, one to several nanoparticles high, of diameter in the micrometer range (Fig. 6.4(g)). What is somewhat surprising is that the Hamaker constant for dichloromethane on silicon is not significantly different from others (Fig. 6.2 and 6.3), as opposed

to what was expected due to the huge difference in dielectric constant compared to other solvents. Both in the presence of native oxide and thick oxide, dichloromethane exhibits Hamaker constants at intermediary values between alkanes and benzene-derivatives. However, the type of patterns formed by a dichloromethane-based solution differs strikingly from either worm-like domains (formed by alkanes) or cellular networks (formed mainly by benzene-derivatives). One peculiarity of dichloromethane is its very high volatility compared to the other solvents studied here. Indeed, at room temperature, there exists an order of magnitude difference between the vapor pressures of dichloromethane ($\sim$450mmHg) and toluene ($\sim$30mmHg), and at least a factor of 3 with those of the other solvents (e.g. benzene $\sim$100mmHg and hexane $\sim$150mmHg) [4].

The goal of this section is to identify the parameters that favour the formation of nanoparticle rings. A difference in volatility was highlighted that probably contributes to this phenomenon. The effects of other experiment-related parameters are investigated, such as nanoparticle concentration, deposition technique, nature of the substrate, but also how the modification of the particle interactions in solution influences the formation, shape and size of nanoparticle rings. Ultimately, we discuss the possible dewetting mechanisms associated with the formation and growth of such patterns.

6.2.1 Experiment : concentration, substrate and deposition technique

Nanoparticle rings have been observed experimentally by several groups in the past (Section 2.3.2 and [2,3,69]). These rings were usually two-dimensional and obtained by deposition and evaporation onto an amorphous carbon transmission electron microscope (TEM) grid. In our case, the observed nanoparticle rings are visually different from those seen by Ohara *et al.* [2] or Maillard *et al.* [3], and are typically more than one nanoparticle thick. No peculiar experimental conditions were required to obtain the samples of Fig. 6.4 and 6.5: an average concentration of 0.7mg/mL (but rings are also observed for 0.5 and 1mg/mL concentrations, for instance), an arbitrary quantity of deposited solution ($\sim$30μL), a conventional spin-coating process (4000rpm, 30s) and a standard cleaning process of the substrates (sonicated successively in ethyl lactate, acetone, methanol and isopropanol). The use of dichloromethane is a novel element in this experiment, toluene being a generally more widely used solvent. Most of our past experiments were carried out with toluene or hexane, which never resulted in the formation of nanoparticle rings. The solvent must thus play an important role in the occurrence of these patterns, as will be discussed below.

The experimental parameters that can be varied in this experiment are as follows : (i) the concentration of the solution, (ii) the nature of the substrate, (iii) the deposition technique (and, thus, the evaporation rate), (iv) the diffusion of nanoparticles in solution (by altering the interparticle and nanoparticle-solvent interactions, as we did in Chapter 5; see also Section 6.1.1). In view

of the preliminary data of Section 6.1.2, we shall keep native-oxide and thick-oxide-terminated silicon as the possible substrates. A parallel study is curently carried out within the group that involves the comparison between various substrates - and in particular *patterned* substrates, i.e. substrates whose wetting properties can be locally altered in a very controlled way [86] - and the subsequent effects on nanoparticle ring formation [128]. However, this study is out of the scope of this thesis and we shall concentrate on spontaneous nanoparticle ring formation on uniform oxide terminated silicon substrates for the time being.

Effects of concentration and substrate material

In the preliminary experiments of Section 6.1, the chosen concentration was about 0.7mg/mL. The initial solution concentration influences the nanoparticle coverage following deposition and can also alter the nature of the patterns formed, in particular on spin-coated samples [47,97]. Our objective is to establish, for each of the four parameters enumerated above, the most favourable value for the occurrence of nanoparticle rings. For this purpose, solutions of concentration 0.5mg/mL and 1mg/mL were tested on standard native oxide terminated silicon substrates. The resulting morphologies were imaged by AFM and some relevant examples are shown in Fig. 6.6. Fig. 6.6(a) was obtained for a low concentration (i.e. 0.5mg/mL) of the solution and shows badly-defined, irregular and mostly opened rings of particles, whereas Fig. 6.6(b) was obtained with a higher concentration (i.e. 1 mg/mL) and the nanoparticle rings, as well as the smaller networks that separate them, are much better defined.

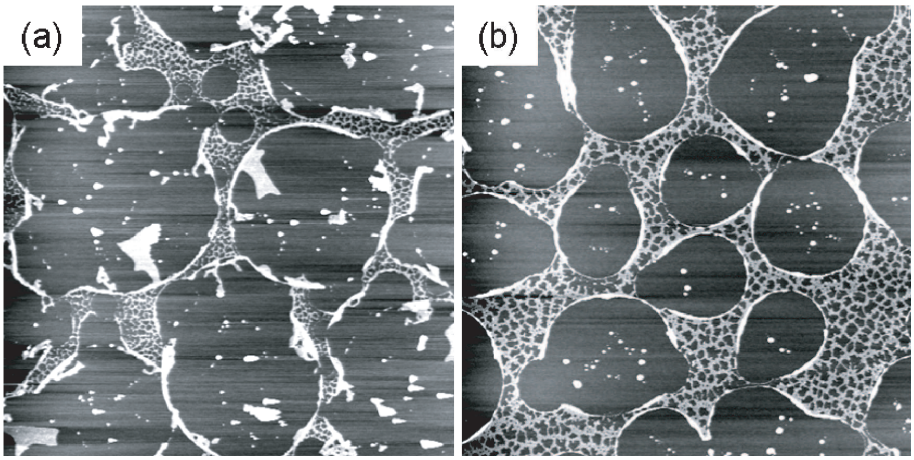

Figure 6.6: *10μm×10μm AFM scans of C_8-thiol passivated nanoparticles spin-coated from dichloromethane onto native oxide terminated silicon. The concentration of the solution is either (a) 0.5mg/mL or (b) 1mg/mL.*

In view of Fig. 6.6 and of corroborating results from other samples (C_{10}- and C_{12}-thiol passivated nanoparticles, and for thick SiO_2 terminated substrates as well), a value of concentration of 1mg/mL was selected for spin-coated samples. However, this concentration was reduced to 0.5mg/mL for tests carried out using the meniscus-driven deposition technique (see below). Indeed, whereas in spin-coated samples most of the solution is removed in the first stages of the deposition process (thus leaving very few of the initially deposited particles to be adsorbed on the surface), in the meniscus experiment, all the particles present in the drop of solution initially deposited are present on the surface following evaporation, which represents a considerable change of coverage as compared to spin-coated samples. As a result, 1mg/mL solutions led, in the case of a meniscus-driven evaporation, to nanoparticles piling up in multi-layers, which is why the concentration had to be divided by two.

Concerning the substrate, since dichloromethane wets both native oxide and thick oxide, not much difference would be expected from the change in

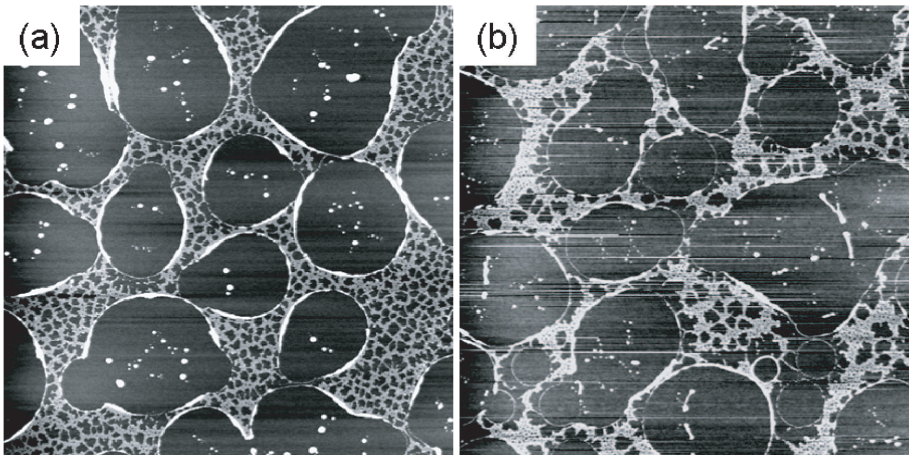

Figure 6.7: *10μm$\times$10μm AFM scans of nanoparticle arrangements resulting from the deposition by spin-coating of a 1mg/mL C_8-thiol passivated nanoparticle solution from dichloromethane onto (a) 3nm native oxide or (b) 200nm thick oxide terminated silicon.*

oxide thickness (as indeed illustrated by the two test samples shown in Fig. 6.7 - note however that differences exist, refer to Fig. 6.4(g) and 6.5(g)). Due to the very small value of the Hamaker constant of dichloromethane on thick SiO_2 (0.0225eV, see Fig. 6.3), it would be interesting to see if any major difference in wetting is observed as the other experimental conditions are varied across as broad a range as possible. This is the reason why both native and thick SiO_2 will be kept as substrates for the purpose of our experiment.

Spin-coating versus meniscus-driven evaporation

As we have seen in Section 6.1, the conditions of evaporation associated with the spin-coating process are adapted to the formation of nanoparticle rings. In order to identify the most favourable drying process for the occurrence of such patterns, we tried to deposit the same solution using a slow evaporation process, that is a meniscus-driven evaporation, such as in Chapter 4. We

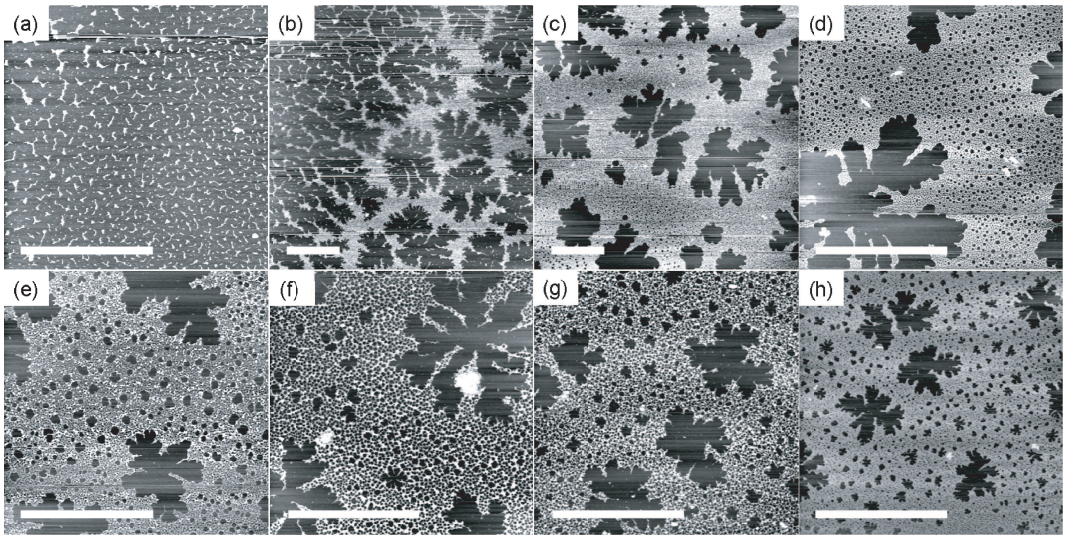

Figure 6.8: *AFM scans taken on a native-oxide terminated silicon substrate after deposition of 20μL of C_8-thiol passivated nanoparticles suspended in dichloromethane into a 5mm ID Teflon ring. Evaporation of the solvent takes place from (a) the centre towards (h) the edge of the sample. Images are taken at (a) 0mm, (b) 0.25mm, (c) 0.75mm, (d) 1mm, (e) 1.5mm, (f) 1.75mm, (g) 2.. and (h) 2.5mm from the centre of the sample. The scale bar represents 10μm.*

hoped that, in addition to obtaining nanoparticle rings, we would be able to observe the pattern evolution as the experimental parameters vary across the surface (the evaporation time and concentration vary from the centre towards the edge of the meniscus, see Chapter 4). Unfortunately, this is not the case, as illustrated in Fig. 6.8. These AFM images show the patterns formed on a native oxide terminated silicon substrate, onto which a solution of C_8-thiol passivated nanoparticles suspended in dichloromethane has been deposited using the meniscus technique.

From isolated worm-like domains in the centre of the sample (Fig. 6.8(a)), corresponding to a very fast evaporation (particularly in the case of dichloromethane, which is very volatile), the patterns then evolve in elongated

fingering structures (Fig. 6.8(b)) and then radial, isotropic fingering structures (Fig. 6.8(b)-(h)), until the edge of the sample. Thus, there is no clear evolution of the nature of the patterns across the surface. More importantly, no nanoparticle rings are formed. Several test samples such as the one shown in Fig. 6.8 were prepared, with various substrates, solution concentrations, types of nanoparticles and sizes of Teflon rings, and none of them exhibited nanoparticle rings such as those observed on spin-coated samples. This - very reproducible - experimental result implies that *for nanoparticle rings to form, one needs a very rapid solvent evaporation.* For this reason, the meniscus deposition technique was considered ill-suited for the study presented here and in the rest of this chapter, only spin-coated samples will be taken into consideration (the meniscus technique is more adapted to the study of different types of patterns, such as those described in Chapter 5). Furthermore, this is coherent with the assumption we made that the very high vapor pressure of dichloromethane as compared to other solvents - hence its very high volatility - plays a role in the occurrence of nanoparticle rings.

6.2.2 Interparticle interactions : effect of thiol chain length

Following these preliminary considerations, samples were prepared by spin-coating a dichloromethane-based solution of particles, of concentration 1mg/mL. Toluene-based solutions were also used for preparing reference samples. Indeed, since our group has been working with toluene solutions for several years [21, 47, 48, 81, 92, 97, 106, 135], we have acquired a good understanding of

pattern formation mechanisms in such systems, which is bound to be valuable for understanding the processes at play here. Samples are prepared in a clean room environment, by spin-coating a 30μL drop of nanoparticle solution onto a 1cm×1cm substrate, rotated at 4000rpm for 30 seconds (which is sufficient for a complete evaporation of the solvent). The sample surfaces were then investigated by AFM. A close inspection of each sample showed that the morphology was similar on the majority of the sample surface (excluding edges, see section 3.2).

We have investigated in the previous section the role of the wetting of the solvent on pattern formation, that is the influence of the solvent-substrate interaction. We are now interested in the effect of the nanoparticle-nanoparticle interaction on the formation of patterns : what happens if we modify this interaction ? The mobility of nanoparticles around each other will be altered, resulting in a modification of the diffusion coefficients of particles [133], which we expect to have an effect on pattern formation, just as in the case of fingering structures presented in Chapter 5. Once again, we modify this interaction by varying the length of the passivating thiol molecules of the particles, from eight to twelve carbons (we reiterate that this is achieved by simply changing the nature of the thiol molecule in the synthesis process, without altering the procedure itself, Section 3.1). According to Motte and Pileni [124], although longer thiol chains increase the interparticle distance, they provide a higher interdigitation, which induces a strong packing of the particles (i.e. impede the free motion of nanoparticles in the vicinity of each other). Experimental results are given in Fig. 6.9 for dichloromethane-based solutions, and in Fig. 6.10 for toluene-based solutions.

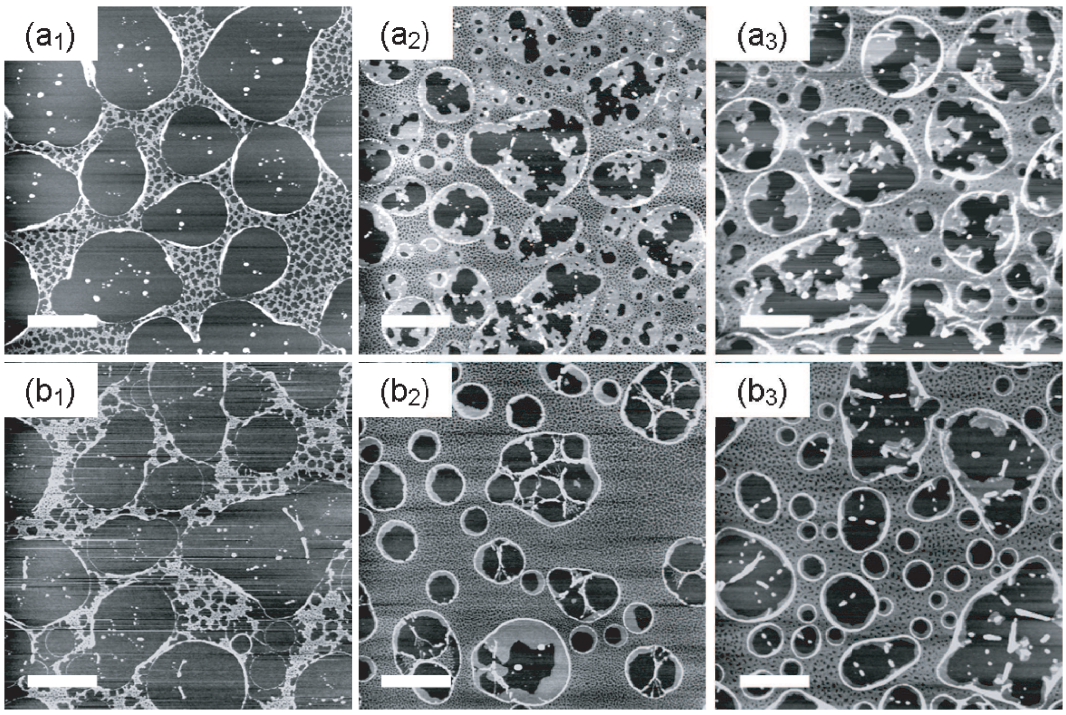

Figure 6.9: *AFM images of nanoparticles deposited from dichloromethane onto (a_1–a_3) native oxide terminated silicon or (b_1–b_3) thick oxide terminated silicon, via spin-coating (at 4000rpm, during 30s). (a_1) and (b_1) are obtained with C_8-thiol passivated particles, (a_2) and (b2) with C_{10}-thiol passivated ones, and (a_3) and (b_3) with C_{12}-thiol passivated ones. The scale bars represent 2μm.*

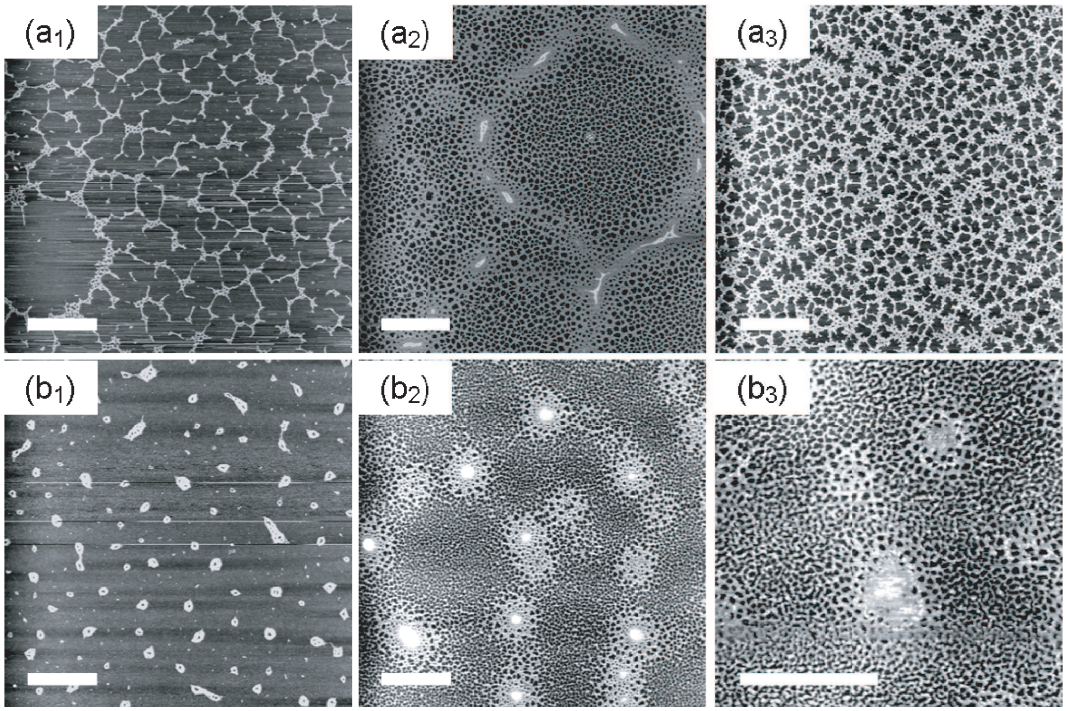

Figure 6.10: *AFM images of nanoparticles deposited from toluene onto (a_1–a_3) native oxide terminated silicon or (b_1–b_3) thick oxide terminated silicon, via spin-coating (at 4000rpm, during 30s). (a_1) and (b_1) are obtained with C_8-thiol passivated particles, (a_2) and (b2) with C_{10}-thiol passivated ones, and (a_3) and (b_3) with C_{12}-thiol passivated ones. The scale bars represent 2μm.*

The samples prepared with dichloromethane-based solutions (Fig. 6.9) all exhibit nanoparticle "rings" (or groups of rings that have merged together), be it on native silicon oxide (3nm) or on thick silicon oxide (200nm). The variation of the thiol chain length thus does not seem to either counteract the wetting behaviour of dichloromethane (values of the Hamaker constants are -0.1999eV and -0.0225eV for native and thick oxides respectively, as calculated in section 6.1.2) or impede ring formation. Noticeably, the effect of the substrate on pattern selection is not crucial : the images of Fig. 6.9(a_1), (a_2) and (a_3), taken respectively for C_8-, C_{10}- and C_{12}-thiol passivated particles on native oxide, do not differ radically from the images in Fig. 6.9(b_1), (b_2) and (b_3), showing similar nanoparticles on thick oxide.

The effect of the thiol chain length, however, is more pronounced. For C_8-thiol passivated nanoparticles, micrometre-sized rings form that are either isolated or a gathering of several rings that have coalesced with each other (Fig. 6.9(a_1) and (b_1)). This is clearly indicated by the small particle aggregates present in the centre of the features, which are almost certainly remains of the rims of the coalescing rings. These rings (or combinations of rings) are surrounded by smaller scale networks, either polygonal [81] - on native oxide - or ramified (i.e. fingering) networks - on thick oxide. Note that the latter form mainly in the vicinity of the rings, which offers a connection with the image of Fig. 6.5(g), for which a lower concentration of particles (0.7mg/mL) led to the disappearance of the rings in favour of poorly-defined large scale fingering structures.

C_{10}-thiol passivated particles form the arrangements of Fig. 6.9(a_2) and (b_2). The main difference with the previous case is that the rings and en-

sembles of rings are not empty. One-nanoparticle-thick layers start forming on the inside of the rings and possibly "grow" from their periphery. The size distribution of the rings is shown for each of the samples in Fig. 6.11. The distribution is noticeably broader for C_{10}-thiol passivated particles than for the C_8 case : ring diameters range from less than 300nm up to 4.5μm on native oxide, against 2 to 4μm in the C_8 case. The proportion of small size rings (less than 1μm) is also very important in the C_{10} case (above 40%), whereas it is very small in the C_8 case (0% on native oxide, 20% on thick oxide). The height of the rings, on the other hand, is similar to that in the C_8 case (most rings are 1 to 3 nanoparticles high, with an irregular circumference), and will be discussed again later (see next section, Fig. 6.14, 6.15 and 6.16). Finally, the length scale of the networks between the rings has decreased in the C_{10} case compared to the C_8 one, and is now limited to regularly distributed polygonal cellular networks. No fingering structures are observed on the thick oxide sample, as opposed to the previous case. The number of rings observed is higher in the C_{10} case than in the C_8 case, which is consistent with the presence of more numerous small rings.

C_{12}-thiol passivated particles exhibit a behaviour that is very similar to that of C_{10}-thiol passivated particles (Fig. 6.9(a_3) and (b_3)). The ensembles of rings are also very variable in size (300nm to 5μm, Fig. 6.11(a_3) and (b_3)), and the particle monolayers within the rings are present as in the C_{10} case. The ring height is similar to other cases and low (2 to 3 nanoparticles). The differences observed from one substrate to the other are the same differences listed in the C_{10} case above. Although the tendency initiated in the C_{10} case compared to the C_8 case is preserved, it does not evolve much further with the

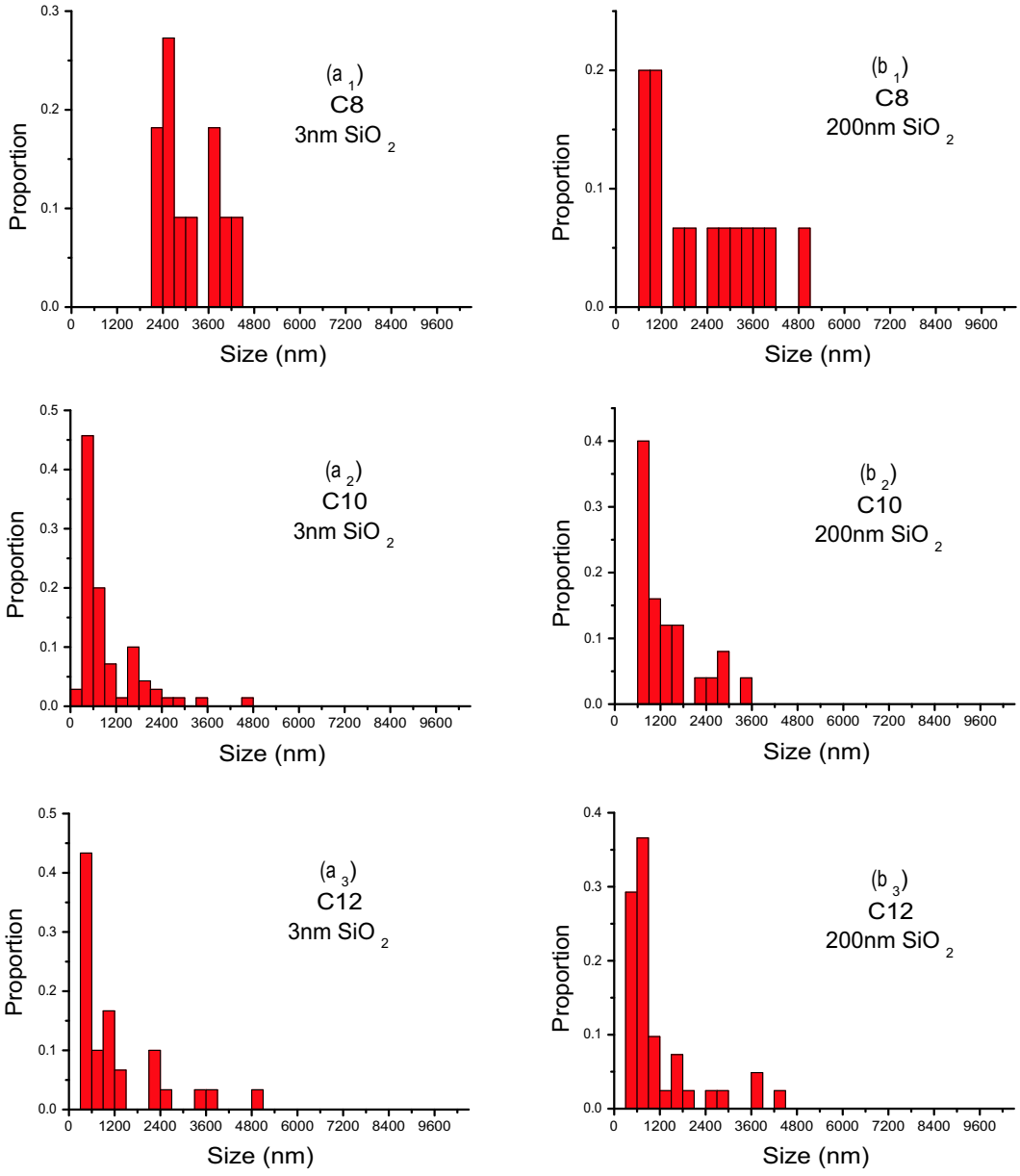

Figure 6.11: *Histograms showing the size distributions of nanoparticle rings for each chain length (C_8 for (a_1) and (b_1), C_{10} for (a_2) and (b_2), C_{12} for (a_3) and (b_3)) and substrate (3nm native silicon oxide or 200nm thick silicon oxide) for dichloromethane-based solutions. Each histogram is plotted according to the statistics provided by the corresponding AFM images in Fig. 6.9.*

use of C_{12}-thiol passivated particles. Propositions for the mechanisms at play in the formation and evolution of these ring-like structures will be discussed in section 6.2.4.

The reference samples prepared with toluene-based solutions are particularly interesting here (Fig. 6.10). First, they show that nanoparticle rings are not solely the result of the deposition process or solution concentration : as a matter of fact, they apparently cannot be formed for a different solvent than dichloromethane (see also experimental results from section 6.1.1). Second, as opposed to dichloromethane, arrangements originating from toluene-based solutions are much more sensitive to the length of the thiol carbon chain. Indeed, although C_8-thiol passivated particles reproduce exactly the configuration observed in section 6.1 (Fig. 6.10(a_1) and (a_2)) - in particular, the isolated nanoparticle islands on thick silicon oxide due to the non-wetting nature of toluene - it is not the case for C_{10}- and C_{12}-thiol passivated particles. In the latter cases, nanoparticles adopt self-organised configurations comprising several networks with different length scales (Fig. 6.10(b_2)-(b_3)). The coverage on the surface is very high, which contradicts what we would expect for a non-wetting solvent. It thus seems that the increase in the thiol chain length somehow counteracts the behaviour expected from the contribution of wetting properties only. Again, this will be discussed further in Section 6.2.4.

6.2.3 Nanoparticle-solvent interactions : effect of excess thiol

In the previous section, the thiol chain length was varied in order to modify the interparticle interaction and diffusion and to assess the consequences on pattern formation. In this section, we are interested in the diffusion (or "mobility") of the particles in the solvent. As stated earlier (Section 6.1.1), the diffusion coefficient of the solute is inversely proportional to the viscosity of the solution [133]. The previous experiment involved the use of several chain lengths of the passivating thiol molecules in order to increase the degree of interdigitation of adjacent particles. This will increase the overall viscosity of the solution (by decreasing the nanoparticle diffusion rate). However, the effect, as we have seen, is not striking : differences in pattern evolution have been noted, but the formation of nanoparticle rings was not impeded.

In order to dramatically alter the viscosity of the solution, we added an excess of non-volatile molecules to the solvent. Thiol molecules are perfect candidates, since they are not volatile and will not induce any contamination of the solution (as stated in the past by Lin *et al.* [74] and as already observed in the experiments of Chapter 5). As a result, an excess of 0.1% thiol by volume is added to each of the solutions prior to deposition. The added thiol molecules correspond to those used for the passivation of the particles, that is respectively C_8-thiol, C_{10}-thiol and C_{12}-thiol for our three solutions. Other than the addition of excess thiol, the experimental conditions are identical to those of the previous experiment (case with no excess thiol, Fig. 6.9 and 6.10). Results for dichloromethane-based solutions are presented in Fig. 6.12.

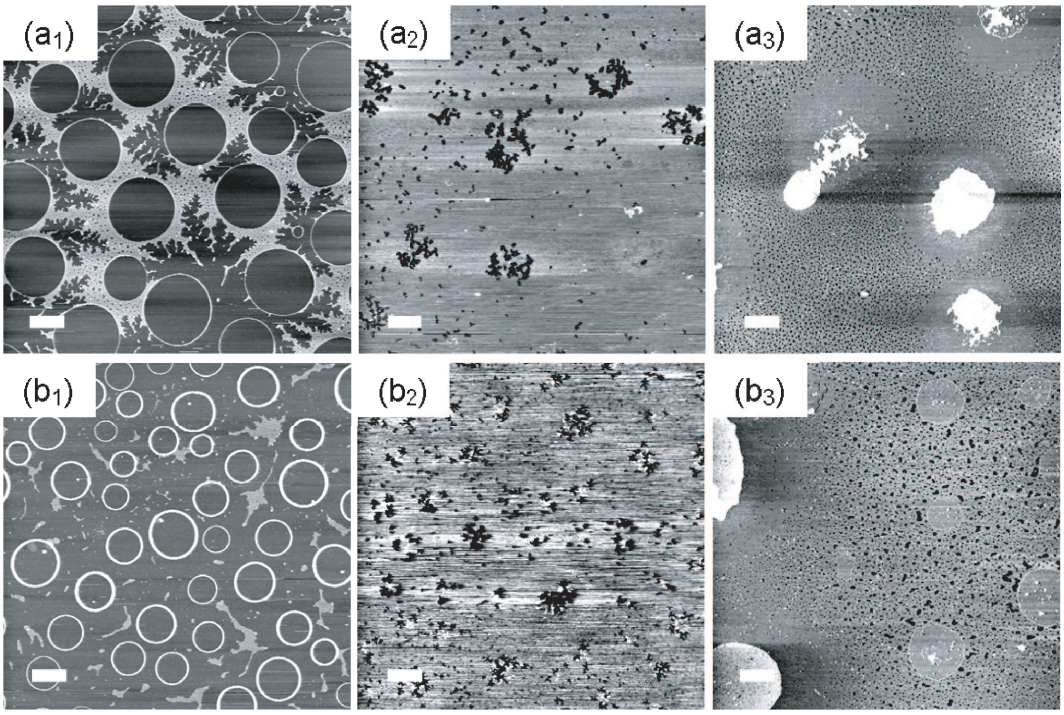

Figure 6.12: *AFM images of nanoparticles deposited from a dichloromethane-based solution containing 0.1% excess thiol by volume, onto (a_1–a_3) native oxide terminated silicon or (b_1–b_3) thick oxide terminated silicon, via spin-coating (at 4000rpm, during 30s). (a_1) and (b_1) are obtained with C_8-thiol passivated particles, (a_2) and (b2) with C_{10}-thiol passivated ones, and (a_3) and (b_3) with C_{12}-thiol passivated ones. The scale bars represent 2μm.*

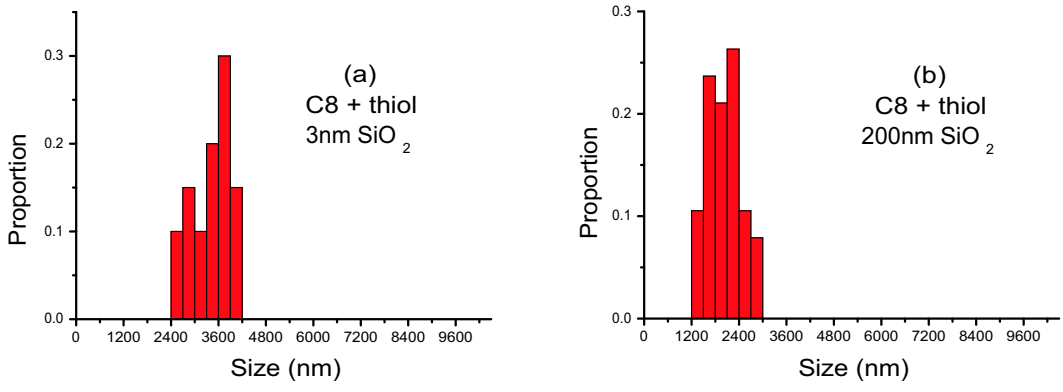

Figure 6.13: *Histograms showing the size distributions of nanoparticle rings for a dichloromethane-based solution of C_8-thiol passivated nanoparticles containing an excess of 0.1% C_8-thiol by volume, deposited on either (a) 3nm of native silicon oxide or (b) 200nm of thick silicon oxide. Each histogram is plotted according to the statistics of the corresponding AFM images in Fig. 6.12.*

For C_8-thiol passivated nanoparticles, rings still form as in the previous case (Fig. 6.12(a_1) and (b_1)). It is not the case for C_{10}-thiol passivated (Fig. 6.12(a_2) and (b_2)) and C_{12}-thiol passivated (Fig. 6.12(a_3) and (b_3)) particles. However, many differences can be noted compared to the previous data. First, in the presence of excess thiol, the substrate has a strong influence on the shape of the nanoparticle rings and on the surrounding networks - whenever they occur (C_8 case). On one hand, excess thiol seems to influence the shape of the rings, which are circular to an even higher degree than before, and do not coalesce as in the previous case (Fig. 6.12(a_1) and (b_1)). As a result, the size distribution is very narrow (2.5 to 4.1μm on native oxide, 1.3 to 2.8 μm on thick oxide, Fig. 6.13), with a high mean value (around 3.6 and 2 μm respectively). Noticeably, the rings are about twice as large on native oxide than on thick oxide. The substrate also influences both the height of the rings and the surrounding networks, which completely disappear on thick oxide (Fig. 6.12(b_1)). Concerning the height, it is difficult to estimate the average height of the rings from sections of AFM images, in particular because most rings are not regular along their circumference. A sample of ring heights (from 50 to 80 measurements depending on the images) measured along the scan lines of our AFM images yields the values represented in the histograms of Fig. 6.14. The range of heights for each sample is summarized in Table 6.15.

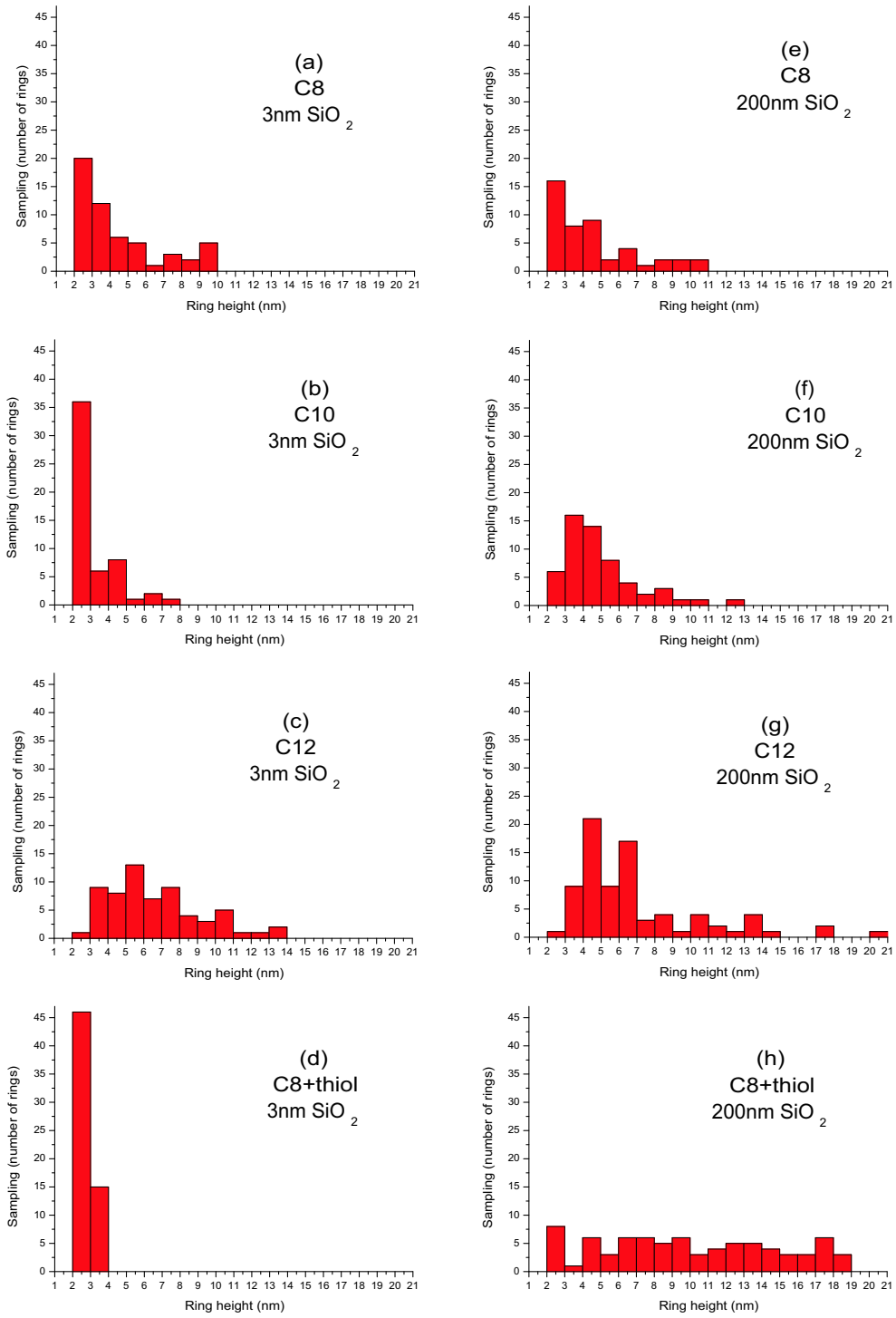

Figure 6.14: *Histograms of the nanoparticle ring height distributions (in nm) on samples prepared with a (a)-(e) C_8, (b)-(f) C_{10}, (c)-(g) C_{12} or (d)-(h) C_8+0.1% thiol dichloromethane-based solution on both (a-d) thin (3nm) and (e-h) thick (200nm) oxide terminated silicon.*

Sample	range of heights (nm)	range of heights (nanoparticles)	average height (nm)	standard deviation (nm)
C8 oxide 3nm	2-10	1-5	4.3	2.4
C8 oxide 200nm	2-10	1-5	4.5	2.4
C10 oxide 3nm	2-8	1-4	3	1.4
C10 oxide 200nm	2-12	1-6	4.9	2
C12 oxide 3nm	2-14	1-7	6.6	2.5
C12 oxide 200nm	2-20	1-10	7	3.7
C8+thiol oxide 3nm	2-4	1-2	2.8	0.4
C8+thiol oxide 200nm	2-18	1-9	10	4.9

Figure 6.15: *Table of the ranges of nanoparticle ring heights (in nm) on samples prepared with a C_8, C_{10}, C_{12} or C_8+0.1% thiol solution on both thin (3nm) and thick (200nm) oxide terminated silicon. The equivalent values in terms of number of nanoparticles are approximated using a average single nanoparticle height of 2nm. Averages and standard deviations are also calculated.*

In addition, 3D reconstructions of these images give a clear illustration of the differences in nanoparticle ring heights, as shown in Fig. 6.16. This figure puts side by side all the different samples that exhibit rings, which are the C_8, C_{10} and C_{12} cases of the previous section, and the "C_8+thiol" case of this section. In this figure, white regions represent aggregates of more than one nanoparticle in height.

This analysis shows that on thick oxide (Fig. 6.16(e)-(h)), rings are generally as high as or higher than their equivalents on native oxide (Fig. 6.16(a)-(d)). The case with excess thiol emphasizes this difference, since rings go from a single nanoparticle (∼2nm) in height on native oxide (on average), up to nine

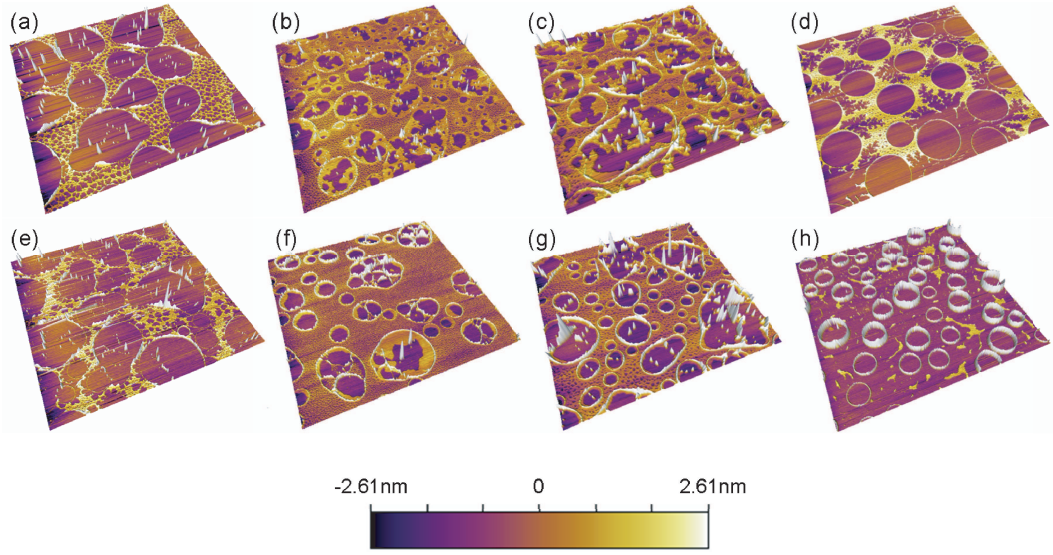

Figure 6.16: *3D reconstructions of nanoparticle rings shown in the AFM images of Fig. 6.9 and 6.12, that illustrate the variations in height distributions depending on the thiol chain length, the substrate and the presence of excess thiol. (a,e) were obtained with C_8-thiol passivated particles, (b,f) with C_{10} particles, (c,g) with C_{12} particles and (d,h) with C_8 particles in the presence of 0.1% of thiol by volume. The substrate is native silicon oxide (3nm) for (a-d), and thick (200nm) silicon oxide for (e-h). The right extremity of the color bar corresponds approximately to the height of one nanoparticle on the surface (∼2nm). Anything above this height appears in white on the 3D images. Images are 10µm×10µm in size, apart from (d) and (h) which are 20µm×20µm.*

nanoparticles high (∼18nm) on thick oxide (with rings spanning uniformly all ranges of heights between 2 and 18nm). The reasons for this significant difference in height will be tentatively explained in the discussion below (Section 6.2.4).

Aside from the rings, the substrate and the presence of thiol also influence the formation of the surrounding networks. While the networks have completely disappeared on thick oxide, those that form on native oxide exhibit two distinct types of patterns, in a much more pronounced manner than in the previous case (without thiol) : the cellular networks are very dense, with much

smaller voids than previously, and the fingering structures are much better developed and spread over microns in size (Fig. 6.12(a_1)). Similarly to what was observed before, fingering structures seem to form preferably near the rims of the nanoparticle rings (e.g. Fig. 6.5(g)). On thick oxide, on the contrary, no network is observed between the rings, and the coverage is very low in terms of covered *area*. However, this low coverage must be partly compensated, in terms of quantity of absorbed nanoparticles, by the dramatic increase of the height - and possibly width - of the rings between Fig. 6.16(d) and (h).

Finally, nanoparticle rings do not form for longer thiol chain lengths. The images in Fig. 6.12(a_2), (b_2), (a_3) and (b_3) illustrate cases where the viscosity of the solution is maximum (slow diffusion due to long chain length and overall viscosity increased by the presence of non-volatile thiol molecules free in solution). This corresponds to the lowest values of diffusion coefficients, which means that *the formation of nanoparticle rings necessitates high diffusion coefficients*. Note also that the effect of the substrate, which is unquestionable for C_8-thiol passivated particles, is not so obvious in the C_{10} and C_{12} cases. C_{10}-thiol passivated particles form very dense, close-packed layers with a small density of holes, whereas C_{12}-thiol passivated particles form large aggregates, surrounded by void-ridden dense layers of particles. On thick oxide, the latter also tend to form patterns which, to a certain extent, exhibit a circular geometry (Fig. 6.12(b_3)). However, these patterns look fundamentally different from earlier rings of nanoparticles and we believe they are of a different nature altogether, which places them out of the scope of this discussion.

Before we move on to discussing the above results, the associated experimental conditions and possible underlying pattern formation mechanisms, note

that reference samples were also prepared from toluene-based solutions (containing an excess of thiol), as for the previous experiment. In the presence of excess thiol, toluene seems to dewet systematically from the tested surfaces, leading to the formation of nanoparticle aggregates on all samples, independently of the thiol chain length. Thus, as in the case of Fig. 6.12(b_1) where all the secondary networks had disappeared, the presence of excess thiol seems to greatly influence the wettability of the substrate by the solvent. Unfortunately, estimating the value of the Hamaker constant for this system, where the solvent is replaced by a combination of solvent + excess thiol, is not straightforward. However, this is an important qualitative consideration that we shall keep in mind in the following discussion.

6.2.4 Discussion

Summary of the experimental results

We have exploited a wide range of experimental parameters and techniques in order to influence the formation of nanoparticle rings. A brief summary of our results is as follows :

(i) Nanoparticle rings are observed only for dichloromethane-based nanoparticle solutions, independent of the nanoparticle concentration and nature of the substrate (thin or thick oxide). They form on spin-coated samples exclusively, where the evaporation rate of the solvent is maximum. They do not form in any case as a result of a toluene-based solution deposition.

(ii) In the absence of excess thiol, nanoparticle rings form for all the thiol chain lengths that were tested (8, 10 and 12 carbon atoms). Once again, the

nature of the substrate does not appear to impede ring formation, or influence substantially the shape, size or number of nanoparticle rings. On the other hand, the increase in the thiol chain length is accompanied by a broader size distribution of the "ring-like" structures. In the case of C_8 particles, the size of the rings lies within a 2 to 4μm interval, whereas it spans from 300nm to 5μm in the C_{10} and C_{12} cases. The latter exhibit an important number of small sized rings (less than 1μm), which do not develop but coalesce into larger structures. One-nanoparticle-thick layers also form within the rings of C_{10} and C_{12} nanoparticles, which were not present in C_8 nanoparticle assemblies. Finally, the characteristic dimension of the nanoparticle networks that stand between adjacent rings decreases as the thiol chain length increases, although the nature of the network (cellular) is not significantly altered.

(iii) In the presence of excess thiol, nanoparticle rings only form for a solution of C_8 particles. Rings are no longer observed for the C_{10} and C_{12} cases. This observation is valid both on thin and thick oxide substrates. Nevertheless, whenever rings form, this time the substrate seems to have a strong influence on both the ring shape, size and height, but also on the interconnecting networks. Nanoparticle rings are on average twice as large on native oxide as on thick oxide and they do not coalesce as they did in the absence of excess thiol. Interconnecting networks exhibit two types of distinct patterns on native oxide, respectively cellular networks and fingering structures - the latter forming essentially in the vicinity of the nanoparticle ring edges. However, neither type is preserved on thick oxide : the networks do not form on that type of substrate.

(iv) The nanoparticle ring height is influenced mostly by the nature of the

underlying substrate. Although on every sample the ring height spans a range of values, the maximum height is not significantly influenced by the thiol chain length : on native oxide, the maximum height is comprised between 4 and 7 nanoparticles for C_8, C_{10} and C_{12} solutions (following a non linear variation). However, for these three solutions, the maximum ring height is increased in the presence of a thick oxide terminated substrate (from 5 to 10 nanoparticle high depending on the thiol chain length). The addition of excess thiol seems to have two main effects. First, it narrows the size distribution on native oxide (and lowers the average value down to $\sim$1 nanoparticle in height) but not on thick oxide. Secondly, it accentuates the effect of the change of substrate : the maximum ring height is increased by a factor of 4.5, from 2 to 9 nanoparticles.

Conclusions

The four points highlighted above suggest a number of correlations between the nanoparticle ring formation and growth and physical parameters associated with the various experimental conditions. To conclude this chapter, we attempt to deduce from this set of experimental results some preliminary conclusions concerning the mechanism of formation of nanoparticle rings.

(i) Volatility : As prompted in the introduction of this section, the difference of vapor pressures between toluene (30mmHg) and dichloromethane (450mmHg) at room temperature plays an important role in the occurrence of nanoparticle rings. Our first conclusion is that *a very fast evaporation - i.e a very volatile solvent - is required for the formation of nanoparticle rings.* This is also consistent with the fact that nanoparticle rings only form on spin-coated samples, not on samples prepared with the meniscus techniques of Chapter 4,

where the evaporation is slow.

(ii) Ratio of mobility to evaporation rate : This first conclusion leads us to a comparison between the evaporation rate of the solvent and the nanoparticle diffusion rate. Indeed, we noticed that for the longest chains and in the presence of excess thiol, nanoparticle rings could not form. These cases correspond to the configurations where the viscosity of the solution is maximum, i.e. where the nanoparticle diffusion rate is the lowest. *For the formation of nanoparticle rings to occur, we thus need a high diffusion rate of the nanoparticles.* In such conditions, the very high solvent evaporation rate very much dominates over the diffusion of the nanoparticles. This is reminiscent of Yosef and Rabani's assumption [82], as explained in Chapter 5, concerning the ratio of global evaporation rate to the evaporation rate at the rim of a nucleated hole.

(iii) Formation of interconnecting networks : The high diffusion rate of the particles is influenced both by the use of long thiol chains and by the presence of free excess thiol molecules in solution. Since the formation of rings is associated with a high diffusion rate, at this early stage of the evaporation (when the rings form), the nanoparticle must be able to track the dewetting front. This suggests that the initial holes form in a relatively thick solvent film. Once the film reaches a thickness of approximately one nanoparticle diameter, the "secondary" networks form. At that stage, the higher concentration of nanoparticles and possible excess thiol molecules reduce the mobility of the particles. These conditions correspond to those described in Chapter 5 as ideal for the formation of fingering structures. This in particular helps to understand the formation of fingering structures within the interconnecting

networks in the presence of excess thiol. The fact that these networks are eliminated on a thick oxide-terminated substrate, however, is more likely to be related to a modification of the wetting properties of the solvent by the presence of excess thiol (this assumption is based upon the observations of Chapter 4 and supported by the supplementary material videos of [92]).

A number of open questions remain in explaining the mechanisms of formation of these nanoparticle rings, and in particular concerning the coalescence of adjacent rings and the nanoparticle monolayers forming inside some of the rings (Fig. 6.9(a_2), (b_2), (a_3) and (b_3)). However, we think it likely that the dynamics of the ring and network formation is close to that described in Chapter 5 and by Yosef and Rabani [82], and involves several time and length scales, and the coexistence of a thin and a thick film of solvent. The correlation between ring formation and the ratio of nanoparticle mobility to solvent evaporation seems clear in view of experimental results. The effects of various experimental parameters (nature of the substrate, thiol chain length, excess thiol) on ring shape, size and height can also be deduced with a high enough degree of confidence. This study thus (i) highlights the possibility of reproducibly obtaining a certain type of pattern, namely nanoparticle rings, via the tuning of wetting properties, (ii) proposes experimental solutions in order to control the formation, shape, size, number and height of rings, and (iii) identifies some of the necessary conditions and mechanisms that underly their occurrence. Further investigation comprises the combination of nanoparticle ring forming solutions with nanolithographic techniques in order to guide ring formation on a surface (see supplementary material of [86], and [136]), as well as the compiling of the nanoparticle ring formation dynamics into a 3D

or pseudo-3D simulation model (such as that in Chapter 5, see also [86,136]).

Chapter 7

Conclusion

"Physics is really nothing more than a search for ultimate simplicity, but so far all we have is a kind of elegant messiness - or as [the astrophysicist Leon] Lederman put it : 'There is a deep feeling that the picture is not beautiful'."

Bill Bryson.

This chapter recapitulates the objectives of our research on pattern formation, the main orientation of the project, and the experimental approach that was adopted in order to address the subsequent issues. It highlights the progress that was made with regards to understanding and controlling the evaporation / dewetting, self-organisation and pattern formation processes, and puts forward a number of remaining open questions in this domain, in particular concerning the principles of non-equilibrium pattern formation in these systems. Finally, future work and potential implications and applications of our research are outlined.

Reminder of the short and long term objectives

The main long-term objective of the PATTERNS research project, which funded the work described in this thesis, is to establish possible unifying principles in non-equilibrium pattern formation. More specifically, we aim at understanding the mechanisms involved in the occurrence and selection of patterns, in order to gain control over their formation, growth, morphologies and possible characteristic length scales. The system that was chosen for study, i.e. colloidal suspensions of nanoparticles deposited onto a solid substrate, has several advantages : (i) it undergoes spontaneous non-equilibrium pattern formation, (ii) it benefits from a rich literature (e.g. [1–3, 21, 26, 40, 42, 44–46, 48, 49, 69, 73, 74, 76, 80–87, 92–94, 97, 124, 135], etc.), and (iii) it offers a large range of tunable laboratory conditions, providing a wide parameter space to explore.

The main issue to tuning pattern formation is the reproducibility of given experimental conditions, as we were able to appreciate at an early stage of the experimental work discussed in this thesis. Attaining a good degree of reproducibility is an essential requirement for potential applications related to pattern formation, in particular for the bottom-up fabrication of nanoscale devices at the industrial scale. This is why the first short-term objective of this work was to gain a high degree of control over the formation and selection of given types of patterns - which was achieved by developing a novel and well-controlled deposition technique (Chapter 4). Mechanisms of pattern formation are then tentatively deduced from an exhaustive analysis of the experimental conditions required for pattern occurrence, which is how we proceeded in Chapters 4, 5 and 6. These mechanisms must then be validated either by further

experimental developments, or by theoretical models and simulations (e.g. the pseudo-3D model developed in Chapter 5).

Tuning, analysing and controlling pattern formation

In accordance with our primary objectives, the work reported in this thesis initially focused on developing a new deposition technique, designed to provide the highest possible degree of control over dewetting-induced pattern formation (Chapter 4). In terms of *control of the experimental environment*, the conditions of evaporation of nanoparticle solutions on a surface created via our "meniscus deposition technique" are tunable in many aspects, and the process is easily monitored by video camera. In terms of *pattern reproducibility*, it enables the systematic formation of a wide variety of both well-known and less-common nanoparticle arrangements, and it provides a good control of the selected morphologies. In particular, this technique led to the generation of millimeter scale close-packed monolayers of nanoparticles. These arrays of capacitively coupled metallic dots exhibit very specific and interesting conduction properties, and being able to produce them systematically, on scales larger than a few microns, is still challenging nowadays. Our meniscus technique brings a promising solution to these limitations.

The slow evaporation process associated with the meniscus deposition technique is accompanied by instabilities of the liquid front. These were monitored and analysed in order to estimate their impact on pattern formation. In particular, since the meniscus technique involves the formation of certain "unusual" nanoparticle assemblies (well-developed branching structures, Chapter 5), the relationship between macroscopic scale and microscopic scale instabilities was

investigated. The role of free excess thiol molecules in solution (prompted by the work of Lin *et al.* in 2001 [74]) was addressed at several points throughout this thesis. In view of previous hypotheses on this subject [74, 76, 98], we concluded that excess thiol played an important role in the instability of the dewetting front and in particular in the *local wettability* of the substrate by the solvent, but did not have a major effect on the nanoparticle morphologies *at reasonably fast evaporation rates*. Importantly, the presence of excess thiol does not alter the overall evaporation time, confirming that "long" evaporation times (several minutes) alone are not sufficient to create close-packed layers of particles. However, the presence of thiol plays a key role in reducing the void density in nanoparticle assemblies in such conditions.

Broadening the spectrum of observable patterns

The search for the best experimental conditions to form close-packed monolayers of nanoparticles proceeded mostly by trial-and-error, involving the modification and adjustment of (i) the deposition technique, (ii) the solution concentration and quantity, (iii) the choice of substrate and ring size (iv) the evaporation duration and procedure, and (v) the addition of excess thiol in solution. Along with the generation of close-packed monolayers of nanoparticles, these preliminary experiments yielded a number of fascinating - sometimes unexpected - results in terms of the variety of observable patterns. The field of investigated experimental conditions was then extended to modifying the respective wetting properties of nanoparticles, substrate and solvent in order to study the conditions of occurrence of these new patterns.

The manner in which close-packed monolayers formed as a result of

meniscus-driven evaporation highlighted some intriguing aspects of the pattern formation mechanisms. For instance, the solvent "slip-stick" motion, along with the gradients of concentration and evaporation rate across the surface, explain the succession of patterns on the surface, from a fast to a slow evaporation regime. It was also deduced that the presence of excess thiol favoured dense packing, as stated before. In the same way, the generation of unusual patterns had to be associated with specific experimental conditions. Identifying these conditions thus became a mean of formulating hypotheses on the mechanisms of pattern formation, in order to understand the actual *chronology* of this process - from the deposition to the various self-organised arrangements.

Identifying the mechanisms of pattern formation

Two main types of rarely seen patterns were studied in depth : fingering structures (Chapter 5) and rings of nanoparticles (Chapter 6). The former were obtained thanks to the development of the meniscus technique, and were observed as isolated structures, surrounded by nanoparticle networks with a much smaller characteristic length scale.

The fingering patterns result from a nucleation event in a thin dewetting nanoparticle-solvent film, and are surrounded after complete evaporation by smaller length scale networks. The presence of two length scales suggests the coexistence of (at least) two dewetting processes.

The first fundamental question that the formation of fingering patterns raised was that of the interface where the assembly takes place. For fingering structures to indeed result from late-stage nucleation events, we have to prove that the self-organisation takes place in a very thin film of solvent, at the

solvent-substrate interface. This was demonstrated by using a novel contrast-enhanced optical imaging technique, called Sarfus : for the first time, we monitored *in real-time* the deposition and self-organisation of particles in a thin liquid film near the surface, at the base of the meniscus, after the liquid front has retreated. An important consequence of this result is that the system can be faithfully described by Rabani *et al.*'s [1] two-dimensional model.

The second question concerned the coexistence of two types of patterns with different morphologies and characteristic length scales. We postulated that the smaller networks must originate from a second dewetting event, taking place at later times than that which created the large "slowly" growing fingering structures. A liquid coverage dependance of the evaporation regime (represented by the chemical potential of the solvent) was added to a simulated 2D description of our thin dewetting liquid layer. A step-function variation of the chemical potential, corresponding to different evaporation regimes as the solvent coverage evolves (slow for a high coverage, much faster for a low coverage), is consistent with the direct observation made of the evaporation process and yielded results that both qualitatively and quantitatively reproduced the experimental images, thus confirming the initial hypothesis.

The last issue aimed at relating the occurrence of these patterns with the very similar looking and widely studied "viscous fingering" phenomenon. The latter is described in terms of viscosity and surface tension, which, for our system, are intrinsically related to the diffusion of nanoparticles. Experimentally, this translated into the modification of the interparticle and the solvent-particle interactions. However, it is still difficult to establish the real dependency that exists between the experimental conditions and the variations of viscosity and

surface tension, since the effects of the parameters are often correlated. Although we were able to identify a clear tendency and attain a very good experimental reproducibility, estimating the correlation between pattern formation, viscosity, and surface tension is still an issue to be addressed (preliminary measurements of the viscosities and surface tensions of our solutions have not yield exploitable results and conclusions so far).

We now have a good understanding of the mechanisms that lead to the formation of fingering structures in nanoparticle assemblies, and we can accurately identify the effects of given experimental parameters on the nature, size and shape of the patterns obtained. An advanced 2D simulation model ("pseudo-3D" model), that relies on hypotheses consistent with experiments, was used to validate these mechanisms [106].

Following the same type of approach, we then studied the formation of nanoparticle rings. Our preliminary investigation of the experimental parameter space led to important conclusions concerning the necessary conditions to nanoparticle ring formation. In given experimental conditions, nanoparticle solutions with different wetting properties will form specific types of patterns. To a certain extent, a correlation can be established between the pattern formed and the wetting properties of the solvent. This observation allowed us to create nanoparticle rings with a very high degree of reproducibility. The corresponding experimental conditions are a high enough mobility of the nanoparticles in solution and a fast evaporation provided both by a high volatility (i.e. vapor pressure) of the solvent and an adapted deposition technique (spin-coating).

Concerning the mechanism of ring formation, the presence of interconnecting sub-monolayer networks between adjacent rings, whose height is generally

larger than one nanoparticle diameter, suggests that two dewetting processes coexist, as in the case of fingering patterns. Our assumption is that rings form in a thick enough solvent film, where the mobility of the particles is high. Then the reduction of the nanoparticle mobility and the increase of nanoparticle concentration as the film thins down lead to the formation of the smaller network, which sometimes exhibits a fingering structure. In order to have a direct observation of this mechanism, it would be very useful to monitor dewetting of such a system in real-time. The rapidity of the evaporation makes such an observation difficult. One of the future developments of this study will be to pursue experiments using the contrast-enhanced Sarfus optical microscope (Chapter 5) in order to solve this issue.

Further investigation will also involve the development of a computational model that reproduces the dewetting process suggested above, probably by using a fully-3D description similar to that made by Yosef and Rabani's [82] (the pseudo-3D model of Chapter 5 cannot produce 3D nanoparticle arrangements). From the experimental point of view, the conditions that lead to ring formation are easy to implement and offer a high degree of reproducibility, which encourages us to move towards an even higher degree of experimental control, by influencing the formation of nanoparticle rings via an external contribution, such as the local alteration of the substrate's wettability or the introduction of defects on the surface.

A preliminary result of such an experiment is illustrated in Fig. 7.1 : silicon oxide patterns, a few nanometers high, are "drawn" onto an hydrogen-terminated silicon substrate (SiH) [86]: a full 4μm$\times 4\mu$m square in Fig. 7.1(a), an empty 4μm$\times 4\mu$m square in Fig. 7.1(b) and dots separated by 2μm and

disposed as a 3×3 square in Fig. 7.1(c). The presence of an hydrophilic square of oxide on an hydrophobic surface seems to favour the formation of rings when a dichloromethane-based solution is spin-coated on the substrate, whereas spinodal-like patterns form on defect free SiH (Fig. 7.1(a)). In Fig. 7.1(b), the rings only nucleate on the thin oxide lines that delimitate the square perimeter, and grow on either side of the lines. The rings of Fig. 7.1(c) form almost exclusively in the vicinity of the nanometer size spots, which seem to constitute preferred dewetting sites.

Many questions remain to be addressed in view of Fig. 7.1 [136]. The mechanism of formation of nanoparticle rings is a very complex one and despite the experimental control and reproducibility that we can now achieve, we have only just started to understand the principles that govern such pattern formation.

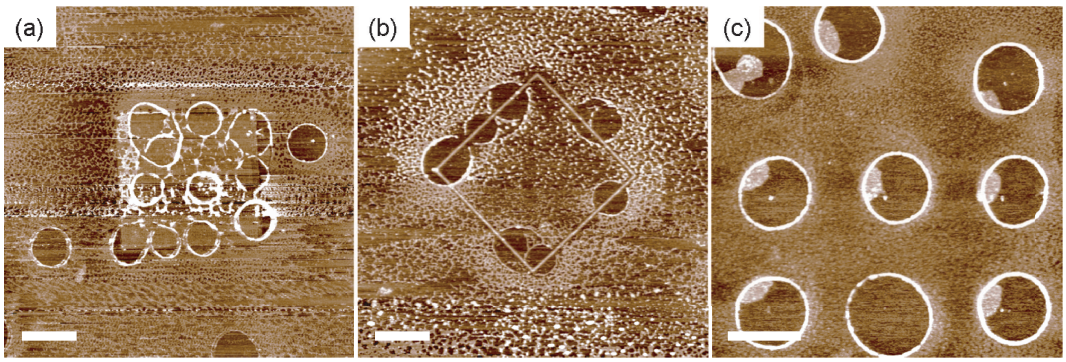

Figure 7.1: *Guided formation of nanoparticle rings from a dichloromethane-based solution onto an H-terminated silicon substrate onto which (a) a full 4μm×4μm square, (b) an empty 4μm×4μm square and (c) regularly spaced (separated by 2μm and disposed as a 3×3 square) nanometer size dots of silicon oxide have been regrown, using AFM nanolithography [86]. The scale bar represents 1μm. Courtesy of A. Stannard [136].*

Further work and applications

We have suggested a number of short term routes to explore in terms of experimental investigation for studying in depth the mechanisms of dewetting-induced pattern formation. In the longer term, it would be interesting to follow a protocol such as that used in this thesis in order to study different types of patterns. Novel techniques such as the contrast-enhanced Sarfus optical microscopy presented here should broadly contribute to facilitating such investigations. Ultimately, we aim at connecting all the observable patterns and the processes that generate them, and obtain a unifying picture of the principles that guide pattern formation in such systems (colloidal self-organised nanoparticles). We have already observed similarities between the formation of fingering structures and of nanoparticle rings. Do the conditions that lead to various patterns evolve as a continuum or do these conditions encounter *critical points* ? Is there a "hierarchy" of pattern formation principles, as there seems to be "hierarchy" amongst the types of patterns formed ? Do similarities exist between these principles and those that create patterns in totally different systems on all scales ? Can we legitimately draw a parallel between these phenomena ? These are the key questions that remain to be addressed.

In addition to exploring the experimental aspects, models will need to be developed in order to support experimentally-deduced principles. Simulations are a necessary tool, as was demonstrated in Chapter 5, in order to draw an exhaustive description of evaporation processes. Ultimately, we aim at developing a model that would include all experimental results. For this purpose, we already extended the existing 2D model [1] to a pseudo-3D description [86] so that the results obtained via our meniscus technique could be taken into

account [106], in addition to the results of past experiments [47,50,81]. Eventually, such a model could be used as a predictive tool for foreseing the formation of patterns in unexplored regions of the parameter space, for instance.

Finally, one should not overlook the potential for direct applications of self-organised nanoparticles. We have highlighted in Chapter 2 the unusual electronic properties of nanoparticle arrays, but interesting optical properties can also be foreseen and, depending on the type of particles used, electro-magnetic properties too. It is thus essential to achieve a sufficient degree of control over the organisation of such nanoparticles to systematically produce samples for the study of their properties and, ultimately, for the mass production required by industrial applications. Only a thorough experimental investigation of pattern formation, growth and, even more importantly, stability will allow us to eventually meet these requirements.

Bibliography

[1] E. Rabani, D. R. Reichman, P. L. Geissler, and L. E. Brus. Drying-mediated self-assembly of nanoparticles. *Nature*, 426:pp271–274, 2003.

[2] P. C. Ohara and W. M. Gelbart. Interplay between hole instability and nanoparticle array formation in ultrathin liquid films. *Langmuir*, 14:pp3418–3424, 1998.

[3] M. Maillard, L. Motte, A. T. Ngo, and M. P. Pileni. Rings and hexagons made of nanocrystals: A marangoni effect. *J. Phys. Chem. B*, 104:pp11871–11877, 2000.

[4] *Wikipedia, The Free Encyclopedia*. http://www.wikipedia.org.

[5] A. M. Lancasta, I. R. Cantalapiedra, C. E. Auguet, A. Penaranda, and L. Ramirez-Piscina. Modeling of spatio-temporal patterns in bacterial colonies. *Phys. Rev. E*, 59:pp7036–7041, 1999.

[6] P. Ball. *The Self-Made Tapestry: Pattern Formation in Nature*. Oxford University Press, New York, 1999.

[7] L. Da Vinci. *The Notebooks of Leonardo Da Vinci.* Translation by Jean-Paul Richter available on line at http://www.sacred-texts.com/aor/dv/index.htm.

[8] H. Bénard. Les tourbillons cellulaires dans une nappe liquide. *Rev. Gen. Sci. Pures Appl.*, 11:pp1261, 1900.

[9] A. M. Turing. The chemical basis of morphogenesis. *Phil. Trans. Royal Soc. London*, B327:pp37–72, 1952.

[10] B. P. Belousov. *in Sbornik Referatov po Radiatsinnoi Meditsine (Trans. Collections of Abstracts on Radiation Medicine, Medgiz, Moscow)*, pages pp145–147, 1958.

[11] A. M. Zhabotinsky. Periodic liquid phase reactions. *Proc. Ac. Sci. USSR*, 157:pp392, 1964.

[12] A. N. Zaikin and A. M. Zhabotinsky. Concentration wave propagation on two-dimensional liquid-phqse self-oscillating system. *Nature*, 225:pp535–537, 1970.

[13] R. J. Field and M. Burger. *Oscillations and Travelling Waves in Chemical Systems.* Wiley, New York, 1985.

[14] H. J. S. Hele Shaw. The flow of water. *Nature*, 58:pp34–36, 1898.

[15] P. G. Saffman and G. I. Taylor. The penetration of a fluid into a porous medium or hele-shaw cell containing a more viscous liquid. *Proc. Royal Society*, 245:pp312–329, 1958.

[16] B. Bryson. *A Short Story of Nearly Everything.* Black Swan, 2004. I particularly recommend chapter 2 of this well-documented book, that recounts with great accuracy (while appealing to non-specialists) the birth of geology as a scientific field of investigation, and very clearly points out how the mere observation of nature has brought very many answers about the age of the planet, the formation of mountains or other large scale phenomena that seem very obvious to us nowadays but were totally unknown only a few centuries ago.

[17] M. Matsushita and H. Fukiwara. Fractal growth and morphological change in bacteria colony formation. *In 'Growth Patterns in Physical Sciences and Biology'.* Editors: J. M. Garci-Ruiz, E. Louis, P. Meakin and L. M. Sander (Plenum Press, New York, 1993).

[18] B. B. Mandelbrot. *The Fractal Geometry of Nature.* W. H. Freeman, New York, 1983.

[19] D. Weaire and N. Rivier. *Contemp. Phys.*, 25:pp59, 1984.

[20] N. Rivier. *Philos. Mag. B*, 52:pp795, 1985.

[21] P. Moriarty, M. D. R. Taylor, and M. Brust. Nanostructured cellular networks. *Phys. Rev. Lett.*, 89:pp248303(1–4), 2002.

[22] G. Binnig and H. Rohrer. Scanning tunneling microscopy. *Helve. Physica Acta*, 55:pp726–735, 1982.

[23] G. Binnig, H. Rohrer, C. Gerber, and E. Weibel. Surface studies by scanning tunnelling microscope. *Phys. Rev. Lett.*, 49:pp57–61, 1982.

[24] D. M. Eigler and E. K. Schweizer. Positioning single atoms with a scanning tunelling microscope. *Nature*, 344:pp524–526, 1990.

[25] V. Derycke, R. Martel, J. Appenzeller, and P. Avouris. Carbon nanotube inter- and intramolecular logic gates. *Nano Letters*, 1:pp453–456, 2001.

[26] C. J. Kiely, J. Fink, M. Brust, D. Bethell, and D. J. Schiffrin. Spontaneous ordering of bimodal ensembles of nanoscopic gold clusters. *Nature*, 396:pp444–446, 1998.

[27] Science magazine breakthrough of the year: Molecules get wired. *Science*, 294:pp2442–2443, 2001.

[28] C. Dekker. *Phys. Today*, 52:pp22, 1999.

[29] M. Ouyang, J. L. Huang, C. L. Cheung, and C. M. Lieber. Atomically resolved single-walled carbon nanotube intramolecular junctions. *Science*, 291:pp97–100, 2001.

[30] Y. Huang, X. Duan, Q. Wei, and C. M. Lieber. Directed assembly of one-dimensional nanostructures in functional networks. *Science*, 291:pp630–633, 2001.

[31] J. H. Schon, C. Kloc, H. Y. Hwang, and B. Batlogg. Josephson junctions with tuneable weak links. *Science*, 292:pp252–254, 2001.

[32] H. W. C. Postma, T. Teepen, Z. Yao, M. Grifoni, and C. Dekker. Carbon nanotube single-electron transistors at room temperature. *Science*, 293:pp76–79, 2001.

[33] Y. Huang, X. Duan, Y. Cui, L. J. Lauhon, K. H. Kim, and C. M. Lieber. Logic gates and computation from assembles nanowire building blocks. *Science*, 294:pp1313–1317, 2001.

[34] A. Bachtold, P. Hadley, T. Nakanishi, and C. Dekker. Logic circuits with carbon nanotube transistors. *Science*, 294:pp1317–1320, 2001.

[35] C. P. Collier, J. O. Jeppesen, Y. Luo, J. Perkins, E. W. Wong, J. R. Heath, and J. F. Stoddart. Molecular-based electronically switchable tunnel junction devices. *J. Am. Chem. Soc.*, 123:pp12632–12641, 2001.

[36] J. H. Schon, H. Meng, and Z. Bao. Field-effect modulation of the conductance of single molecules. *Science*, 294:pp2138–2140, 2001.

[37] J. Park, A. N. Pasupathy, J. I. Goldsmith, A. V. Soldatov, C. Chang, Y. Yaish, J. P. Sethna, H. D. Abruna, D. C. Ralph, and P. L. McEuen. Wiring up single molecules. *Thin Solid Films*, 438–439:pp457–461, 2003.

[38] N. Tessler, V. Medvedev, M. Kazes, S. Kan, and U. Banin. Efficient near-infrared polymer nanocrystal light-emitting diodes. *Science*, 295:pp1506–1508, 2002.

[39] K. Keren, R. S. Berman, E. Buchstab, U. Sivan, and E. Braun. Dna-templated carbon nanotube field-effect transistor. *Science*, 302:pp1380–1382, 2003.

[40] P. Moriarty. Nanostructured materials. *Rep. Prog. Phys.*, 64:pp297–381, 2001.

[41] R. K. Smith, P. A. Lewis, and P. S. Weiss. Patterning self-assembled monolayers. *Prog. Surf. Sc.*, 75:pp1–68, 2004.

[42] R. P. Andres, J. D. Bielefeld, J. I. Henderson, D. B. Janes, V. R. Kolagunta, C. P. Kubiak, W. J. Mahoney, and R. G. Osifchin. Self-assembly of a two-dimensional superlattice of molecularly linked metal clusters. *Science*, 273:pp1690–1693, 1996.

[43] A. A. Middleton and N. S. Wingreen. Collective transport in arrays of small metallic dots. *Phys. Rev. Lett.*, 71:pp3198–3201, 1993.

[44] R. Parthasarathy and X. M. Linnd H. M. Jaeger. Electronic transport in metal nanocrystal arrays: The effect of structural disorder on scaling behavior. *Phys. Rev. Lett*, 87:pp186807(1–4), 2001.

[45] R. Parthasarathy, X. M. Lin, K. Elteto, T. F Rosenbaum, and H. M. Jaeger. Percolating through networks of random thresholds: Finite temperature electron tunnelling in metal nanocrystal arrays. *Phys. Rev. Lett.*, 92:pp076801(1–4), 2004.

[46] K. Elteto, X. M. Lin, and H. M. Jaeger. Electronic transport in quasi-one-dimensional arrays of gold nanocrystals. *Phys. Rev. B*, 71:pp205412(1–5), 2005.

[47] M. O. Blunt. Far from equilibrium nanoparticle assemblies: Patterns, transport and dynamics. *Thesis*, 2006.

[48] M. O. Blunt, M. Suvakov, F. Pulizzi, C. P. Martin, E. Pauliac-Vaujour, A. Stannard, A. Rushforth, B. Tadic, and P. Moriarty. Charge transport

in cellular nanoparticle networks: Meandering through nanoscale mazes. *Nano Letters*, 7:pp855–860, 2007.

[49] M-C. Daniel and D. Astruc. Gold nanoparticles: Assembly, supramolecular chemistry, quantum-size-related properties, and applications toward biology, catalysis, and nanotechnology. *Chem. Rev.*, 104:pp293–346, 2004.

[50] C. P. Martin. Pattern formation in self-organised nanoparticle assemblies. *Thesis*, 2007.

[51] N. D. Denkov, O. D. Velev, P. A. Kralchevsky, I. B. Ivanov, H. Yoshimura, and K. Nagayama. Mechanism of formation of two-dimensional crystals from latex particles on substrates. *Langmuir*, 8:pp3183–3190, 1992.

[52] A. Yochelis, A. Hagberg, E. Meron, A. L. Lin, and H. L. Swinney. Development of standing-wave labyrinthine patterns. *SIAM J. Applied Dynamical Systems*, 1:pp236–247, 2002.

[53] L. Rishtroph, M. Thrasher, M. B. Mineev-Weinstein, and H. L. Swinney. Fjords in viscous fingering: Selection of width and opening angle. *Phys. Rev. E*, 74:pp015201(1–4), 2006.

[54] K. G. Libbrecht. The physics of snow crystals. *Rep. Prog. Phys.*, 68:pp855–895, 2005.

[55] *The University Corporation for Atmospheric Research.* http://www.ucar.edu/news/releases/2006/hurricanes.shtml.

[56] T. A. Witten and L. M. Sander. Diffusion-limited aggregation. *Phys. Rev. B*, 27:pp5686–5697, 1983.

[57] T. A. Witten and L. M. Sander. Diffusion-limited aggregation, a kinetic critical phenomenon. *Phys. Rev. Lett.*, 47:pp1400–1403, 1981.

[58] F. London. *Zeitschrift fur Physik*, 60:pp245, 1930.

[59] F. London. *Z. Physik. Chemie*, B11:pp222, 1930.

[60] H. C. Hamaker. The london-van der waals attraction between spherical particles. *Physica*, 4:pp1058, 1937.

[61] J. Israelachvili. *Intermolecular and Surface Forces*. Academic Press (2nd Edition), 1992.

[62] E. M. Lifshitz. The theory of molecular attraction forces between solid bodies. *Soviet. Phys. JETP (English Translation)*, 2:pp73, 1956.

[63] P-G. De Gennes, F. Brochard-Wyart, and D. Quéré. *Gouttes, Bulles, Perles et Ondes*. Belin Collection Echelles, Paris, 2002.

[64] R. Seemann, S. Herminghaus, and K. Jacobs. Dewetting patterns and molecular forces: A reconciliation. *Phys. Rev. Lett.*, 86:pp5534–5537, 2001.

[65] K. Jacobs, S. Herminghaus, and K. R. Mecke. Thin liquid polymer films rupture via defects. *Langmuir*, 14:pp965–969, 1998.

[66] S. Herminghaus, K. Jacobs, K. Mecke, J. Bischof, A. Ferry, M. Ibn-Elhaj, and S. Schlagowski. Spinodal dewetting in liquid crystal and liquid metal films. *Science*, 282:pp916–919, 1998.

[67] R. Xie, A. Karim, J. F. Douglas, C. C. Han, and R. A. Weiss. Spinodal dewetting of thin polymer films. *Phys. Rev. Lett.*, 81:pp1251–1254, 1998.

[68] E. Ruckenstein and R. K. Jain. Spontaneous rupture of thin liquid films. *J. Chem. Soc. Faraday Trans. II*, 70:pp132–147, 1974.

[69] M. Maillard ans L. Motte and M. P. Pileni. Rings and hexagons made of nanocrystals. *Adv. Mater.*, 13:pp200–204, 2001.

[70] M. J. Block. Surface tension as the cause of bénard cells and surface deformation in a liquid film. *Nature*, 178:pp650–651, 1956.

[71] J. R. A. Pearson. On convection cells induced by surface tension. *J. Fluid Mech.*, 4:pp489, 1958.

[72] C. Stowell and B. A. Korgel. Self-assembled honeycomb networks of gold nanocrystals. *Nano Letters*, 1:pp595–600, 2001.

[73] C. J. Kiely, J. Fink, J. G. Zheng, M. Brust, D. Bethell, and D. J. Schiffrin. Ordered colloidal nanoalloys. *Adv. Mater.*, 12:pp640–643, 2000.

[74] X. M. Lin, H. M. Jaeger, C. M. Sorensen, and K. J. Kablunde. Formation of long-range-ordered nanocrystal superlattices on silicon nitride substrates. *J. Phys. Chem. B*, 105:pp3353–3357, 2001.

[75] S. Narayanan, J. Wang, and X. M. Lin. Dynamical self-assembly of nanocrystal superlattices during colloidal droplet evaporation by in-situ small angle x-ray scattering. *Phys. Rev. Lett.*, 93:135503–1–4, 2004.

[76] T. P. Bigioni, X. M. Lin, T. T. Nguyen, E. I. Corwin, T. A. Witten, and H. M Jaeger. Kinetically driven self assembly of highly ordered nanoparticle monolayers. *Nature Materials*, 5:pp265–270, 2006.

[77] A. J. Rimberg, T. R. Ho, and J. Clarke. Scaling behavior in the current-voltage characteristic of one- and two-dimensional arrays of small metallic islands. *Phys. Rev. Lett.*, 74:pp4714–4717, 1995.

[78] M. N. Wybourne, L. Clarke, M. Yan, S. X. Cai, L. O. Brown, J. Hutchinson, and J. F. W. Keana. Coulomb-blockade dominated transport in patterned gold-cluster structures. *Jpn. J. Appl. Phys.*, 36:pp7796–7800, 1997.

[79] C. Reichhardt and C. J. Olson Reichhardt. Charge transport transitions and scaling in disordered arrays of metallic dots. *Phys. Rev. Lett.*, 90:pp046802(1–4), 2003.

[80] G. Ge and L. Brus. Evidence for spinodal phase separation in two-dimensional nanocrystal self-assembly. *J. Phys. Chem. B*, 104:pp9573–9575, 2000.

[81] C. P. Martin, M. O. Blunt, and P. Moriarty. Nanoparticle networks on silicon: Self-organized or disorganized? *Nano Letters*, 4:pp2389–2392, 2004.

[82] G. Yosef and E. Rabani. Self-assembly of nanoparticles into rings: A lattice-gas model. *J. Phys. Chem. B*, 110:pp20965–20972, 2006.

[83] J. Huang, A. R. Tao, S. Connor, R. He, and P. Yang. A general method for assembling single colloidal particle lines. *Nano Letters*, 6:pp524–529, 2006.

[84] J. Xu, J. Xia, S. W. Hong, Z. Q. Lin, F. Qiu, and Y. L. Yang. Self-assembly of gradient concentric rings via solvent evaporation from a capillary bridge. *Phys. Rev. Lett.*, 96:pp066104(1–4), 2006.

[85] J. Xu, J. Xia, and Z. Lin. Evaporation-induced self-assembly of nanoparticles from a sphere-on-flat geometry. *Angew. Chem. Int. Ed.*, 46:pp1860–1863, 2007.

[86] C. P. Martin, M. O. Blunt, E. Pauliac-Vaujour, I. Vancea, U. Thiele, and P. Moriarty. Organising nanoparticles via directed solvent dewetting. *Phys. Rev. Lett.*, 99:pp116103(1–4), 2007.

[87] M. Brust, M. Walker, D. Bethell, D. J. Schiffrin, and R. Whyman. Synthesis of thiol-derivatised gold nanoparticles in a two-phase liquid-liquid system. *J. Chem. Soc., Chem. Commun.*, page 426, 1994.

[88] J. Turkevich, P. C. Stevenson, and J. Hillier. A study of the nucleation and growth processes in the synthesis of colloidal gold. *J. Discuss. Faraday Soc.*, 11:pp55–75, 1951.

[89] C. Pale-Grosdemange, E. S. Simon, K. L. Prime, and G. M. Whitesides. Formation of self-assembled monolayers by chemisorption of derivatives of oligo(ethylene glycol) of structure hs(ch2)11(och2ch2)moh on gold. *J. Am. Chem. Soc.*, 113:pp12–20, 1991.

[90] A. G. Kanaras, F. S. Kamounah, K. Schaumburg, C. J. Kiely, and M. Brust. Thioalkylated tetraethylene glycol: A new ligand for water soluble monlayer protected gold clusters. *J. Chem. Soc., Chem. Commun.*, pages pp2294–2295, 2002.

[91] M. Brust, J. Fink, D. Bethell, D. J. Schiffrin, and C. J. Kiely. Synthesis and reactions of functionalised gold nanoparticles. *J. Chem. Soc., Chem. Commun.*, pages pp1655–1656, 1995.

[92] E. Pauliac-Vaujour and P. Moriarty. Meniscus-mediated organization of colloidal nanoparticles. *J. Phys. Chem C*, 111:pp16255–16260, 2007.

[93] R. D. Deegan, O. Bakajin, T. F. Dupont, G. Huber, S. R. Nagel, and T. A. Witten. Capillary flow as the cause of ring stains from dried liquid drops. *Nature*, 389:pp827–829, 1997.

[94] R. D. Deegan. Pattern formation in drying drops. *Phys. Rev. E*, 61:pp475–485, 2000.

[95] C. Gigault, K. Dalnoki-Veress, and J. R. Dutcher. Changes in the morphology of self-assembles polystyrene microsphere monolayers produced by annealing. *J. Colloid and Interface Science*, 243:pp143–155, 2001.

[96] http://www.nano-lane.com.

[97] C. P. Martin, M. O. Blunt, E. Vaujour, A. Fahmi, A. D'Aleo, L. De Cola, F. Vogtle, and P. Moriarty. Self-organised nanoparticle assemblies; a panoply of patterns. *In 'Systems Self-Assembly: Multidisciplinary Snapshots'.* (Studies in Multidisciplinarity, Volume 5). Editors: N. Krasnogor, S. Gustafson, D. Pelta and J. L. Verdegay (Elsevier, 2007).

[98] D. Qu, R. Suter, and S. Garoff. Surfactant self-assemblies controlling spontaneous dewetting. *Langmuir*, 18:pp1649–1654, 2002.

[99] V. N. Truskett and K. J. Stebe. Influence of surfactants on an evaporating drop: Fluorescence images and particle deposition patterns. *Langmuir*, 19:pp8271–8279, 2003.

[100] K. S. Varanasi and S. Garoff. Unsteady motion of receding contact lines of surfactant solutions: The role of surfactant re-self-assembly. *Langmuir*, 21:pp9932–9937, 2005.

[101] R. V. Craster and O. K. Matar. On autophobing in surfactant-driven thin films. *Langmuir*, 23:pp2588–2601, 2007.

[102] S. J. Gokhale, J. L. Plawsky, and P. C. Wayner. Spreading, evaporation, and contact line dynamics of surfactant-laden microdrops. *Langmuir*, 21:pp8188–8197, 2005.

[103] K. Y. Chan and A. J. Borhan. Surfactant-assisted spreading of a liquid drop on a smooth solid surface. *J. Colloid and Interface Science*, 287:pp233–248, 2005.

[104] O. E. Jensen and S. J. Naire. The spreading and stability of a surfactant-laden drop on a prewetted substrate. *Fluid Mech.*, 554:pp5–24, 2006.

[105] A. B. Afsar-Siddiqui, P. F. Luckham, and O. K. Matar. Dewetting behaviour of aqueous cationic surfactant solutions on liquid films. *Langmuir*, 20:pp7575–7582, 2004.

[106] E. Pauliac-Vaujour, A. Stannard, C. P. Martin, and P. Moriarty. Fingering instabilities in dewetting nanofluids. *Submitted to Phys. Rev. Lett.*, 2008.

[107] M. Elbaum and S. G. Lipson. How does a thin wetted film dry up ? *Phys. Rev. Lett.*, 71:pp3562–3565, 1994.

[108] N. Samid-Mrzel, S. G. Lipson, and D. S. Tannhauser. Pattern formation in drying water films. *Phys. Rev. E*, 57:pp2906–2913, 1998.

[109] A. V. Lyushnin, A. A. Golovin, and L. M. Pismen. Fingering instability of thin evaporating liquid films. *Phys. Rev. E*, 65:pp021602(1–7), 2002.

[110] J. Feder. *Fractals*. Plenum Press, New York, 1988.

[111] S. S. Manna and B. Subramanian. Quasirandom spanning tree model for the early river network. *Phys. Rev. Lett.*, 76:pp3460–3463, 1996.

[112] J. R. Castrejon Pita, A. Sarmiento Galan, and A. Castrejon Garcia. Fractal dimension and self-similarity in asparagus plumosus. *Fractals*, 10:pp429, 2002.

[113] H. M. Singer. Measurements of the three-dimensional shape of ice crystals in supercooled water. *Phys. Rev. E*, 73:pp051606(1–4), 2006. And references therin [1-6],[10],[11],[15],[16].

[114] W. Kurz and D. J. Fisher. *Fundamentals of Solidification*. Trans. Tech. Publ. Ltd, Switzerland (4th edition), 1998.

[115] S. Hill. *Chem. Eng. Sci.*, 1:pp247–253, 1952.

[116] R. L. Chouke, P. Van Meurs, and C. Van der Poel. *Trans. AIME*, 216:pp188–194, 1959.

[117] D. Bensimon, L. P. Kadanoff, S. Liang, B. I. Shraiman, and C. Tang. Viscous flows in two dimensions. *Rev. Mod. Phys.*, 58:pp977–999, 1986.

[118] D. C. Hong and J. S. Langer. Analytic theory of the selection mechanism in the saffman-taylor problem. *Phys. Rev. Lett.*, 56:pp2032–2035, 1986.

[119] M. G. Moore, A. Juel, J. M. Burgess, W. D. McCormick, and H. L. Swinney. Fluctuations in viscous fingering. *Phys. Rev. E*, 65:pp030601(1–4), 2002.

[120] G. M. Homsy. Viscous fingering in porous media. *Annual Rev. Fluid Mech.*, 19:pp271–314, 1987.

[121] J. Nittmann and H. E. Stanley. Tip splitting without interfacial tension and dendritic growth patterns arising from molecular anisotropy. *Nature*, 321:pp663–668, 1986.

[122] Centre for Polymer Studies (CPS) http://polymer.bu.edu/ trunfio/images.html.

[123] H. Bhadeshia, University of Cambridge, http://www.msm.cam.ac.uk/phase-trans/dendrites.html.

[124] L. Motte and M. P. Pileni. Self-assemblies of silver sulfide nanocrystals : Influence of length of thiol-alkyl chains used as a coating agent. *App. Surf. Sci.*, 164:pp60–67, 2000.

[125] http://www.ees.nmt.edu/ davew/P362/boxcnt.htm.

[126] P. Grassberger and I. Procaccia. Characterization of strange attractors. *Phys. Rev. Lett.*, 50:pp346–349, 1983.

[127] O. Praud and H. L. Swinney. Fractal dimension and unscreened angles measured for radial viscous fingering. *Phys. Rev. E*, 72:pp011406(1–10), 2005.

[128] A. Stannard, C. P. Martin, E. Pauliac-Vaujour, and P. Moriarty. In Preparation.

[129] F. Brochard-Wyart and J. Daillant. Drying of solids wetted by thin liquid films. *Can. J. Phys.*, 68:pp1084–1088, 1990.

[130] U. Thiele. Open questions and promising new fields in dewetting. *Eur. Phys. J. E*, 12:pp409–416, 2003.

[131] L. Bergstrom. Hamaker constants of inorganic materials. *Adv. Colloid and Interface Science*, 70:pp125–169, 1997.

[132] *CRC Handbook of Chemistry and Physics (Online).* http://www.hbcpnetbase.com, 88th Ed.

[133] W. P. Wuelfing, A. C. Templeton, J. F. Hicks, and R. W. Murray. Taylor dispersion measurements of monolayer protected clusters: A physicochemical determination of nanoparticle size. *Anal. Chem.*, 71:pp4069–4074, 1999.

[134] R. Seemann, S. Herminghaus, and K. Jacobs. Gaining control of pattern formation of dewetting liquid films. *J. Phys. Condens. Matter*, 13:pp4925–4938, 2001.

[135] M. O. Blunt, C. P. Martin, M. Ahola-Tuomi, E. Pauliac-Vaujour, P. Sharp, P. Nativo, M. Brust, and P. Moriarty. Coarced coarsening of nanoparticle assemblies. *Nature Nanotech.*, 2:pp167–170, 2007.

[136] A. Stannard. unpublished.

List of Figures